

**PROBING INTO THE EVOLUTION OF A
POLYMORPHIC SEMICONDUCTOR AT NANOSCALE**

ALIREZA YAGHOUBI TAEMEH

**DISSERTATION SUBMITTED IN FULFILMENT OF
THE REQUIREMENTS FOR THE DEGREE OF MASTER
OF ENGINEERING SCIENCE**

**FACULTY OF ENGINEERING
UNIVERSITY OF MALAYA
KUALA LUMPUR**

2018

UNIVERSITY OF MALAYA
ORIGINAL LITERARY WORK DECLARATION

Name of Candidate: Alireza Yaghoubi Taemeh

Matric No: KGA160040

Name of Degree: Master of Engineering Science (Materials Engineering)

Title of Dissertation (“this Work”):

Probing into the Evolution of a Polymorphic Semiconductor at Nanoscale

Field of Study: Advanced Materials / Nanomaterials

I do solemnly and sincerely declare that:

- (1) I am the sole author/writer of this Work;
- (2) This Work is original;
- (3) Any use of any work in which copyright exists was done by way of fair dealing and for permitted purposes and any excerpt or extract from, or reference to or reproduction of any copyright work has been disclosed expressly and sufficiently and the title of the Work and its authorship have been acknowledged in this Work;
- (4) I do not have any actual knowledge nor do I ought reasonably to know that the making of this work constitutes an infringement of any copyright work;
- (5) I hereby assign all and every rights in the copyright to this Work to the University of Malaya (“UM”), who henceforth shall be owner of the copyright in this Work and that any reproduction or use in any form or by any means whatsoever is prohibited without the written consent of UM having been first had and obtained;
- (6) I am fully aware that if in the course of making this Work I have infringed any copyright whether intentionally or otherwise, I may be subject to legal action or any other action as may be determined by UM.

Candidate’s Signature

Date:

Subscribed and solemnly declared before,

Witness’s Signature Date:

Name:

Designation:

PROBING INTO THE EVOLUTION OF A POLYMORPHIC SEMICONDUCTOR AT NANOSCALE

ABSTRACT

Graphene is considered to be the most likely candidate for the post-silicon era however the problem with its zero band gap is challenging to overcome. A close relative of silicon, silicon carbide is expected to have a stable 2D polymorph which happens to be a wide-gap semiconductor. Unfortunately, the so-called silagraphene has proven to be elusive. To date, neither theoretical, nor experimental studies have been conclusive. In this thesis, computational methods have been employed to determine the stable arrangements of silagraphene, and establish their accurate band structure. Models were experimentally validated by preparing and characterizing a number of graphitic features. Silagraphene exhibits a wide spectrum of optoelectronic properties (360-690 nm) as well as an unusual band structure with highly anisotropic transport properties, which originates from its non-dispersive band near its K-point. This feature makes direct-indirect gap crossover extremely sensitive to ambient conditions, making silagraphene suitable for a range of sensors. We also demonstrate that a particular arrangement of atoms that represent 9R-SiC occurs when the metastable AA' silagraphene is relaxed. This structure has a very similar microscopic and crystallographic signature to that of 3C-SiC and 15R-SiC, respectively, which might explain why it has evaded detection until now. Its vibrational footprint on the other hand is quite distinct thanks to its fewer active phonon modes. Surprisingly, the indirect band gap of this polytype is slightly wider than that of 2H-SiC, despite its lower hexagonality, and is equivalent to that of GaN. Due to its unique conduction band structure, 9R-SiC may also exhibit improved

electron transport properties as compared to other SiC polytypes; and therefore could be suitable for high-frequency and high-voltage applications.

Keywords: Two-Dimensional Materials, Silagraphene, Electronic Band Structure, Density Functional Theory, Raman Scattering

University of Malaya

PENYELIDIKAN EVOLUSI SEMIKONDUKTOR POLIMORFIK DI NANOSCALE

ABSTRAK

Graphene dianggap sebagai calon yang baik untuk era pasca silikon namun masalah jurang band sifarnya amat mencabar untuk diatasi. Sekumpulan serupa silikon seperti karbida silikon dijangka mempunyai polimorf 2D yang stabil menyerupai semikonduktor jurang luas. Akan tetapi, bahan yang dikenali sebagai silagraphene telah terbukti sukar difahami. Setakat ini, kajian teoretikal atau eksperimen tidak dapat dipastikan. Dalam tesis ini, kami menggunakan kaedah pengiraan untuk menentukan kestabilan susunan silagraphene dan menetapkan struktur band-nya yang tepat. Kami juga membuktikan melalui eksperimen model kami dengan menyediakan dan mencirikan beberapa ciri-ciri grafit. Silagraphene mempamerkan spektrum sifat optoelektronik yang luas (360-690 nm) serta struktur jalur yang luar biasa dengan sifat pengangkutan anisotropik yang berasal dari jalur bukan penyebarannya dekat titik K-nya. Ciri ini menghasilkan penyeberangan antara jurang langsung dan tidak langsung menjadi amat sensitif terhadap keadaan ambien maka menjadikan silagraphene amat sesuai untuk pelbagai sensor. Kami juga memperlihatkan susunan atom-atom yang mewakili 9R-SiC berlaku apabila silagraphene AA' metastable dalam keadaan tenang. Struktur ini mempunyai tanda mikroskopik dan kristallografik yang amat mirip dengan 3C-SiC dan 15R-SiC. Oleh itu, ia telah mengelakkan pengesanan sehingga kini. Selain itu, jejak getarannya adalah amat berbeza kerana kurang mod phonon yang aktif. Yang menghairankan, jurang band tidak langsung politype ini adalah lebih luas daripada 2H-SiC, walaupun hexagonality yang lebih rendah dan bersamaan dengan GaN. 9R-SiC juga boleh mempamerkan sifat-sifat pengangkutan elektron yang lebih baik berbanding dengan politypes SiC yang lain disebabkan struktur jalur konduksi yang unik. Oleh itu, ia mungkin sesuai untuk aplikasi frekuensi tinggi dan voltan tinggi.

Keywords: Bahan Dua Dimensi, Silagraphene, Struktur Band Elektronik, Teori
Fungsian Ketumpatan, Raman Scattering

University of Malaya

ACKNOWLEDGEMENTS

I would like to thank Prof. Patrice Mélinon of University of Lyon (France) for countless inputs. This work would not have been possible without his scientific contributions. HRTEM and XPS analyses were performed by Dr. Karine Masenelli and Dr. Olivier Boisron, respectively with generous support from *Centre National de la Recherche Scientifique* (CNRS) of France.

I appreciate interesting conversations with Dr. Muhammad Huda at UT Arlington, USA, Prof. Stephen Pennycook at National University of Singapore, Prof. Yu-Lun Chueh at National Tsing Hua University, Taiwan, Dr. Guoying Gao and Prof. Roald Hoffmann at Cornell University, USA regarding computational methods as well as microscopic techniques.

Lastly, I would like to thank Prof. Ramesh Singh from Faculty of Engineering, University of Malaya for supporting my research and ensuring that I complete this thesis.

TABLE OF CONTENTS

Abstract	iii
Abstrak	v
Acknowledgement	vii
Table of Contents	viii
List of Figures	x
List of Tables	xiv
List of Symbols and Abbreviations.....	xv
CHAPTER 1: INTRODUCTION	1
1.1 Nanotechnology: Trends and Challenges in Semiconductor Industry	1
1.1.1 Polymorphism	8
1.1.2 Importance and Potential Applications	13
1.2 Scope of Research	15
1.3 Objectives of Research	16
1.4 Organization of Thesis	17
CHAPTER 2: LITERATURE REVIEW	19
2.1 Polytypes of Silicon Carbide: Growth and Applications	19
2.2 Exotic Polymorphs of Silicon Carbide	33
CHAPTER 3: METHODOLOGY	45
3.1 Impermeable Plasma Synthesis of SiC	45
3.2 Material Characterization	49
3.3 Density Functional Theory Calculations	51

CHAPTER 4: RESULTS AND DISCUSSIONS	54
4.1 Graphitic Silicon Carbide	54
4.2 Origin of the Tetrahedral SiC Core in Graphitic Onions	74
CHAPTER 5: CONCLUSIONS	89
5.1 Future Studies	90
REFERENCES.....	91
LIST OF PUBLICATIONS	100

University of Malaya

LIST OF FIGURES

Figure 1.1: A conventional planar MOSFET versus Intel's Fin-FET.....	3
Figure 1.2: Representative energy diagrams for various tunneling modes at Si/SiO ₂ interface.....	4
Figure 1.3: Cross section of a typical III-V compound HEMT and its corresponding band diagram at equilibrium	6
Figure 1.4: Crystallographic arrangement of two polymorphs of silica, α - and β -quartz. Distortion of the hexagonal voids between the SiO ₄ tetrahedra is evident in α -quartz..	10
Figure 1.5: Some of the most common polytypes of SiC and their tri-layer stacking sequence in alphabetical order of ABC.....	11
Figure 1.6: A heterojunction made from interface of a 3C- SiC quantum well and bulk 2H-SiC. A quantum well formed by an antiphase boundary (antisite) in 4H-SiC and its corresponding band-edge model.	14
Figure 2.1: Band structure in a 6H-/3C-SiC heterojunction (left) and a schematic depicting a fixed positive charge N_p at the C-face in [0001]6H-SiC which is confined to the interface due to band offset and forms 2DEG.....	29
Figure 2.2: A large-scale STM image (a) along with its corresponding height profile (b) and an illustration (c) showing the monolayer and bilayer of epitaxial graphene on ($\sqrt{3} \times \sqrt{3}$)R30° terrace of 6H-SiC	32
Figure 2.3: Various interplanar spacing in what appears to be multi-walled SiC nanotubes	36
Figure 2.4: Bilayers with Si(C)/C(Si) stacking (a) and Si(C)/Si(C) stacking (b). A trilayer with Si(C)/C(Si)/C(Si) stacking (c) showing a smaller d-spacing between the upper bilayer. 4 layers with Si(C)/C(Si) collapsed into a tetrahedral arrangement.	37
Figure 2.5: Bilayers with Si(C)/Si(C) stacking (top) and Si(C)/C(Si) stacking. The structures on the right show d-spacing after relaxation.	38
Figure 2.6: Lin (2012) has identified this structure as a type of graphitic SiC, however all major XRD peaks can be assigned to either hexagonal SiC (precursor) or graphite (the peaks at 25°, 52° and 55° correspond to [002], [102] and [004] in graphite for example).....	40
Figure 2.7: What Lin et al (2015) have claimed to be quasi-2D SiC has striking resemblance both in terms of morphology and d-spacing to hexagonal SiC nanowires.	41

Figure 2.8: Para-SiC ₃ I (left) and II as well as their corresponding electronic band structure showing the Dirac cone.....	43
Figure 4.1: Side-view of different silagraphene structures before (left, with intentional buckling along c-axis) and after relaxation (middle) along with their interlayer distances. The right panes show top-view of 2x2x2 supercells so that the long-range order is clearer. The color maps represent the total electron density.....	56
Figure 4.2: Energy minimization curve using the density mixing approach for AA' stacking.	59
Figure 4.3: The phosphorene-type SiC with orthohobmic Cmc21 structure (unstable AA').	60
Figure 4.4: Imaginary acoustic modes in the phonon dispersion of the sandwiched flat-buckled hybrid (metastable AA').....	60
Figure 4.5: Phonon dispersion and density of phonon states of monolayer silagraphene (a) and AB' silagraphite (b) with their corresponding electronic band structure and partial DOS in (c) and (d), respectively.	61
Figure 4.6: IR footprint of AB' silagraphite versus that of 3C-SiC.....	62
Figure 4.7: Density of Phonon States for bilayer and trilayer AA and AB shows how the addition of layers shifts the ultralow frequency acoustic modes (ZA) toward imaginary values (below zero).	63
Figure 4.8: A close-up of the CBM in monolayer silagraphene suggesting a highly anisotropic electron mass and mobility.....	64
Figure 4.9: Band structure in different stacking arrangements of bilayer silagraphene .	65
Figure 4.10: Reduction of band gap energy in different arrangements of g-SiC with the increasing number of layers due to quantum confinement.	66
Figure 4.11: Field-emission scanning electron micrographs (FESEM) of graphitic features (sheet, tubes and onions) are depicted (a-c). (d) Several onions are resting on tubular structures. (e) A slightly puckered onion with a barely visible sp ³ -hybridized core (bottom left). (f) The same onion as (e) after several minutes of exposure to electron beams. The diamond-like core has grown larger, tearing open the onion in the bottom left side in the process. (g) Several-layer thick sheet of silagraphene. The magnified region (h) shows how the sheet curls into a tubular/onion-like feature while (i) is a closer view of one of the edges, exhibiting the characteristic interlayer distance of 3.7 Å	68

Figure 4.12: A series of HRTEM micrographs showing onion-like features that exhibit admixture of several interlayer spacing, but predominantly 3.7 Å. The outlined region shows superposition of two onions.	69
Figure 4.13: Line profiles taken from a slightly puckered onion along with its selected area electron diffraction (SAED) pattern. The scatter plot at the end summarizes the repeating measurements of interlayer spacing	70
Figure 4.14: A pair of HRTEM micrographs showing an onion before (top) and after (bottom) the growing diamond-like core tears it open from within.	72
Figure 4.15: Experimental C1s (a) and Si2p (b) XPS signals from the sample along with the simulated core-level C (c) and Si (d) spectra of both AB' silagraphite and 3C-SiC for comparison. Observation of strong surface signals from oxide species is in line with the reactive nature of 2D materials.	73
Figure 4.16: 2H→9R transformation in DFT calculations (left to right).....	75
Figure 4.17: The atomic arrangement of 9R-SiC along c- (top) and b- (bottom) axis. Simulated electron diffraction patterns and the corresponding Miller indices are also shown.	78
Figure 4.18: Simulated XRD profiles of 9R- and 15R-SiC. The asterisks indicate a pair of peaks that are unique to 15R-SiC and do not appear in 9R-SiC. The arrows show slight shift of certain peaks in 9R-SiC as compared to 15R-SiC.....	80
Figure 4.19: Simulated XRD profile of 9R-SiC. The inset shows the crystal morphology as computed using the BFDH method.	81
Figure 4.20: A carbon-rich variation of 9R-SiC with (C:Si ratio of 5:1) is shown. The lattice is compressed by 10% due to shorter C-C bonds (a,b= 2.7 Å, c= 20.42 Å) and the diffraction spots along the c-axis (003, 006 and so on) become significantly prominent.	82
Figure 4.21: Calculated Raman spectra for 9R- and 15R-SiC along with the assigned vibrational modes (top). The stacking sequences of both polytypes are visualized for clarity (bottom, far right). Phonon dispersion curves and phonon DOS of 9R-SiC are also shown.....	83
Figure 4.22: Phonon dispersion curves and phonon DOS of 15R-SiC are very similar to those of 9R-SiC.....	84
Figure 4.23: Electronic band structure and partial DOS of 9R-SiC.....	85
Figure 4.24: Electronic band structure of 15R-SiC is very similar to that of 9R-SiC, but the CBM takes places at the M-point (similar to most hexagonal polytypes of SiC)....	86

Figure 4.25: Electronic band structure of 2H- (top) and 4H-SiC (bottom) as computed using HSE06 functional are shown for comparison..... 88

University of Malaya

LIST OF TABLES

Table 1.1: Some of the most common polytypes of silicon carbide along with their crystallographic and electronic properties.....12

Table 1.1: Some of the most common polytypes of silicon carbide along with their crystallographic and electronic properties.....79

Table 1.1: Some of the most common polytypes of silicon carbide along with their crystallographic and electronic properties.....
...87

University of Malaya

LIST OF SYMBOLS AND ABBREVIATIONS

2DEG	:	Two Dimensional Electron Gas
APB	:	Anti-Phase Boundary (also anti-site)
B3LYP	:	Becke 3-parameter Lee-Yang-Parr (DFT functional)
BFGS	:	Broyden-Fletcher-Goldfarb-Shanno Method
BJT	:	Bipolar Junction Transistor
CBM	:	Conduction Band Minima
CPU	:	Central Processing Unit
CVD	:	Chemical Vapor Deposition
DFT	:	Density Functional Theory
DOS	:	Density of States
EELS	:	Electron Energy Loss Spectroscopy
EDX	:	Energy Dispersive X-ray Spectroscopy (also EDS)
FET	:	Field Effect Transistor
FFT	:	Fast Fourier Transform
FWHM	:	Full Width Half Maximum
GGA	:	Gradient Corrected Approximation (pseudopotential)
HEMT	:	High Electron Mobility Transistor
HRTEM	:	High Resolution Transmission Electron Microscopy
HSE06	:	Heyd-Scuseria-Ernzerhof 2006 (DFT functional)
LDA	:	Local Density Approximation (pseudopotential)
LED	:	Light Emitting Diode
MBE	:	Molecular Beam Epitaxy
MEMS	:	Micro-Electro-Mechanical Systems
MESFET	:	Metal Semiconductor Field Effect Transistor

MOSFET	:	Metal Oxide Semiconductor Field Effect Transistor
PBE	:	Perdew-Burke-Ernzerhof (DFT functional)
PL	:	Photoluminescence
SAED	:	Selected Area Electron Diffraction
SEM	:	Scanning Electron Microscopy
STM	:	Scanning Tunneling Microscopy
UV	:	Ultraviolet
VBM	:	Valence Band Maxima
XPS	:	X-ray Photoelectron Spectroscopy
XRD	:	X-Ray Diffraction

University of Malaya

CHAPTER 1: INTRODUCTION

1.1 Nanotechnology: Trends and Challenges in Semiconductor Industry

Since its inception in the 1960s, semiconductor industry has changed our lives in ways we could have never imagined before. Nearly all appliances that we use today on daily basis take advantage of miniscule semiconductor devices, enabled through extensive use of nanotechnology. Televisions, computer screens and generally any form of backlit liquid crystal display (LCD) are made of hundreds of thousands or even millions (in the case of 4K displays) of tiny light-emitting diodes or LEDs which are basically p-n junctions that emit light due to electroluminescence (electron-hole recombination when voltage is applied). The latest generation of displays takes advantage of nanotechnology to a higher degree. Quantum dot displays (QLED) provide 30-40% more brightness, better color accuracy, lower power consumption and smaller form factor. This technology utilizes the quantum confinement effect, a phenomenon in semiconductor nanocrystals that are smaller than their Bohr radius (e.g. 56 Angstroms for cadmium selenide quantum dots), leading to a transition from continuous to discrete energy bands that correspond to different colors.

Thanks to nanotechnology, a typical smart phone today is 10 times faster than the world's fastest supercomputer back in 1997; IBM's Deep Blue that interestingly got to beat the best chess player in the world, Garry Kasparov. The essential processing units in such smart phones, and generally any modern computer, consist of several billions of field-effect transistors (FET). In FET, an external electric field in form of voltage difference between the drain and source terminals changes the device from an insulator (OFF mode = 0) to a conductor (ON mode = 1), hence creating a switchable logic system. The most common FETs are metal-oxide semiconductor FETs or MOSFETs for

short. In n-type MOSFETs, source and drain are two highly conducting n-type semiconductors, isolated from the p-type substrate by reversed-biased p-n diodes. A metal gate covers the region between source and drain, but is insulated against the semiconducting layers by a highly dielectric gate oxide. A p-type MOSFET on the other hand has p-type source and drain regions embedded into an n-type substrate. In this case, holes flow from the source to drain by a negative gate voltage and they also produce a negative drain current. The distance between the source and drain is known as the gate pitch. A smaller gate pitch means a shorter effective channel length, allowing for high transistor counts, lower gating voltage (lower power consumption) and faster switching.

Back in 1965, Gordon Moore, co-founder of Fairchild Semiconductor and Intel, suggested that the number of components per integrated circuit would double every year. For 50 years, the so-called Moore's Law served as a road map for the semiconductor industry, but in 2016, Intel officially announced that they were unable to keep up with this trend. In 2015, Intel released the new Skylake microarchitecture into the market that used the same 14 nm processing¹ as the older generation (Broadwell). Kaby Lake (2016) and Coffee Lake (2017) also use the same 14 nm processing technology. Cannon Lake, Intel's first commercial 10 nm CPU is expected to be available only in 2018, meaning that Intel has been unable to miniaturize its microchips for 4 consecutive generations now (since 2014). 10 nm node is planned to be followed by 7 nm and 5 nm technologies², however already at 10 nm, quantum tunneling is capable of reducing the device efficiency and reliability significantly, so much so that many experts believe it is better to never go beyond the 10 nm limit and instead explore

¹14 nm refers to the smallest feature in the transistor. Gate pitch in 14 nm nodes are in fact 70 nm or larger.

²Gate pitch is expected to be 32 nm or larger for 5 nm node (originally planned to be commercially available in 2020, now indefinitely delayed).

alternative solutions. Quantum tunneling broadly refers to the quantum mechanical phenomenon where a particle "tunnels" right through a potential barrier that it classically would not be able to overcome. There are generally 3 different types of tunneling that could take place in a MOSFET:

1) Band to band tunneling (also known as Zener tunneling): electrons typically tunnel from tip of the drain, right outside of the gate, into the p-type channel. This is mainly due to overlap of the electric field with halo-doped region (non-uniform doping with high concentrations). The so-called Fin-FET, also called 3D Tri-Gate transistor by Intel³ (see Figure 1.1), was a practical solution that concentrates and maintains the channel (current path) close to the gate. In order to achieve that, a single gate is stacked on top of two vertical gates, allowing three times the surface area for electrons to travel. Beside a smaller leakage, this allows up to 37% higher speed or a 50% reduction in power consumption.

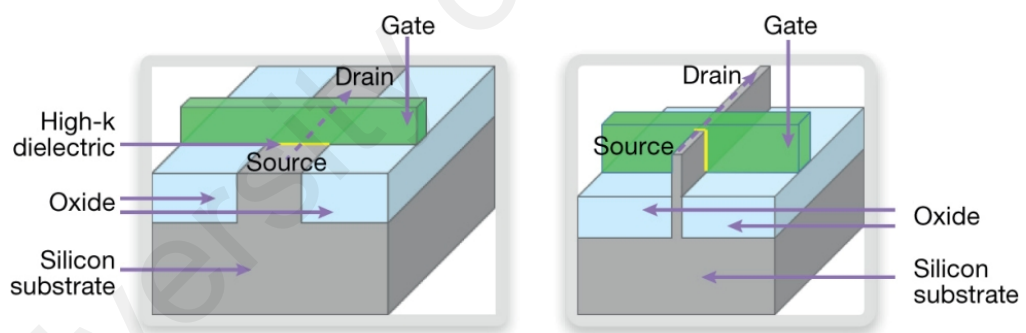


Figure 11.1: A conventional planar MOSFET (left) versus Intel's Fin-FET

2) Direct gate oxide tunneling: in sub-50 nm MOSFETs, the thickness of the oxide gate has to drop at the same rate as the gate pitch, so that a lower voltage could maintain high gate capacitance and drive current. At thickness scales below 2 nm, carriers often tunnel into the gate through the dielectric layer, leading to high power consumption in off-state (standby mode) and reduced device reliability. Intel shipped its first 45 nm

¹Introduced in 2011 with Ivy Bridge microarchitecture (22 nm node).

based processor, the Xeon 5400-series, in November 2007. The new chips introduced high- κ gate dielectrics that allowed increased gate capacitance and minimal leakage. This new technology however added more complexity to the manufacturing process. The commonly used silicon dioxide dielectric gates are readily formed through controlled oxidation of the underlying silicon, ensuring a uniform and high-quality interface. In contrast, common high- κ materials like hafnium silicate, zirconium silicate, hafnium dioxide and zirconium dioxide are usually fabricated using the more expensive atomic layer deposition. These compounds also have band misalignment with silicon and may impact leakage, thermal stability and mobility of charge carriers negatively.

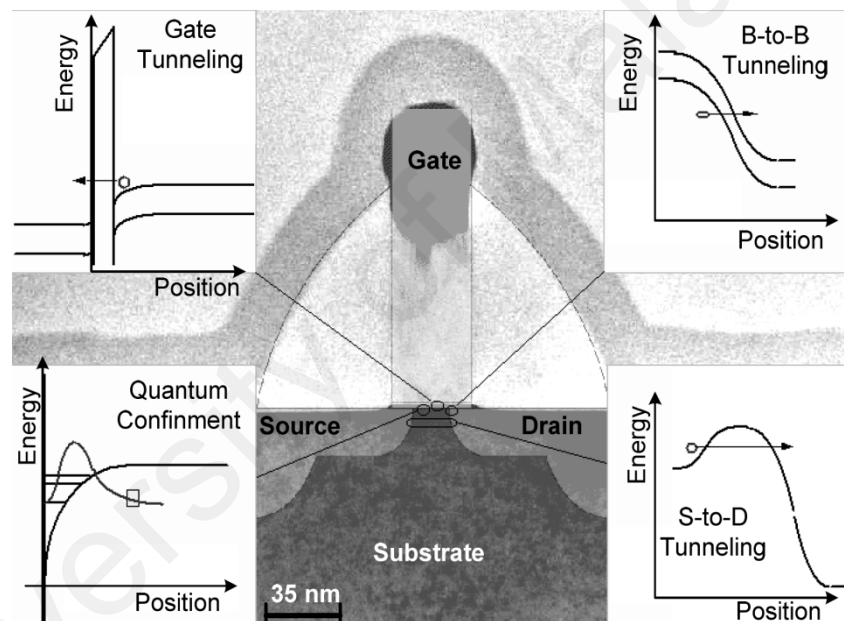


Figure 1.2: Representative energy diagrams for various tunneling modes at Si/SiO₂ interface (Asenov et al, 2002)

3) Source to drain tunneling: in sub-10 nm MOSFETs, charge carriers can tunnel directly from the source to drain due to their nanoscale proximity, without any applied voltage. In extreme cases, a full-fledged quantum tunneling will not only lead to leakage but a total transmission of carriers, meaning that the transistors will always stay in the ON mode and can no longer be switched. Direct tunneling through the channel is a fundamental problem originating from principles of quantum mechanics and there is no easy way to circumvent it. Some experts think that silicon, albeit with some

modifications, could still be used to make faster, but not necessarily smaller transistors. In fact, Intel has been applying strain engineering in the making of transistors with higher mobility since 2002. By putting the layer of silicon over a substrate of silicon germanium (SiGe) which has a larger lattice constant, the bonds in silicon are stretched beyond their normal inter-atomic distance, reducing the atomic forces that interfere with the free movement of electrons. As a result, the electrons in strained silicon can move up to 70% faster.

Many in the scientific community however believe that the era of silicon is coming to an end and we should explore new materials with higher electron mobility. A sizable number of III-V semiconductors such as Gallium Arsenide (GaAs) or Indium Antimonide (InSb) have significantly higher electron mobility, $8500 \text{ cm}^2\text{V}^{-1}\text{s}^{-1}$ and $78,000 \text{ cm}^2\text{V}^{-1}\text{s}^{-1}$ respectively compared to $\leq 1400 \text{ cm}^2\text{V}^{-1}\text{s}^{-1}$ for silicon. (Kalna et al, 2008) Perhaps one of the most interesting III-V compounds is $(\text{GaAs})_x(\text{InAs})_{1-x}$ or simply denoted as InGaAs, a direct band gap, pseudo-binary alloy that is miscible over the entire compositional range from InAs (band gap = 0.34 eV) to GaAs (band gap = 1.42 eV). Lattice parameter in InGaAs increases linearly with the concentration of InAs in the alloy. The most technologically important alloy $\text{Ga}_{0.47}\text{In}_{0.53}$ for example, has a lattice constant of 5.869 Å which is similar to that of InP, another important III-V semiconductor.

A typical FET is basically a homojunction, an interface that occurs between layers of similar semiconductor material. The p-type (positive) silicon contains an excess of holes, while the n-type (negative) has an excess of electrons, but both have an identical band structure. One can achieve high electron mobility, in orders of 50 times that of silicon, by using a III-V semiconductor homojunction, although this is not usually sought-after since the scaling opportunity for such materials would be relatively limited. Silicon-based devices in the last two decades have got at least a 60X boost in

performance and as such, a 50X increase in mobility alone would not warrant a mass adoption of a new technology. Further miniaturization of III-IV devices would also encounter the obstacle of quantum tunneling sooner or later.

A new generation of transistors is currently being developed. The high electron mobility transistor (HEMT) applies the same principles as a typical FET, but instead incorporates a heterojunction (interface with different band gaps) as the channel rather than a doped region.

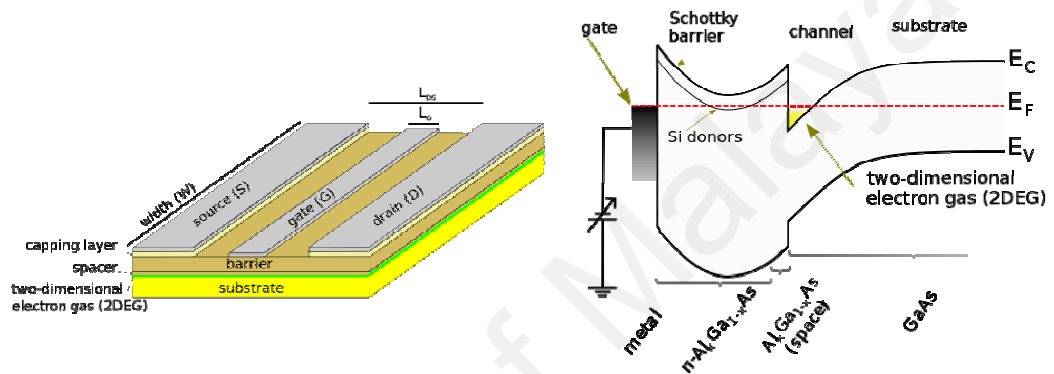


Figure 1.3: Cross section of a typical III-V compound HEMT and its corresponding band diagram at equilibrium

A conventional HEMT (Figure 1.3) usually consists of a n-type Schottky barrier that is placed right under a metallic gate. This layer has excess electrons in its conduction band as a result of doping by donor atoms, a process known as modulation doping because the channel itself remains undoped. The substrate usually has a narrow band gap and attracts excess electrons into its conduction band due to availability of lower energy states. The flow of electrons will cause a change in potential and gives rise to an electric field between the layers which pushes the electrons back toward the conduction band of the Schottky barrier. According to the semi-classical diffusion-drift (DD) transport model, this cycle continues until electron diffusion and drift balance each other out and create a semi-p-n junction at equilibrium. This process leads to an accumulation of electrons at the interface of the two regions, but still inside the substrate which is undoped and has excess charge carrier. In this region, which also acts

as the channel, electrons are trapped in a triangular quantum well and form a two-dimensional electron gas (2DEG), a quantum state wherein electron mobility can reach values in the order of $32,000,000 \text{ cm}^2 \text{ V}^{-1} \text{ s}^{-1}$ (Kumar, 2010) which is nearly 21,500 times that of silicon. By comparison, in a typical MOSFET, 2DEG is only formed during inversion mode when the electrons underneath the gate oxide are confined to the semiconductor-oxide interface.

Another key difference in heterojunctions is a lack of dopants in the channel which means charge carriers are not subject to ionized impurity scattering and can move across from the source to drain with minimal interference. Switching on other hand is similar to homojunctions. The conduction and valence bands throughout the heterojunction are not continuous and must "bend" to deplete the channel or populate it with donor electrons from the Schottky barrier. This "bending" is achieved by applying a gate voltage.

The prospect of InGaAs-based HEMTs look very promising, but despite such advantageous properties, they main never become mainstream in the semiconductor industry. To begin with, the raw materials are far less abundant than silicon which makes up to 27% of Earth's crust. By comparison, Indium is very rare and makes only around 0.000016% of the crust. Furthermore processing of compounds such as GaAs requires costly preparation techniques given the high toxicity of arsenic. An 8" wafer of GaAs costs 5000\$ whereas the same wafer made with silicon goes for as low as 5\$. The low cost of processing for silicon-based devices is thanks to their versatile and flexible applications, from photovoltaic and sensors to displays and microchips. Silicon fabrication facilities are often multipurpose and each process has been carefully optimized for several decades now. New semiconductors like those mentioned above may hold great potentials considering our current needs, but massive transformations in the industry are not going to come cheap. A true successor to silicon must offer at least

a few decades of constant increase in performance, but that may not be necessarily the case with III-V semiconductors.

We highlighted earlier that what makes InGaAs alloys attractive candidates for future devices, beside their high electron mobility, is their ability to be tuned and demonstrate various band structures. This feature however is not unique to III-V compounds. A close relative of silicon, silicon carbide (SiC) has been reported to have over 250 unique atomic arrangements or polymorphs, each with different band structures. Furthermore, Si-C bonds are in many ways similar to C-C bonds and may be able to attain several metastable configurations with sp^2 hybridization. Some of these configurations, collectively dubbed silagraphene, are predicted to incorporate Dirac cones (referring to the conical shapes whose points meet at Fermi energy levels in the band structure). Charge carriers in such materials act as massless Fermions with k -independent Fermi velocities, around 10^6 ms^{-1} and exceptionally high mobility, up to $10^7 \text{ cm}^2\text{V}^{-1}\text{s}^{-1}$.

We are yet to fully understand how SiC evolves at nanoscale into so many different polymorphs, but once we do, we may not have to completely retire our silicon fabrication infrastructures anymore. Even today, carbon doping of silicon is quite commonplace and it is not far-fetched to think these same production methods could be used to grow SiC-based HEMTs one day.

1.1.1 Polymorphism

Most people know or at least have heard about allotropy, the property of some elements that enables their atoms to bond in different configurations. Perhaps the most widely known allotropes are those of carbon. Diamond, graphite and fullerenes are all solids and made of pure carbon, but the atoms in each of them are arranged in a unique way; in a tetrahedral (sp^3 hybridized) lattice arrangement in diamond, in sheets of

hexagonal lattice (sp^2 hybridized) in graphite and in a spherical form with mixed sp^2 and sp^3 hybridization in fullerenes.

The term allotropy is generally used for elements and could indicate non-crystalline (or more broadly non-solid) materials too. Oxygen for example has two allotropes, dioxygen (O_2) and ozone (O_3) that could be solid, liquid or gas. In crystalline materials on the other hand, we tend to use a more specialized term: polymorphism! It is the ability of a solid material to exist in multiple crystallographic arrangements, each having vastly different properties. If polymorphism is due to a difference in crystal packing, it is referred to as "packing polymorphism". If it is a result of different conformers of the same molecule, it is known as "conformational polymorphism". The latter is mostly common in organic compounds. The opposite of this condition is known as isomorphism. Atoms that have similar chemical properties often substitute for one another without changing the crystal structure. This is quite common in minerals and a prominent example is the case of Forsterite (Mg_2SiO_4) and Fayalite (Fe_2SiO_4). Both have the same orthorhombic structure (called Olivine), but in earth's crust, magnesium and iron atoms usually replace each other to form mixed compositions while retaining their original crystallographic arrangement.

The most familiar polymorphic material is silica (SiO_2). Silica has quite a number of polymorphs, the most important of which includes α -quartz, β -quartz, tridymite, cristobalite, coesite, and stishovite. Polymorphs have different enthalpy of formation and may spontaneously convert from a metastable form to the stable form at a particular temperature or pressure. Of special interest are α - and β -forms of quartz which represent a special class of polymorphic materials. Both have identical bonding arrangements, but the position of atoms are very different and appear as if the structure of α -quartz is a distorted version of β -quartz or vice versa. This is because they are low- and high-temperature polymorphs of one another. At $573^\circ C$ ($P = 1$ bar), α -quartz undergoes a

"displacive transformation" (bonds are only distorted, not broken apart as in reconstructive transformation) and rapidly changes into β -quartz. This is a reversible process known as "quartz inversion", during which the unit cells undergo a 0.45% volumetric expansion. Above 870°C, β -quartz transforms into β -tridymite which is stable up to 1470°C and above that, it transforms into β -cristobalite. However if they get cooled very quickly, both β -tridymite and β -cristobalite may be stable at lower temperatures too. Polymorphs that occur outside the temperature range at which they are stable are called *metastable* polymorphs and often will slowly transform (known as disorder-order transformation) into the polymorph that is more stable at those conditions. This process sometimes could take years or decades to fully complete.

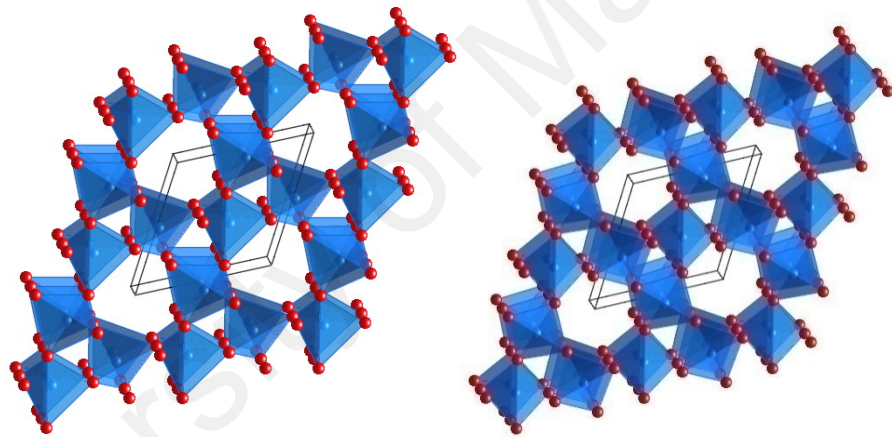


Figure 11.4: Crystallographic arrangement of two polymorphs of silica, α - (left) and β -quartz. Distortion of the hexagonal voids between the SiO_4 tetrahedra is evident in α -quartz

Beside variations in temperature and pressure, a few other factors can influence the crystallization process and lead to the development of different polymorphs. Impurities for example can inhibit certain growth kinetics and favor the formation of metastable arrangements. If the precursor fluid is supersaturated, the atoms from the same compound can also act as "impurities" if they are highly concentrated in a specific region. Other physical parameters such as mixing, solvation and electromagnetic interferences could affect the nanoscale evolution of polymorphic materials as well. In

any case, Ostwald's step rule states that in general the least stable polymorphs tend to crystallize first, so that the increase in entropy is minimal.

A special sub-category of polymorphism is referred to as Polytypism. It is the tendency of a polymorphic material system to have multiple close-packed crystal structures that differ in one dimension only (in simple terms, same structure but with different stacking). SiC for example has more than 250 polymorphs in three crystallographic systems (cubic, hexagonal and rhombohedral), many of which exhibit polytypism (see Figure 1.5).

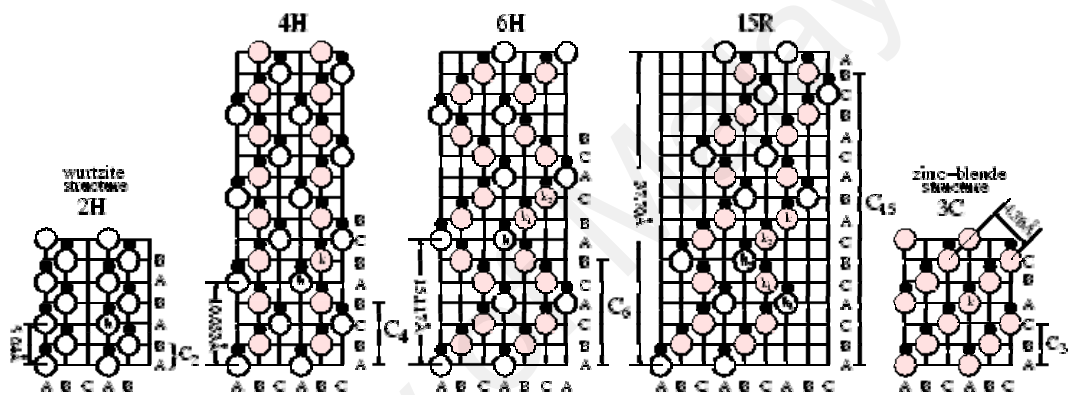


Figure 11.5: Some of the most common polytypes of SiC and their tri-layer stacking sequence in alphabetical order of ABC (Powell & Rowland, 2002)

Despite years of research, the exact mechanism behind the formation of such a large number of polytypes in SiC is somewhat ambiguous. From a theoretical standpoint, short-period polytypes like 3C-SiC and 2H-SiC should be more stable and those with long-period are essentially various stacking configurations of these same basic building blocks. However we do not know what exactly starts this stacking and how far it could go if not interrupted. Some rare polytypes, designated as 393R and 594R have been reported to have a lattice constant of 98.76 nm (Mitchel, 1954) and 149.1 nm (Honjo et al, 1950), respectively. Long-chain stacking appears to be predominantly a rhombohedral feature.

Another hypothesis suggests that long-period structures begin as screw dislocations and the corresponding spiral growth mechanism is the main driving force behind long-

period polytypes. This approach however fails to explain how 3C-SiC undergoes a solid-solid phase transition at high temperatures with 6H-SiC as the only outcome.

In terms of crystallography, all SiC polytypes are made of CSi_4 and SiC_4 tetrahedra except for 3C-SiC, where silicon and carbon atoms are positioned in a slightly distorted manner. Therefore, some *ab initio* models have suggested that polytypism may be related to atomic relaxation of 3C-SiC under metastable conditions. (Käckell et al, 1994)

Table 1.1: Some of the most common polytypes of silicon carbide along with their crystallographic and electronic properties

Polytypes	Space Group	a (Å)	c (Å)	Band gap (eV)	Hexagonality (%)
3C	T_d^2 -F43m	4.3596	4.3596	2.3	0
2H	C_{6v}^4 -P6 ₃ mc	3.0730	5.0480	3.3	100
4H	C_{6v}^4 -P6 ₃ mc	3.0730	10.053	3.3	50
6H	C_{6v}^4 -P6 ₃ mc	3.0730	15.11	3.0	33.3
8H	C_{6v}^4 -P6 ₃ mc	3.0730	20.147	2.86	25
10H	P3m1	3.0730	25.184	2.8	20
15R	C_{3v}^5 -R3m	3.073	37.7	3.0	40
21R	C_{3v}^5 -R3m	3.073	52.89	2.85	28.5
24R	C_{3v}^5 -R3m	3.073	60.49	2.73	25
27R	C_{3v}^5 -R3m	3.073	67.996	2.73	44

From a practical perspective, every stacking configuration of SiC appears to create very distinct electronic structure. All experimentally-recorded polytypes of SiC are

indirect band gap semiconductors. 3C-SiC has the highest level of symmetry (zincblende), and therefore exhibits the best electron mobility ($900 \text{ cm}^2\text{V}^{-1}\text{s}^{-1}$) and saturation velocity because of reduced phonon scattering. At 2.3 eV, it also has the narrowest band gap of all polytypes. 2H-SiC on the other hand is 100% hexagonal (wurtzite) and has the widest band gap at 3.3 eV. In general, there seems to be a linear relationship between hexagonality percentage and a wider band gap (Choyke et al, 1999), although rhombohedral polytypes do not follow this trend, as shown in Table 1.1.

1.1.2 Importance and Potential Applications

According to the statistics portal Statista, annual revenues of the semiconductor industry are expected to reach an accumulated USD 378 billion worldwide in 2017. Today more than ever, there is greater demand for faster, more efficient, and smaller devices. Our modern society craves for an ever-increasing level of processing power to perform sophisticated data analysis and in many ways, our personal devices are the new supercomputers that perform such complex tasks. With quantum size limit looming over the silicon industry, scientists and engineers have started to explore new ways of building microchips. HEMT-based logic made from III-V compounds might be a viable approach in short term, but issues like processing cost, high price of raw materials, environmental concerns and lattice compatibility pose a serious challenge.

One solution, instead of mass migration to a totally new material technology, is to take advantage of polymorphic materials with similar chemistry to silicon. A special category of polymorphic materials known as polytypic materials are even more desirable, given that their crystalline arrangement only change in one direction by stacking of smaller units. Nearly all controlled deposition / growth techniques such as

CVD (chemical vapor deposition) or MBE (molecular beam epitaxy) are also based on vertical stacking principles, making polytypic materials an ideal match.

In this regard, SiC polytypes are perhaps the only materials that fulfill such requirements, and on top of that certainly offer the greatest versatility. These materials, being stacked version of the same building blocks, can seamlessly grow on top of each other, eliminating the need for buffer layers that alleviate lattice mismatch. A polytypic HEMT device could consist of the narrow-band 3C-SiC polytype and a modulation-doped wide-band hexagonal polytype like 2H-SiC could create a gap variation in excess of 1 eV (type II heterostructure), promoting the generation of 2DEG with exceptionally high carrier mobility within the cubic region near the interface (see Figure 1.6).

One might argue that the energy of formation for a particular polytype of SiC is not far enough from any other, and in reality it would be very difficult to achieve high-purity growth of any single polytype. However, several research groups have successfully demonstrated low-temperature growth of 3C-SiC (Sugii et al, 1990) and 6H-SiC (Fissel et al, 1995) on a silicon substrate using both gas- and solid-source MBE, although line defects such as dislocations remain to be dealt with.

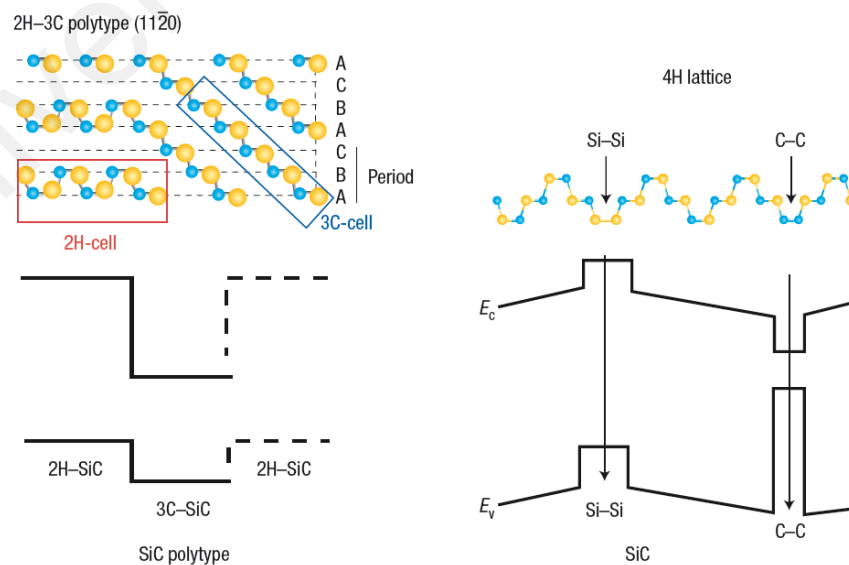


Figure 1.6: A heterojunction made from interface of a 3C- SiC quantum well and bulk 2H-SiC (left). A quantum well formed by an antiphase boundary (antisite) in 4H-SiC and its corresponding band-edge model.

At the same time, it is possible to make heterojunctions using native defects such as Si_C or C_Si antisites. SiC films grown on a Si (001) substrate with terraces show multiple defects including antiphase boundaries (Pirouz et al, 1987). These defects disrupt the original atomic arrangement of SiC, typically along a 2D plane, resulting in replacement of carbon and silicon atoms due to inversion symmetry. As shown in Figure 1.6, this exchange creates a quantum well in form of a pair of homonuclear C–C and Si–Si bonds with strong polarization which originates from a net charge transfer of $0.22|e|$ from the C–C portion to the Si–Si. (Mélinon et al, 2007).

Beside an imperfect substrate, it may also be possible to use a post-treatment technique such as neutron irradiation to create these defects. (Nagesh, 1987) This approach is more compatible with the top-down methodology of today's semiconductor industry.

1.2 Scope of Research

The author's first academic paper (Yaghoubi & Melinon, 2013), an expanded version of which became also my Final Year Project later that year (Yaghoubi, 2013), introduced a new method for synthesis of complex nanomaterials, especially those of endothermic compounds like SiC.

This new technique, also called impermeable plasma synthesis, relies on gas-insulated thermal plasma and its strong ion-screening effect to maintain a high-temperature at its core where ion-ion collisions induce viscous heating. Beside the core, there are also two other regions at the interface of gas and plasma; the outermost *boundary region* where low-velocity gas molecules can pierce into, and the inner *ionization region* where only the fast neutrals are able to penetrate, but get ionized in the process. This interface is diamagnetic due to the flow of transverse electric currents and that is what fuels the screening effect as well as the impermeability.

During the course of this earlier study, a variety of nanostructures from quantum dots and nanowires to nanotubes and nanoclusters were synthesized. Many new nanoscale structures with very peculiar atomic arrangements and unexplainable optical properties were also observed. Perplexed by the results and unable to fully interpret them, the author spent the next 4 years studying the old data as well as generating new ones that could shed light on my previously unanswered questions.

The present work is a compilation of these new insights. XPS results have been carefully re-analyzed and accurate information about the bonding of silicon and carbon atoms have been uncovered. New set of HRTEM coupled with comprehensive image processing helped narrow down a few potential candidates which were further substantiated using DFT models.

1.3 Objectives of Research

- To analyze onion-like structures that appear to be a common byproduct in impermeable plasma synthesis of SiC using meticulous atomic-scale image processing.
- To explain the reproducible interplanar spacing in these onions that suggest the formation of the elusive silagraphene, a sp^2 -hybridized bonding arrangement of silicon and carbon atoms.
- To diagnose the exact composition and crystallographic system of these structures using simulated vibrational and diffraction patterns.
- To analyze their electronic properties.

1.4 Organization of Thesis

Earlier in this chapter, a thorough introduction about some of the challenges the semiconductor industry facing today was given. Quantum size limit and its effect on

downscaling of microchips were discussed and the important role of material properties at nanoscale in common device architectures was highlighted. Some of the more recent solutions like high- κ dielectric layers and Fin-FET architecture are able to reduce certain types of quantum tunneling, but the most critical one, source to drain tunneling remains an issue. As a result, the progress of downscaling toward 10 nm node has been stagnated for a few years now. A recently popular approach was also introduced that instead of miniaturization relies on increasing carrier mobility in the channel using a medium called 2DEG. This medium is created in modulation-doped heterojunctions, referred to as HEMTs, which today are mainly based on InGaAs alloys. Lack of long-term scalability and cost of these III-V compounds have obstructed mainstream applications thus far and the industry is hesitant to completely abandon silicon. Polymorphic materials such as SiC may be an answer to such concerns and therefore the introduction continued with describing the concept of polymorphism and possible driving forces behind it. The introduction ended with underlining viable ways the industry could use SiC polymorphs in fabrication of HEMTs.

In the next chapter, we will delve deeper into the world of polymorphism by reviewing several growth methods and recent applications of SiC polytypes. In order to fully appreciate the versatility of SiC systems, we will then review the general bonding behavior of silicon and carbon atoms and go through some of the more exotic species that have been predicted or observed in recent years. This topic would lead us to the subject of defects in SiC systems and how they affect the overall structure and optoelectronic properties.

Chapter 3 establishes the overall methodology of the study, including synthesis and processing of the samples, material characterization techniques and parameters, as well as DFT models.

In Chapter 4, we will start by discussing the experimental results and implications. The first section is dedicated to structural and crystallographic analysis of graphitic polymorphs while the second section focuses on a previously unknown tetrahedral arrangement.

Finally, \ all the ideas from earlier chapters are gathered and brought together in Chapter 5 to present a conclusive argument. The thesis comes to an end with suggestions for future studies.

University of Malaya

CHAPTER 2: LITERATURE REVIEW

2.1 Polytypes of Silicon Carbide: Growth and Applications

Polymorphism is not a rare phenomenon. Many common minerals such as calcium carbonate (CaCO_3), or Iron Sulfide (FeS_2) are polymorphic and appear in form of calcite (trigonal) and aragonite (orthorhombic), or pyrite (cubic) and marcasite (orthorhombic), respectively. Each of these polymorphs has distinct crystalline structure, appearance and physical properties, however not all polymorphic materials are relevant to the scope of this study. Silicon carbide itself is not the only polymorphic carbide. Tungsten carbide for example is stable as α -WC (hexagonal crystal, space group $P6m2$), as well as β -WC, a high-temperature form ($T > 2525^\circ\text{C}$), which has the rock salt structure (face-centered cubic). (Sara, 1965)

Another prominent example is the special case of boron carbide (B_4C). Polymorphism in boron-rich borides is perhaps more than anything else driven by the ability of boron to form stable covalently bonded networks, just like carbon. Elemental boron has 16 different polymorphs and its stable phase at ambient conditions is yet to be determined, but in general there are 3 major polymorphs; α -rhombohedral and β -rhombohedral (denoted as α -R and β -R, respectively) and β -tetragonal (β -T, also known as T-192). There is also the elusive α -tetragonal phase (α -T) which appears to be formed only when impurities are introduced. (Vlasse et al, 1979) Most of these polymorphs are made of B_{12} icosahedra, but more recently a high-pressure phase (γ - B_{28}) has been reported that remains stable from 19 GPa to 89 GPa in a NaCl-type arrangement of the B_{12} icosahedra and B_2 atomic pairs. Because of the charge transfer between these two

components, the new phase can be regarded as an ionically bonded “boron boride” best represented as $(B_{12})^{\delta-}(B_2)^{\delta+}(B_{12})^{\delta-}$. (Oganov, 2009)

In the last few years, monolayers of boron (named borophene) have also been epitaxially grown onto Ag (111) substrates, first by Mannix et al (2015) in form of B_7 distorted units and later by Feng et al (2016) in form of the so-called β_{12} and χ_3 sheets. Interestingly, it has been predicted that borophene itself could be stable in multiple other polymorphs. (Penev, 2012) Boron nanotubes and B_{80} fullerenes have been computationally shown to be stable too. (Szwacki & Tymczak, 2010) Unlike tungsten carbide that has no significance in the semiconductor industry, boron polymorphs could behave as an insulator, a semiconductor or even a metallic conductor and therefore would be certainly useful in device applications. By extension, nanoscale formations of boron-rich borides, and especially boron carbides (enabling a hybrid between graphene and borophene) could also be of interest. Xu and Bando (2004) for example have reported nanosheets of boron carbide, prepared by induction heating of B_2O_3 and graphite, and subsequently deposition onto hexagonal boron nitride (h-BN) which itself is capable of forming two dimensional graphitic sheets.

Boron and boride polymorphs as well as their potential applications are very promising, but these topics are quite extensive and demand an independent study altogether. Therefore we dedicate the rest of this chapter to the review of SiC polymorphs, their growth conditions and possible applications.

As mentioned in Chapter 1, SiC has numerous polymorphs, but the cubic and hexagonal arrangements are most common. Cubic SiC has only one possible polytype which is referred to as β -SiC or 3C-SiC. Each SiC bilayer can be oriented into 3 possible positions with respect to the lattice while maintaining its tetrahedral formation, hence the notation 3C. If these layers are named alphabetically, then the stacking

sequence would be ABCABC ..., forming a zincblende structure with an indirect band gap of ~ 2.2 eV and a relatively high electron mobility of up to ~ 800 $\text{cm}^2\text{V}^{-1}\text{s}^{-1}$. The first large-scale growth of monocrystalline 3C-SiC is attributed to Nishino et al (1983). Their method, which now is an industry standard, involved the use of chemical vapor deposition with SiH_4 (3% in H_2) and C_3H_8 (0.3% in H_2) as precursor to grow high quality layers on a Si substrate at atmospheric pressure. A buffer layer, grown *in situ* by carbonizing the silicon surface, was used to minimize the effect of lattice mismatch between SiC and Si. 3C-SiC wafers of up to 34 μm thick and several cm^2 in area were prepared after chemically removing the underlying Si layer. Sasaki et al (1984) subsequently measured the electrical properties of such wafers up to 850 $^\circ\text{C}$ in hopes of finding applications in high-temperature sensors and micro-electromechanical systems (MEMS) such as those in turbines and engines. They reported that all the epilayers exhibited n-type behavior with carrier concentration ranging between 5×10^{17} and 1×10^{18} cm^{-3} , and the Hall mobility at room temperature between 120 and 200 $\text{cm}^2\text{V}^{-1}\text{s}^{-1}$. From 400 $^\circ\text{C}$ to 500 $^\circ\text{C}$, Hall mobility dropped to 40 – 60 $\text{cm}^2\text{V}^{-1}\text{s}^{-1}$ and at 800 $^\circ\text{C}$, it further decreased to 20–30 $\text{cm}^2\text{V}^{-1}\text{s}^{-1}$. This level of reduction in mobility is only half as steep as those observed in other polytypes (4H, 6H and 15R), making 3C-SiC the material of choice for high-temperature applications. In the following years, the process of heteroepitaxial growth on Si (100) was further optimized and other research groups managed to increase the size of 3C-SiC wafer to 4" (Zoman et al, 1995) and 6" in diameter (Nagasawa & Yaki, 1997). Today, high-quality 3C-SiC wafers up to 8" in diameter are commercially available from the likes of Anvil Semiconductors (UK) and Air Water Inc (Japan), however defect density remains quite high for certain applications.

In terms of applications, 3C-SiC has been used in a number of devices including MOSFETs, MESFETs, BJTs, Schottky diodes, heterojunction FETs, p-n diodes, sensors

and MEMS. Kondo et al (1986) demonstrated one of the early forms of MOSFETs using heteroepitaxially grown 3C-SiC. Their low-temperature method took advantage of polycrystalline silicon (instead of diffused) as source and drain contacts. The gate insulator was formed by thermally oxidizing the SiC surface. The p-type SiC thin film was isolated from the n-type SiC which becomes conductive at high temperatures. Instead of refractory metals, aluminum was used as the gate metal. The device performance however was not satisfactory. For negative values of gate voltage, the drain current did not saturate even at large drain voltages. The leak current flowing through the underlying p-type SiC appeared to prevent acceptable rectifying characteristics between the drain source and the Si substrate. The authors concluded that a higher quality SiC layer was necessary to achieve improved operation.

Further developments on 3C-SiC MOSFET was not quite successful. Schöner et al (2006) reported that their device (fabricated in a similar manner to that of Kondo et al) showed poor blocking behavior. Under the best conditions, blocking voltages of 100 V were reached with leakage currents below 1 mA. The relatively high leakage current was attributed to extended crystal defects such as stacking faults in the substrate. The maximum Hall mobility at room temperature was only $75 \text{ cm}^2\text{V}^{-1}\text{s}^{-1}$ indicating an unexpectedly high value of the interface trap density of up $4 \times 10^{13} \text{ cm}^{-2}\text{eV}^{-1}$ (two orders of magnitude larger than expected). Interface traps were predominantly ascribed to carbon clusters located in the oxide close to the interface.

Two years later, the same group reported significantly improved blocking voltage and a reduction in leakage current. The authors attributed this to a reduction of planar defects such as antiphase boundaries (APBs) and stacking faults. An APB in 3C-SiC arises at the interface between two adjacent domains when Si and C atoms are replaced by one another. APBs mostly appear when a polar crystal is heteroepitaxially grown on

a non-polar substrate. In the case of 3C-SiC the [111] face which could be either Si- or C-terminated, align with the equivalent [111] plane in the Si substrate, giving rise to two different 3C-SiC domains. APBs are normally eliminated by using a misoriented Si(001) substrate. On the other hand, stacking faults are generated on Si(001) at the interface between 3C-SiC and Si to help reduce the lattice mismatch of 19.7%. To minimize APBs and stacking faults simultaneously, Nagasawa et al (2008) developed a new method that involved growing 3C-SiC on an undulant-Si substrate. Undulant-Si refers to a Si(001) substrate having its surface covered with continuous undulations parallel to the [110] plane.

Thanks to this new method, the authors achieved a high blocking voltage of 600 V with a leakage current of only 100 nA, but mobility in the device was lower than the previous device, indicating that defects may have had both advantageous and degrading behavior.

Another common architecture for 3C-SiC devices is based on a Schottky barrier, a potential energy barrier for electrons formed at a metal–semiconductor junction. If the so-called barrier height (denoted by Φ_B) is large enough, this type of barrier provides rectifying characteristics (conducts current in one direction only) which is a useful feature in diodes. In bipolar junction transistors (BJTs), a Schottky barrier between the base and the collector requires a low junction voltage, preventing the transistor from saturating too deeply, and in turn improving the switching speed. A typical MESFET or even some variants of HEMTs are also based on reverse-biased Schottky barriers which provide a depletion region (similar to p-n junction) that pinches off a conducting channel buried inside the semiconductor.

Yoshida et al (1985) for example fabricated Schottky barrier diodes by evaporating gold onto chemically etched surfaces of epitaxially grown n-type 3C-SiC, and obtained

a barrier height of up to 1.15 eV (about half of band gap in 3C-SiC). In covalent semiconductors, the Fermi level is pinned by the surface states so that the barrier height hardly depends on the work function of metals and is about 1/2 to 2/3 of the energy band gap of the semiconductor. It is therefore possible to achieve higher barrier heights with hexagonal polytypes of SiC that have a wider band gap.

The same group also demonstrated a MESFET device based on Schottky barriers. Yoshida et al (1986) successively grew aluminum-doped p-type and non-doped n-type 3C-SiC epilayers on p-type Si substrates using CVD. Gold and aluminum electrodes were used for Schottky-barrier gate contacts and ohmic contacts (source and drain) for n-type SiC. Carrier concentration and Hall mobility of p-type SiC at room temperature were found to be in the order of 10^{17} cm^{-3} and $\sim 50 \text{ cm}^2\text{V}^{-1}\text{s}^{-1}$, respectively. Non-doped 3C-SiC exhibited n-type conduction and carrier concentration of 3 to $7 \times 10^{16} \text{ cm}^{-3}$ and Hall mobility of 400 to $550 \text{ cm}^2\text{V}^{-1}\text{s}^{-1}$.

3C-SiC has been applied in heterojunction-based devices as well. Kaneda et al (1987) for example used molecular beam epitaxy to grow p-type 3C-SiC/n-type 6H-SiC heterojunction at 1150 °C. 3C-SiC with boron doping was grown on a (0001) n-type 6H-SiC substrate prepared using Lely method (reason being that there is no lattice mismatch between this face and (111) surface in 3C-SiC). Reverse bias characteristics revealed a steep breakdown characteristic similar to the conventional Si p-n junction, but I-V measurements indicated a much higher breakdown electric field, up to $6.6 \times 10^5 \text{ Vcm}^{-1}$. In fact, numerical models by Gao et al (1994) suggest that 6H-SiC/3C-SiC heterojunction bipolar transistors offer better high frequency performance (larger output power and better efficiency) over popular heterojunctions such as AlGaAs/GaAs; although high resistance at the emitter and base ohmic contacts is a limiting factor. It was calculated that contact resistance must be reduced below $1 \times 10^{-4} \Omega\text{cm}^2$ in order to

achieve satisfactory performance. More recently, Lebedev et al (2003) have observed a 0.05 to 0.07 eV blueshift in the excitonic electroluminescence peak of a 3C-SiC/6H-SiC heterojunction suggesting the formation of a quantum well. A similar behavior has been reported in 4H/3C/4H-SiC superlattices as well (Fissel et al, 2001), suggesting that SiC heterojunctions are viable options for fabrication of HEMTs.

In high-temperature sensing applications, 3C-SiC has been one of the most prominent compounds. Pressure sensors for example are critical for advanced industrial, automotive, and aerospace sensing applications. Typical temperatures in such environments range between 200°C to 600°C. Silicon-based pressure sensors relying on piezoresistive or capacitive sensing undergo catastrophic degradation above 500°C. Furthermore, piezoresistive sensors exhibit a strong temperature dependence and experience contact resistance variations at elevated temperatures. To address these problems, Young et al (2004) have demonstrated a capacitive pressure sensor that consists of an edge-clamped circular 3C-SiC diaphragm with a radius of 400 μm and a thickness of 0.5 μm , suspended over a 2 μm sealed cavity on a silicon substrate. The 3C-SiC film was grown epitaxially on a (100) silicon substrate by atmospheric pressure chemical vapor deposition. The fabricated sensor demonstrated high-temperature sensing capabilities up to 400°C. At this temperature, the device achieved a linear characteristic response between 1100 and 1760 torr with a sensitivity of 7.7 fF/torr, a linearity of 2.1%, and a hysteresis of 3.7% with a sensing repeatability of 39 torr.

Resistive hydrogen sensors based on 3C-SiC have also been reported by Fawcett et al (2004). These are of great interest to the fuel cell, automotive, and aerospace industries, mainly for leak detection. In particular, the aerospace and automotive industries require hydrogen sensors that can operate at high temperatures and in highly corrosive environments, whereas typical silicon-based sensors only operate up to 250°C and are

prone to degradation in harsh conditions. The authors deposited NiCr planar ohmic contacts onto a 3C-SiC epitaxial film grown on n-type Si(001) to form a resistive structure. Molecular concentrations as low as 0.33% (in argon), and as high as 100% were detected; whereas similar sensors with silicon saturated already at 40% concentration. Under a constant 2V bias, 3C-SiC sensors exhibited an increase in current up to 17 mA once exposed to pure hydrogen. The sensing mechanism was explained in terms of reduction in surface resistance due to adsorption of hydrogen molecules onto the SiC surface. In this regard, SiC-based sensors appear to employ a similar sensing mechanism as that of oxide semiconductor sensors.

Another active area of research is the application of 3C-SiC in MEMS. Miniscule mechanical resonators offer new prospects for a variety of important applications including accelerometers, gyroscopes, inkjet printers, biosensors and ultrasound transducers. A larger product of Q factor (indicating low loss and high resolution) and series resonance frequency f_s (higher data rate and sensitivity) indicates a better performance in MEMS. Silicon carbide offers an exceptionally large $f_s Q$ due to its low acoustic loss characteristic in the microwave regime. Additionally, 3C-SiC has compatible mechanical and electrical properties with aluminum nitride (AlN), a common piezoelectric material with extensive applications in miniaturized electromechanical acoustic resonators. Lin et al (2012) have demonstrated an AlN/3C-SiC composite piezoelectric resonator with an ultra-high phase velocity up to 32,395 ms^{-1} , a low motional impedance of 91 Ω and a high Q of 5510 at a series resonance frequency (f_s) of 2.92 GHz, resulting in an $f_s \cdot Q$ of 16.1 THz, which is among the highest values reported to date.

In addition to direct applications, 3C-SiC is also used as the substrate of choice for heteroepitaxial growth of some important semiconductors such as gallium nitride. GaN

is a direct band gap material (3.4 eV) with applications in optoelectronic devices such as blue LEDs, near-UV laser diodes (Blue-ray devices), power transistors and HEMTs. GaN thin films were previously grown on silicon wafers due to their affordability, however GaN(0001) has a large mismatch with Si(111), around 17%, resulting in low crystallinity and poor performance. This mismatch against 3C-SiC(111) wafers on the other hand is merely 3.5%. (Takeuchi et al, 1991) Komiyama et al (2006) have argued that beside lattice mismatch, a compatible thermal expansion is also key to growing high-quality GaN. They have shown that microcracks in the GaN thin film still occurred after a 50 nm 3C-SiC buffer layer was grown onto Si(111). Only after a critical thickness of 1 micron was achieved, the cracks were suppressed. The authors concluded that since the thermal expansion coefficient of 3C-SiC ($4.5 \times 10^{-6} \text{ K}^{-1}$) is closer to that of GaN ($5.59 \times 10^{-6} \text{ K}^{-1}$), as compared to Si ($4.2 \times 10^{-6} \text{ K}^{-1}$), 3C-SiC exerts a more uniform thermal stress on the film during crystallization.

Today GaN is almost exclusively grown on 3C-SiC substrates, for example, Cordier et al (2008) have demonstrated a (GaN)-based HEMT grown on 3C-SiC and have compared its performance to that grown on Si(111). Beside stress reduction due to a lower lattice mismatch and a more compatible thermal expansion, 3C-SiC was shown to be less sensitive to the detrimental nitridation effect of ammonia. Ammonia is one of the main precursors in growth of GaN and readily reacts with silicon to form silicon nitride (whereas SiC is more resistant to such reactions). A threading dislocation density below $5 \times 10^9 \text{ cm}^{-2}$ and a 2DEG with a sheet carrier concentration of $1.1 \times 10^{13} \text{ cm}^{-2}$ and a room temperature electron mobility of $2,050 \text{ cm}^2 \text{ V}^{-1} \text{ s}^{-1}$ were achieved.

Among hexagonal polytypes of SiC, 4H and 6H are most common. The case of 2H-SiC is quite interesting. Despite the fact that 2H-SiC is the simplest arrangement of SiC in hexagonal system (with an ABAB... stacking sequence), it appears to be metastable.

Will & Powell (1972) have reported that 2H-SiC transforms into disordered 3C-SiC at temperatures as low as 400°C. They further suggested that phase transformation propagates perpendicular to the c-axis via an axial screw dislocation.

There appears to be a link between impurities and formation of 2H-SiC. (Bootsma et al, 1970) Nitrogen in particular seems to be the most common doping agent to promote 2H arrangement. Messier (1977) reported whiskers of 2H-SiC as a common impurity during synthesis of silicon nitride (Si_3N_4). This whisker-type morphology has been observed rather frequently ever since. Li et al (1990) have reported 2H-SiC whiskers when Si_3N_4 is decomposed at 1900°C in a graphite vessel under nitrogen atmosphere. In other works, 2H-SiC whiskers seem to form along with other nitrides such as AlN. (Zhang et al, 2002) In absence of nitrogen, SiC whiskers normally crystallize in a disordered 3C-SiC structure with stacking faults along the (111) basal plane (Wang et al, 1991) which is consistent with the idea of 2H \rightarrow 3C solid-state phase transformation.

If high-quality 2H-SiC is realized in large scale one day, it could potentially offer a better performance as compared to other hexagonal polytypes of SiC, thanks to its isotropic transport properties. Models by Bertilsson & Nilsson (2002) suggest that cut-off frequency (f_T) in vertical MESFETs on semi-insulating substrates (that require high mobility perpendicular to the surface) can reach 50 GHz at 200 nm lithographic resolutions, as compared to 43 GHz and 12 GHz for 4H- and 6H-SiC, respectively.

3C-SiC transforms into 6H-SiC beyond 1400°C, a polytype with ABCACB... stacking sequence that shows superior stability at high temperatures but only half the mobility of 3C-SiC. However 3C- and 6H-SiC could be grown simultaneously to form a polytypic heterostructure. Powell et al (1991) have reported the homoepitaxial growth of high-quality 6H-SiC films on wafers that were intentionally tilted off the (0001) plane toward the [1120] direction. They showed that it is possible to grow 6H-SiC at

temperatures as low as $\sim 1350^\circ\text{C}$ at which 3C-SiC is stable. Lower tilt angles (below 1°) and carbon-terminated face of the substrate were found to contribute to nucleation of 3C-SiC near planar defects. Where necessary, these nucleation sites could be eliminated by HCl etching of the substrate at 1375°C . More recently, Lu et al (2009) have developed a heterojunction by growing a 3C-SiC epilayer at 1350°C onto a 6H-SiC. The authors observed quantum coherence at low temperatures (1.5K) and using magnetotransport measurements under a magnetic field of $\sim 5\text{T}$, indicating the presence of 2DEG at the carbon-terminated interface of 3C-/6H-SiC (see Figure 2.1). Mobility of the 2DEG was measured to be $2000\text{ cm}^2\text{V}^{-1}\text{s}^{-1}$ and the electron sheet density was about $2.7 \times 10^{12}\text{ cm}^{-2}$.

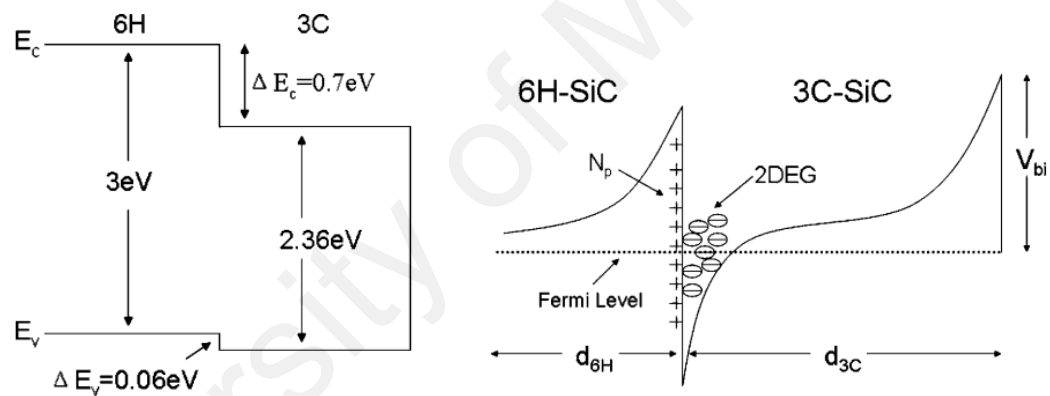


Figure 2.1: Band structure in a 6H-/3C-SiC heterojunction (left) and a schematic depicting a fixed positive charge N_p at the C-face in [0001]6H-SiC which is confined to the interface due to band offset and forms 2DEG. (Lu et al, 2009)

Hexagonal polytypes of SiC have a wurtzite-type structure which lacks a center of inversion. This low symmetry in turn gives them several unique properties. To begin with, the four tetrahedral bonds no longer have equivalent bond-to-bond charge transfer and are slightly ionic, causing an intrinsic spontaneous polarization along the stacking direction. The difference in band gap of different hexagonal polytypes is due to this spontaneous polarization which offsets the conduction band. (Qteish et al, 1992) This also explains why band gap energy varies nearly linearly with the degree of

hexagonality in these polytypes (excluding rhombohedral ones). Lack of inversion symmetry also makes hexagonal polytypes of SiC piezoelectric (generating electric charge under pressure) and pyroelectric (generating a temporary voltage as temperature changes). While the latter aspect has not been studied in detail, Karmann et al (1989) have recorded piezoelectric resonant vibrations with quality factors (Q) up to 100,000 and an electromechanical k_{31} coupling factor of 0.03 for 6H-SiC.

6H-SiC, due to its wider band gap, was previously used in blue LEDs. Edmond et al (1993) demonstrated diodes made from p-type 6H-SiC (aluminum-doped) and n-type 6H-SiC (nitrogen-doped) with a peak wavelength of 470 nm and a spectral half-width of 70 nm. The device exhibited an optical power output of 12 to 18 μW for a forward current of 20 mA at 3 V, representing a 0.02% to 0.03% quantum efficiency. The low efficiency of SiC LEDs is due to their indirect band gap. Today 6H-SiC has been almost entirely replaced by GaN, a direct wide band gap semiconductor, in blue LEDs, although it is still widely used in UV photodiode detectors due to its superior sensitivity and low leakage currents (10^4 to 10^5 times less leakage than silicon-based junctions).

Given that its breakdown electric field strength is significantly higher than that of 3C-SiC, 6H-SiC is also the preferred polytype for high-voltage Schottky rectifiers in power electronics such as industrial invertors. Typical silicon-based Schottky rectifiers can operate at 5 V or lower and have a breakdown voltage below 100 V. They also suffer from excessive reverse leakage currents and a sharp increase in the internal series resistance that limits the forward conduction. SiC-based Schottky rectifiers require a much smaller drift region thickness. As a result, they are normally 18 to 20 times smaller than corresponding Si devices and also offer a reduced series resistance. Breakdown voltage in SiC rectifiers could be as high as 5000 V at 100 A.cm^{-2} (room

temperature) and the forward voltage drop is only 3.85 V for 6H-SiC, as compared to 5.44 V for 3C-SiC. (Bhatnagar et al, 1993)

Furthermore, 6H-SiC could also be used in high-frequency devices with applications in wireless communications and short-wavelength radars operating in the microwave regime. Trew et al (1991) have modeled 6H-SiC MESFETs and shown that RF output powers as high as 65 W could be achieved at 10 GHz.

As a substrate, 6H-SiC has been recently used to grow graphene, an atomically thin but stable form of hexagonal carbon with promising properties for the next generation of electronics. Huang et al (2008) have reported the growth of epitaxial graphene on silicon-terminated 6H-SiC(0001) using high temperature annealing at 1100 °C (see Figure 2.2). This process leads to the decomposition of SiC, followed by desorption of silicon from the surface and an accumulation of carbon atoms to form a carbon-rich surface layer. Ultrathin epitaxial graphene films grown in this manner on SiC can be patterned using standard nanolithography methods, making them compatible with current semiconductor technology. Besides, 6H-SiC acts as a functional substrate with n-type or insulating properties due to its large band gap, however lattice mismatch with graphene remains an issue.

The other common polytype of silicon carbide, 4H-SiC (ABCB... stacking sequence) is perhaps the most commercialized variation, thanks to its superior mobility which is on average 20% higher than that of 3C-SiC. High-quality crystals are normally grown using a modified Lely method. Itoh et al (1994) have reported that if a 6H-SiC(0001) seed is used, cerium impurities are necessary to promote the nucleation of 4H-SiC, whereas if the seed was 4H-SiC(0001), no impurities were required. In both cases however, 4H-SiC could only grow on the carbon-terminated face. The wafers can be grown homoepitaxially at 1500°C and atmospheric pressure using a SiH₄ and C₂H₄ as

precursor and H_2 as the carrier gas. The 4H-SiC(0001) substrate is normally off-oriented toward the (1120) face which is carbon-terminated. Higher tilts angles (as much as 8°) have been shown to improve growth rate.

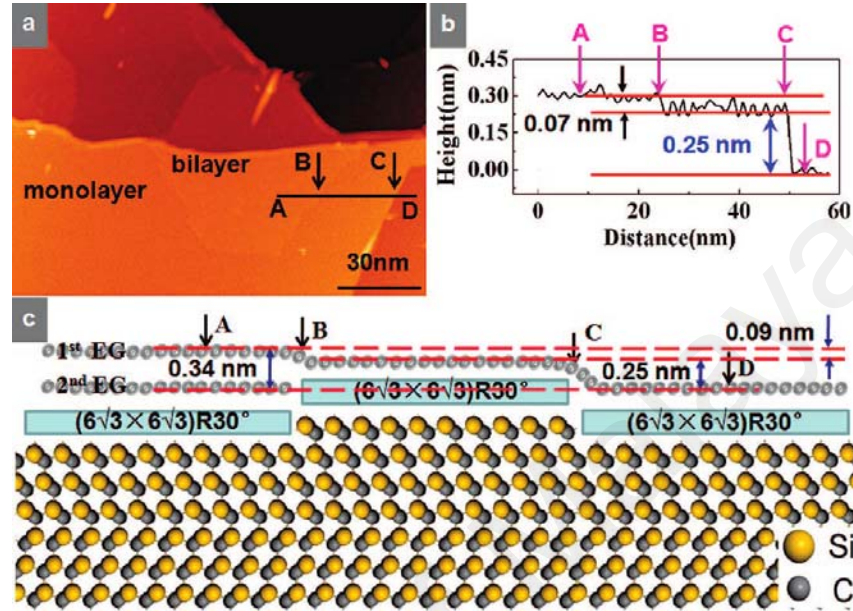


Figure 2.2: A large-scale STM image (a) along with its corresponding height profile (b) and an illustration (c) showing the monolayer and bilayer of epitaxial graphene on $(\sqrt{3} \times \sqrt{3})R30^\circ$ terrace of 6H-SiC. (Huang et al, 2008)

In terms of stability, 4H-SiC appears to be sensitive to impurities. Okojie et al (2001) have reported the formation of stacking faults that give rise to 3C-SiC bands parallel to the [0001] basal plane in a highly doped ($1.73 \times 10^{19} \text{ cm}^{-3}$ concentration) n-type 4H-SiC epilayer following dry thermal oxidation. These stacking faults are formed as the result of nucleation and propagation of Shockley partial dislocations on basal [0001] planes. The associated polytypic transformation is thought to relieve the strain produced by heavy doping. Similar observations have been reported for nitrogen-doped 4H-SiC epilayers as well. Sridhara et al (2001) have shown that these stacking faults could also be formed due to electrical stress during the normal operation of 4H-SiC devices. Such

defects cause local potential fluctuations leading to exciton recombination and a characteristic emission line.

When it comes to industrial applications, 4H-SiC can often replace 6H-SiC in semiconductor devices. Zhao et al (2003) for example have demonstrated record-breaking Schottky barrier diodes with 10.8 kV blocking voltage using a multistep junction termination extension; however most applications involving 4H-SiC take advantage of its high mobility. Yano et al (1999) have reported an inversion channel mobility of $95.9 \text{ cm}^2\text{V}^{-1}\text{s}^{-1}$ for a MOSFET prepared using the carbon-terminated (1120) face, as compared to only $5.59 \text{ cm}^2\text{V}^{-1}\text{s}^{-1}$ for Si(0001).

Additionally, the high mobility of 4H-SiC may prove useful in the fabrication of HEMTs. Polyakov & Schwierz (2005) predicted 2DEG sheet densities of $1.28 \times 10^{13} \text{ cm}^{-2}$ for 4H/3C SiC heterostructures compared to 1.05×10^{13} and $0.81 \times 10^{13} \text{ cm}^{-2}$ for $\text{Al}_{0.3}\text{Ga}_{0.7}\text{N}/\text{GaN}$ and 6H/3C SiC heterostructures. Two years later, Chandrashekhar et al (2007) experimentally verified these results by recording a sheet carrier concentration of $\sim 3 \times 10^{13} \text{ cm}^{-2}$ and Hall mobility of $314 \text{ cm}^2\text{V}^{-1}\text{s}^{-1}$ at 77 K for a quantum well formed by a heteropolytype junction on the carbon-terminated face of 4H-SiC(0001).

2.2 Exotic Polymorphs of Silicon Carbide

A large number of polymorphic semiconductors that form into wurtzite-type crystals by default may also be stable in graphitic arrangements at nanoscale. Freeman et al (2006) have applied *ab initio* DFT calculations to study phase transformation in ultrathin films of SiC as well as ZnO, ZnS, BeO, GaN and AlN. They have demonstrated that thicker films terminating with the polar [0001] surface are stabilized via charge transfer and metallization of the surface layers, whereas thinner films remove the dipole by adopting a graphitic like structure. In the latter case, surface reconstruction promotes a transformation from sp^3 tetrahedral (four single bonds) to sp^2 trigonal planar

coordination (one double bond and two single bonds). This is achieved by simultaneous movement of surface-layer cations inwards toward the slab, and the anions and cations in the second layer towards the surface.

Tusche et al (2007) have reported direct evidence for presence of graphitic ZnO(0001) films on a Ag(111) substrate. The ultrathin layer was composed of two monolayers and exhibited trigonal planar coordination, however it was not completely flat and showed some level of buckling. After deposition of 3 to 4 monolayers, the structure started to transform into the bulk wurtzite structure. The authors attributed this to surface roughening, although Wen & Melnik (2008) have argued that there is a critical threshold before such a transformation occurs. Their model suggests that when the number of ZnO molecules in a nanostructure exceeds 38, from an energy-level perspective, wurtzite-like arrangement would be more stable than graphitic.

Wu et al (2011) on the other hand have suggested that epitaxial strain plays a significant role in the stability of graphitic ZnO. They have shown using first-principle calculations that a ZnO(0001) thin film grown on Pb(111) prefers the graphitic structure up to 17 monolayers. Furthermore, a thicker film may naturally transform into a thinner arrangement to avoid exceeding this threshold, as long as it is subjected to tensile epitaxial strain.

When it comes to graphitic SiC, there are a number of interesting studies, both theoretical and experimental, in the literature. Miyamoto & Yu (2002) are credited with developing the first theoretical models of graphitic and tubular SiC. According to their DFT calculations, a sp^2 Si-C bond on average requires 1.25 eV more energy to form (as compared to sp^3 Si-C) however it should be possible to exfoliate graphitic sheets of SiC from the (111) surface of a hexagonal polytype using extreme hole injection which could be realized by applying a sufficiently large electric field. The authors also rolled

these graphitic sheets into nanotubes that were found to have either direct or indirect band gaps depending on their helicities. In all possible arrangements, Si–C bond length was found to be 1.78 Å (as compared to 1.89 Å in bulk SiC) and there was also a 0.08 Å out of-plane splitting between silicon and carbon atoms.

Coincidentally, within a few months, Sun et al (2002) reported SiC nanotubes (shown in Figure 2.3) that clearly showed a much larger interplanar spacing (3.5 Å to 4.5 Å) than typical carbon nanotubes (3.3 Å to 3.4 Å). Unlike the prediction by Miyamoto & Yu however, Sun et al used a multi-walled carbon nanotube as template. They also measured strong pre-edge absorption peaks at 101.2 eV and 282.5 eV in electron energy loss spectra (EELS) of SiC nanotubes that were not present in SiC nanowires and attributed them to π bonding between Si and C atoms. Since only the outer layers of nanotubes were transformed into SiC and the inner parts were purely made of carbon, the authors concluded that SiC was formed via surface diffusion of Si atoms into carbon nanotubes.

To evaluate their stability, SiC nanotubes were also irradiated continuously with high-energy electron beams (200 kV at 100-150 μ A) for up to 5 minutes. After 15-30 seconds of electron beam annealing, the nanotubes began to collapse, forming curved structures. After 45 seconds, onion-like features with 3.3 Å interlayer spacing emerged. After 1 minute, these onions started to curl even more and self-compress until the interlayer spacing was reduced to 3.2 Å. Shortly after, these onions started to break apart and finally after 5 minutes a cubic structure with the interplanar spacing of 2.5 Å, which is that of [111] planes in 3C-SiC, was formed.

Zhao et al (2005) have studied the electronic properties of SiC NTs. They found that the strain energy in these nanotubes were up to 0.686 eV/atom higher relative to 3C-SiC for (5,5) nanotubes but decreased for larger tube diameters. The authors also suggested

that all SiC nanotubes should be semiconductors regardless of their configuration and their band gap ranges from 0.9 eV to 1.83 eV, increasing with tube diameter (unlike carbon nanotubes, some of which show metallic properties). Zigzag nanotubes appeared to have a direct band gap at the Γ point, while armchair and chiral tubes showed indirect band gap. This exclusively semiconductor behavior was attributed to the higher ionicity of Si-C bonds and the fact that the valence charge density is accumulated around carbon atoms due to their strong $2p$ potential, creating an asymmetric charge distribution. The charge transfer from Si to C was estimated using Mulliken population analysis to be about $0.45|e|$ for (4,4), close to the value $0.6|e|$ obtained by using other *ab initio* calculations. Sun et al (2008) on the other hand have offered a different perspective based on spin-polarized first-principle calculations. They predicted that once SiC nanotubes are unfolded into nanoribbons, zigzag configurations exhibit magnetic and metallic properties (however this appears to be a function of size), while armchair arrangements are non-magnetic semiconductors.

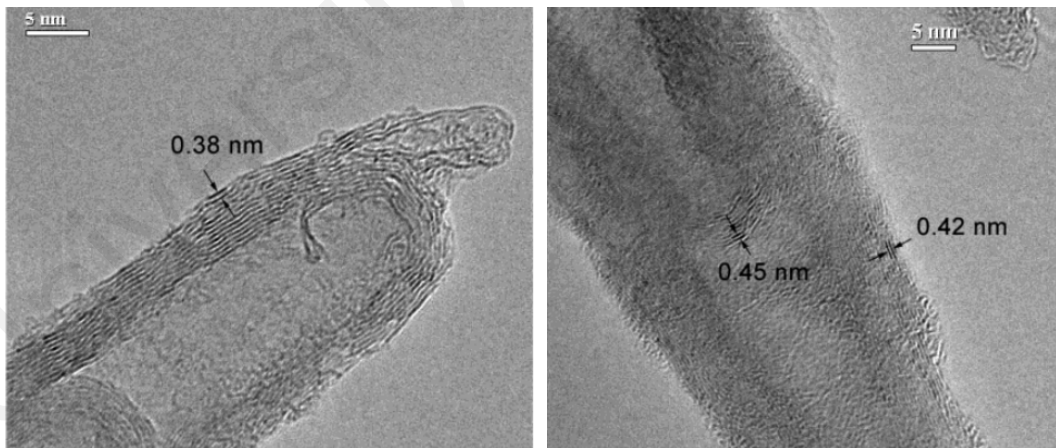


Figure 2.3: Various interplanar spacing in what appears to be multi-walled SiC nanotubes (Sun et al, 2002)

For several years, no study addressed the fact that Sun et al (2002) observed a strangely large variation of interplanar spacing (3.5 \AA to 4.5 \AA) in what was supposedly graphitic SiC. Huda et al (2009) used local density approximation (LDA, supposedly

because of improved performance in weakly interacting systems) to study different stacking arrangements in graphitic SiC. When Si(C) atoms were stacked over Si(C) atoms, the interplanar spacing of the relaxed bilayer was 4.138 Å, whereas if Si(C) atoms were stacked over C(Si) atoms, the same value was 2.136 Å and the monolayers were buckled suggesting strong interlayer interaction and sp^3 tendencies (see Figure 2.4). The SiC monolayer was found to have a direct band gap of 2.544 eV (due to difference in electronegativity of Si and C), while the bilayers had an indirect band gap of 1.855 eV and 1.710 eV for the first and second stacking sequence, respectively. The Si(C)/Si(C) layers seem to be metastable even in large numbers, unless they are compressed, but once 4 SiC monolayers are stacked in the Si(C)/C(Si) sequence, graphitic arrangement no longer forms and strong sp^3 bonding reduces the interplanar distance to 1.986 Å.

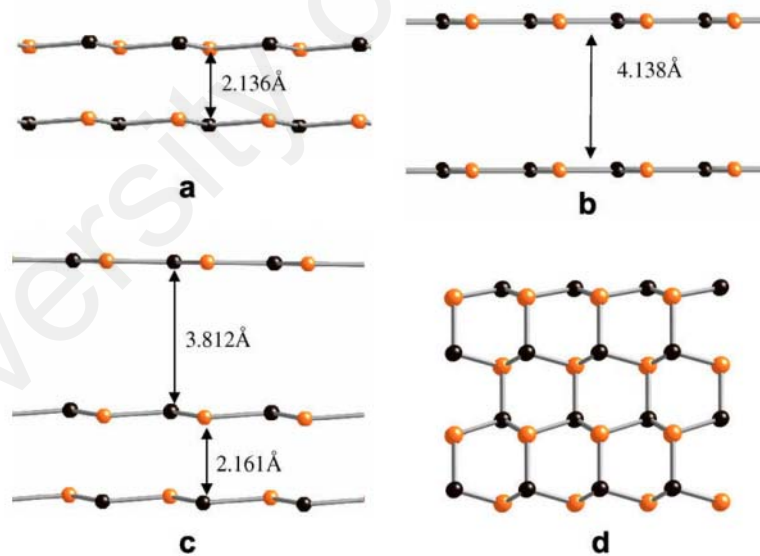


Figure 2.4: Bilayers with Si(C)/C(Si) stacking (a) and Si(C)/Si(C) stacking (b). A trilayer with Si(C)/C(Si)/C(Si) stacking (c) showing a smaller d-spacing between the upper bilayer. 4 layers with Si(C)/C(Si) collapsed into a tetrahedral arrangement. (Huda et al, 2009)

The authors also examined the effect of Si/C ratio on interplanar distance and unexpectedly found out that substitution of one pair of Si atom on top of another in a graphene bilayer leads to a sudden increase to 4.47 Å. In general, there should be a

correlation between low (but non-zero) Si content and larger distances, which could be explained by non-uniform charge accumulation and increase in Coulomb repulsion. In contrast, increase in Si content should promote tetrahedral tendencies.

A year later, Yu et al (2010) approached the same problem from a different angle, using generalized gradient approximation (GGA) and surprisingly arrived at completely different and somewhat contrasting results. The authors showed that no matter the stacking sequence, Si(C)/Si(C) or Si(C)/C(Si), the monolayers relaxed into a completely flat arrangement with 4.47 Å to 4.64 Å (depending on initial distance) and 3.66 Å, respectively (see Figure 2.5). Given that Sun et al (2002) never observed a ~ 2.1 Å distance as Huda et al have predicted, these numbers look more realistic. Their work also suggests that multiple monolayers stacked in a graphitic arrangement could be stable and there is no threshold that would trigger a collapse toward tetrahedral coordination. Furthermore, Si to C charge transfer was lower ($0.32 |e|$) than that estimated by Zhou et al (2005).

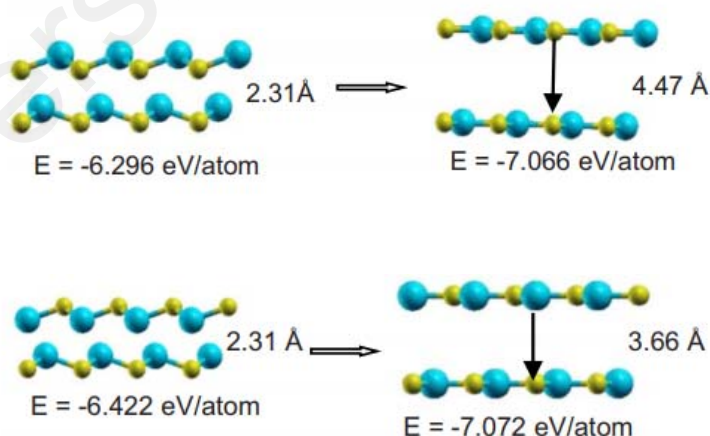


Figure 2.5: Bilayers with Si(C)/Si(C) stacking (top) and Si(C)/C(Si) stacking (Yu et al, 2010) . The structures on the right show d-spacing after relaxation.

In recent years, a number of other research groups have also reported the formation of SiC nanotubes, but most of these works lack any concrete evidence regarding sp^2

hybridization or two dimensional stacking. The atomic arrangements (and potentially polymorphs) of graphitic SiC remain to be deciphered.

For example, SiC "nanotubes" reported by Hu et al (2004), Borowiak-Palen et al (2005), Taguchi et al (2005) or Wang et al (2005) are all in fact made of polycrystalline 3C-SiC. A more recent work by Pei et al (2006) on the other hand may be relevant to the scope of this study. Beside the common 3C-SiC, the authors have also observed layers with 2.6 Å to 3.0 Å interplanar spacing which they attributed to carbon-deficient silicon nanotubes. This proposal is unlikely to be correct, since an increase in Si content should by right promote tetrahedral bonding and smaller d-spacing as a result.

Lin (2012) has claimed to have successfully produced two-dimensional SiC nanoflakes by exfoliating hexagonal SiC crystals using polar solvents such as N-methylpyrrolidone (NMP) and isopropyl alcohol (IPA). This exfoliation technique is commonplace in the case of graphite, where graphene layers are loosely held together using weak van der Waals forces. For SiC on the other hand, hydrofluoric acid is normally used as etchant because Si and C atoms are covalently bonded in a very stable tetrahedral arrangement (similar to diamond). This strong bonding force is what gives SiC its superb mechanical strength as well as its superior performance in corrosive and high-temperature environments. Lin also reports a- and c-axis lattice constant of the "2D SiC" to be 0.266 nm and 0.694 nm, respectively (see Figure 2.6), which are firstly unlike any other theoretical prediction (or experimental observation of Sun et al) and secondly are very close to that of a typical graphite (0.246 nm and 0.67 nm). He has also observed large amounts of graphene along with this "2D SiC" and he attributed them to out-diffusion of Si atoms into NMP. These evidences lead us to believe what Lin has observed is either pure graphene or silicon-doped graphene with slightly modified interplanar spacing. Surface graphitization in hexagonal SiC is an established fact

(Forbeaux et al, 2000) and Nicotra et al (2013) have demonstrated that the carbon buffer layer present on the planar SiC(0001) face delaminates on certain facets of SiC surface steps. Considering the above, it is more likely that Lin's approach was able to exfoliate these quasi-freestanding graphene, some of which may still have traces of silicon in them, rather than exfoliating graphitic SiC from the bulk.

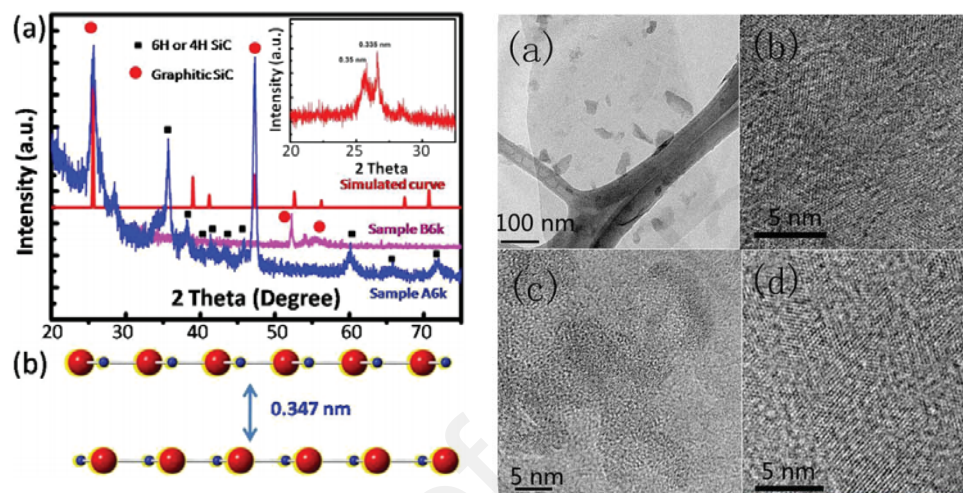


Figure 2.6: Lin (2012) has identified this structure as a type of graphitic SiC, however all major XRD peaks can be assigned to either hexagonal SiC (precursor) or graphite (the peaks at 25°, 52° and 55° correspond to [002], [102] and [004] in graphite for example).

In a more recent attempt, Lin et al (2015) have claimed to have prepared two-dimensional SiC and SiC₂ by diffusing silicon into graphene. Unfortunately, the conclusions once again fall short and fail to provide a convincing trail of evidence. For example, they have reported a lattice parameter of 0.308 nm in a-axis which in fact is equal to that of hexagonal SiC (2H, 4H, 6H, etc all have the same lattice constant of 0.307 nm). They have also observed an interplanar spacing of 0.25 nm along the growth direction of these "quasi-2D SiC" which in terms of morphology happen to resemble nanowires more than a sheet (due to their aspect ratio, refer to Figure 2.7). Gao et al (2012) have also reported SiC nanowires with a 0.25 nm interplanar spacing which is attributed to a [102] growth direction in 6H-SiC. As a result, with great certainty, we can conclude that what has been reported here as 2D SiC is actually a very thin

nanowire of hexagonal SiC. As a further validation to this conclusion, it has to be mentioned that more recently ultrathin flakes of hexagonal SiC with identical lattice parameters have also been demonstrated. (Chabi et al, 2016)

In the case of the supposed SiC₂, the authors have reported d-spacing of 0.44 nm and 0.47 nm, which fall within the same range as that of Sun et al (2002) as well as DFT calculations of graphitic SiC by Yu et al (2010). Lin et al however have identified this as SiC₂ due to a largely disproportionate energy dispersive X-ray (EDX) signal from the sheets, which in reality is not a reliable method to determine concentration of light elements such as carbon, especially in thin specimens.(Eibl, 1993) Zhou et al (2013) have used particle swarm optimization and DFT to develop a 2D planar SiC₂ with a direct band gap of 1.09 eV (and hence suitable for excitonic solar cells), although this arrangement has a lattice constant of $a = 0.502$ nm and the authors have not reported the c-axis d-spacing. The structure predicted by Zhou et al is more stable than an isomeric counterpart with planar tetracoordinate arrangement proposed earlier by Li et al (2010), but the lattice constants for that system (0.286 nm and 0.3879 nm for a and b lattices, respectively) are also not compatible with observations by Lin et al (2015).

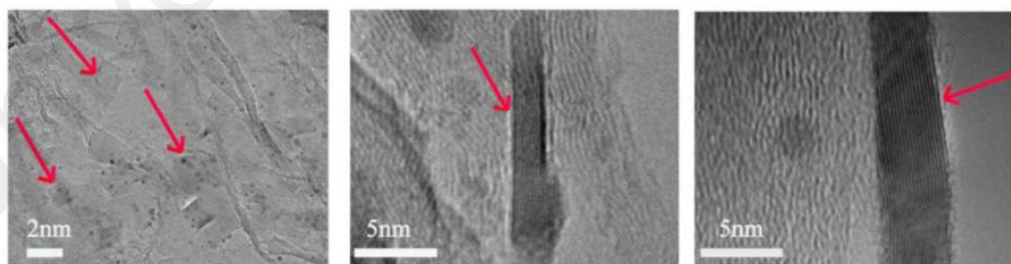


Figure 2.7: What Lin et al (2015) have claimed to be quasi-2D SiC has striking resemblance both in terms of morphology and d-spacing to hexagonal SiC nanowires.

A study by Gao et al (2013) provides a different perspective. They have looked at several candidates and concluded that a graphitic SiC with Si(C)/C(Si) AB stacking is the most stable arrangement, but even then it is 0.99 eV per formula less stable than the

common diamond-like SiC. Interestingly, this arrangement was found to have an interplanar spacing of 3.73 Å, which is within the range observed by Sun et al (2002). Among the relatively more stable structures, there was also a hybrid with alternating silicene and graphene sheets with a d-spacing of 4.4 Å, which is once again very close to experimental measurements in SiC nanotubes.

Unlike all previous studies, Sorokin et al (2014) have come up with a completely new route to achieve sp^2 -hybridized SiC. They have suggested that ultrathin cubic films have a general tendency to graphitize spontaneously. In the case of 3C-SiC, the critical threshold is 3 layers, beyond which the film is more likely to stay cubic. However no interplanar spacing was given for this type of graphitic SiC.

In the same year, Ding & Wang (2014) applied particle-swarm optimization to predict a new carbon-rich form of 2D silicon carbide. Three arrangements of SiC₃ were found to be more stable, the so-called meta-SiC₃ as well as para-SiC₃ I and II. The first structure is a direct band gap semiconductor with strong visible light absorption. It also has a slightly disordered graphene-like structure with $a_1 = 5.66$ Å and $a_2 = 4.76$ Å. Para-SiC₃ I and II on the other hand are both zero band gap semimetals (like graphene) but with a distorted Dirac cone whose Fermi velocities can vary between 54 and 91% of graphene (see Figure 2.8). The former has equal lattice constants of $a_1 = a_2 = 5.63$ Å whereas the latter has a more asymmetric structure with $a_1 = 4.87$ Å and $a_2 = 5.61$ Å.

Dirac cone was originally associated with a honeycomb structure with hexagonal symmetry and equivalent sub-lattices, however Qin et al (2015) have provided a new explanation for the origin of Dirac cones in silagraphene. They have used a combined DFT and tight-binding model to show that 2D SiC featuring Si-Si and C-C pairs (named t1- and t2-SiC) possess Dirac cones while an alternative arrangement of Si and C atoms (named h-SiC) leads to a finite band gap (2.58 eV using GGA-PBE and 3.76 eV using

hybrid functional B3LYP). This behavior was attributed to minimal interactions between Si-Si valence bands and C-C conduction bands. t1- and t2-SiC have a lower energy of formation (by ~ 0.3 eV) as compared to h-SiC (7.076 eV); nevertheless, they are less stable due to mismatch of 0.02 Å to 0.03 Å compared to optimal bond lengths of C-C (1.42 Å in graphene) and Si-Si (2.28 Å in silicene). Si-C bonds were also elongated by 0.03 Å against that of h-SiC.

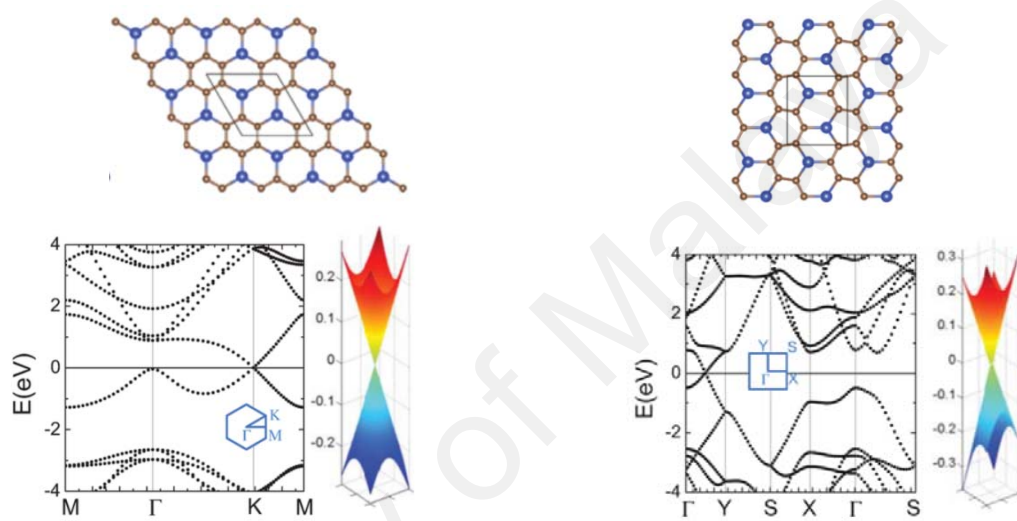


Figure 2.8: Para-SiC₃ I (left) and II as well as their corresponding electronic band structure showing the Dirac cone. (Ding & Wang, 2014)

Very recently, Susi et al (2017) have argued that while the ground state of 2D SiC is planar, there is always a sp^3 tendency between the layers. The authors have looked at several stacking configurations and found that Si(C)/C(Si) AA stacking was by far the most stable (even 41 meV more stable than AB stacking that Gao et al, 2013 found to be most stable). Once the forces were minimized in a bilayer, a d-spacing of 2.32 Å was recorded which is too short to indicate a van der waals interaction. Further analysis of electron density confirmed that there is indeed covalent bonding between the layers; however residual stress prevents the structure from reaching a 3D ground state.

We learned in this section that, just like its numerous polytypes, silicon carbide as a possible graphitic compound is also an extremely complex system which is not fully

understood. It has been established, to some extent, that SiC with at least partially sp^2 hybridization should exist, however its exact structure, level of stability, electronic properties and pathway of formation are among topics that remain to be adequately addressed. There is no general consensus about the default arrangement of graphitic SiC, but given the recent studies, it is likely that there is more than one variation.

Unfortunately, a gap persists until today between theoretical and experimental works. There is a lack of an integrated approach that could bring sophisticated DFT calculations together with atomic scale diagnosis. The aim of this study is to clarify the bonding behavior as well as band structure of different polymorphs of silagraphene and establish their level of stability.

University of Malaysia

CHAPTER 3: METHODOLOGY

3.1 Impermeable Plasma Synthesis of SiC

High-pressure (~11250 Torr) stream of room-temperature argon was used to isolate and focus a DC discharge (300 amperes, 3750 Torr, argon) from a tungsten electrode onto a homogeneously mixed graphite-silicon pellet (1:1 molar ratio) for 30-120 seconds. The samples were extracted from the graphitic features that were deposited within the core region.

Detailed accounts of the experimental setup as well as the rationales behind the process of synthesis have been discussed in an earlier paper (Yaghoubi & Mélinon, 2013). The following summary is taken from this work and highlights the main differences between thermal plasma and impermeable plasma. It also describes various regions in impermeable plasma (core, ionization region, etc) and how graphitic features form.

Thermal plasma because of its broad range of enthalpy is an ideal medium for readily tuning the total energy of a system of reactants. Of particular interest in this scenario is the nature of interactions between plasma and neutrals with regard to its potential applications in synthesis of new materials. In a quasi-steady plasma, these interactions can be subdivided into diffusion of fast neutrals and slow neutrals at the boundaries. If the plasma has a sufficiently high ion density, the slow neutrals which have a relatively lower temperature are readily stopped at the interface between the hot plasma and the cold gas blanket whereas the fast neutrals, due to their higher energies, can somewhat penetrate into the plasma before getting ionized and absorbed. It is apparent that the

temperature and therefore enthalpy of such a gas blanket system gradually increases towards the hotter core region of the plasma where the initial discharge channel under the source is located. At a hypothetical point where the temperature of neutrals gets comparable to that of the core owing to successive ion-neutral collisions, enthalpy reaches a critical value beyond which ionization has a noticeable effect on the plasma equilibrium. The resulting partially ionized boundary layer then effectively separates the plasma from the influx of impinging neutrals by balancing the pressure gradient.

Within this boundary layer, there are at least two distinct regimes each with its own set of properties which can potentially affect the process of synthesis: 1) The outer *boundary region* where only the slow components perturb the steady state and 2) The inner *ionization region* where the fast neutrals are present. The former has a more turbulent nature and lower temperature due to the presence of neutrals while the latter because of the flow of transverse electric currents is essentially diamagnetic and therefore establishes a strong screening effect which minimizes ion loss. This special type of plasma is referred to as impermeable plasma suggesting that incorporation of both ions and neutrals at the boundaries can be closely controlled to give rise to a myriad of structures with customized properties. In this study we report a new method for systematic synthesis of virtually any mesostructure by utilizing these exceptional properties of impermeable plasma at high pressure differences of the order of 7500 Torr. Extremely rapid (typically a few seconds) growth of nanostructured thin films in a controlled manner is also demonstrated which can be attributed to the earlier introduced ion screening effect as well as the dissimilar potentials of non-identical ions.

Impermeable plasma just like any other source of heat can be used to synthesize a variety of materials and we take advantage of a variety of nucleation growth pathways to synthesize distinct nanostructures which closely correlate with characteristics of

plasma considering the temperature density during nucleation and growth are quite different for every structure.

What differentiates impermeable plasma synthesis (IPS) from more conventional approaches is the unique property of its boundary layers which grants us the ability to closely tune the process. In order to control the size of the structures for example, we can simply disturb the growth process by regulating the population of the impinging neutrals which on account of their lower temperature perturb the otherwise homogeneous hot plasma.

Theoretically, the penetration length for fast neutrals exceeds that of slow neutrals by orders of magnitude given their higher energy level and the larger cross section for ion-neutral collisions compared to electron-neutral collisions. However in laboratory experiments, this ratio conversely translates into a wider boundary region as a result of the non-ideal compensation for ion outflux via diffusion. A more practical approach to modifying the extent of each regime therefore would be to monitor the permeability of plasma through different density balance conditions. Assuming an approximate isolation due to ion screening, in any practical case, changing the pressure of the blanket (influx) and the gas used to generate the column of plasma (outflux) can collectively influence permeability via critical density of ions and neutrals at the interface. Consequently, higher permeability of the outermost layers leads to emergence of SiC nanocrystals in the vicinity of the blanket while those regions closer to the ionization region remain in a state of quasi-equilibrium to foster defect free microstructures.

Beyond this outer boundary layer the temperature drop is steep preventing the occurrence of highly endothermic reactions, although nanoparticles may still be obtained. The sudden decrease in temperature has origin in diamagnetic characteristic of the ionization region which effectively confines the ions. Ion screening, along with

element separation, further gives rise to yet another interesting aspect of impermeable plasma; the extremely rapid in situ growth of nanostructured thin films of graphitic features on as-synthesized silicon carbide crystals. It is evident that the morphology of the thin films is also a function of plasma permeability. For example, nanodendrites grown in the close vicinity of the ionization region are largely carbon-based (up to 96%) and therefore the screening of carbon ions was effective. The specific morphology of these nanodendrites can be attributed to perturbation of the quasi-steady plasma by the impinging fast neutrals. This is in agreement with previous observations that dendritic forms obey diffusion limited aggregation a process in which diffusion in a non-steady state is the primary means of transport in the system. In the core region on the other hand, due to relative stability of the plasma, the process of growth takes a different turn.

In principle there are countless structures that can be synthesized using IPS. The relative isolation and the quasi-steady state of impermeable plasma due to ion screening offer a significant level of control over the total energy level in the system and that is how altering any parameter even slightly leads to new products. Achieving such a versatility using a typical thermal plasma is not feasible mainly because of substantial heat conduction via ion loss to the surrounding which can in turn alter the kinetics of reaction. Additionally an arc channel developed under the sole effect of Ohmic heating is limited in dimension to the size of the electrode and is not homogenous owing to lower collision frequency in the absence of screening. In impermeable plasma, on the contrary, the higher rate of ion-ion collisions in the core which is due to ion screening induces viscous heating. For high pressure differences of the order of +7500 Torr (the plus sign indicates higher pressure of the influx), this effect were found to be the dominant source of enthalpy in which case heating is essentially due to dissipation of kinetic energy during Coulomb collisions. Even though this secondary heating mechanism is similar to neutral beam injection in principle, through conservation of

ions in the core, it is to a large extent self-sustaining. For instance, a sample synthesized at 100A for discharge current shows higher yield of synthesis using impermeable plasma (positive flux difference) whereas in another sample, even though the current was threefold (300A) the negative pressure difference (-7500 Torr) made the plasma largely permeable and thus the synthesis had a substantially lower yield. This can be attributed to the fact that in impermeable plasma the highly ionized column rapidly spreads from the initial channel ($1/8$ " in diameter) toward the boundaries generating a homogeneous medium with the same size as that of the torch (1 cm in diameter).

3.2 Material Characterization

Field-emission SEM micrographs were captured on a Zeiss Auriga CrossBeam Workstation model at 3-5 kV using the energy selective backscattered In-lens detector.

HRTEM observations were performed on a JEOL 2010F microscope operating at 200 kV. High Resolution images were acquired using a Gatan Orius 200 camera. Samples were directly deposited onto a Copper 300-mesh grid covered with a holey carbon film without any solvent. Profile analysis and measurements were performed in ImageJ.

Room-temperature XRD was carried out on a PANalytical Empyrean Cu $K\alpha$ diffractometer at a step size of 0.013 degrees.

For core-level spectroscopy, mechanically extracted samples were pressed onto a freshly cleaned indium substrate to avoid charging. XPS measurements were performed

in situ in an ultrahigh vacuum chamber (7×10^{-8} Pa). Deconvoluted peaks were deduced from the fits of the core level lines using a set of Lorentzian and Gaussian curves after subtracting the background signal using the standard procedure developed by Shirley. The main peaks under consideration were Si2p^{1/2-3/2}, O1s and C1s. The XPS spectra were recorded with a CLAM 4 vacuum generator (Al K line at 1486.6 eV), and the photoelectrons were collected at a pass energy of 20 eV in the fixed analyser transmission mode, which gives an FWHM of just over 1.08 eV for the Ag 3d^{5/2} line (reference peak at 368.2 eV).

To perform Raman spectroscopy, A Renishaw's inVia micro-Raman system equipped with an Olympus microscope was used to excite the samples at two wavelengths; 325 nm (UV) from a HeCd laser and 532 nm (VIS) from a YAG laser, both operated at 2 mW with an exposure time of 30 seconds. The scattering was subsequently collected via a front illuminated CCD with Peltier cooling up to -70°C .

Normalized absorption spectra were obtained in the UV-IR range (transmission mode) by depositing BDs from a filtered dispersion of BD/methanol onto a corning glass and subsequently subtracting the background via differential measurement against a virgin glass substrate. PL studies were carried out at 300 K using the Edinburgh Instruments FLS920 fluorescence spectrometer and a 450W Xe arc lamp as the excitation source. PL emissions were analysed at various excitation wavelengths either for a dispersion of raw samples in ethanol or high purity BDs extracted from the supernatant suspension after centrifugation at 10,000 tpm for 5 min and ultrasonication at 37 kHz for 10 min. Chemical etching using a mixture of aqueous HF (40%, 2.5 ml) and HNO₃ (70%, 7.5 ml) at 250°C for 1 hour was applied to remove the passivants and break down the supercrystals into individual BDs through the reaction

$\text{SiC} + 2\text{HNO}_3 + 6\text{HF} \rightarrow \text{H}_2\text{SiF}_6 + 2\text{HNO}_2 + \text{CO}_2 + 2\text{H}_2$ after which the samples were thoroughly washed with deionized water.

3.3 Density Functional Theory Calculations

For graphitic structures, a 2x2x2 supercell derived from 2H-SiC or 4H-SiC (for AA/AA' and AB/AB', respectively) were used for geometry optimization using CASTEP with PBEsol functional (Perdew et al, 2008). The accurate description of long-range interactions such as vdW forces is missing in common DFT methods. Hybrid semi-empirical solutions known as DFT-D introduce damped dispersion correction that is expected to remedy this problem. Among these, the Tkatchenko-Scheffler (TS) scheme (Tkatchenko et al, 2012) is thought to be the most effective. We did apply this method to our geometry optimization; however the results were not satisfactory. For example, AA and AB stacking had nearly identical interlayer distance of 3.8 Å. This cannot possibly be correct given the vastly different interactions of atoms in these arrangements. One would expect the atoms in AA (being right on top of each other) to be more repulsive and naturally enforce a larger distance. Or in another example, AB' stacking was found to have the same interlayer distance as graphite (3.4 Å). This also should be incorrect, given that the introduction of silicon atoms (being significantly larger than carbon) must have at least some impact on interlayer interactions.

We found the PBEsol functional to produce results that not only offered the closest match to our experimental values and previous works in the literature, but also the best convergence values (lowest stress, force, etc). In fact, PBEsol has shown very good performance in the study of other layered structures; comparable to local second-order

Møller-Plesset perturbation approximation (Constantinescu et al, 2013) or DFT-D2 (Tunega et al, 2012).

The reason why DFT-D did not provide the most accurate results is not fully clear, but it could be linked to transferable parameters that are often hard to define accurately in semi-empirical methods like this. All major DFT-D methods largely ignore the substantial variation in properties between effective atoms of the same species. Similar discrepancies have been reported by Bučko et al (2013).

Recently, Gobre & Tkatchenko (2013) have reported that the C_6 coefficient per carbon atom varies by almost an order of magnitude in different nanostructures, with the lowest value found for small fullerenes and the largest for graphene. This mismatch is even more significant between monolayer and few-layer graphene. The carbon-carbon C_6 coefficient of 147 a.u. in the former is 5.3 times larger than that of latter. These findings suggest that the conventional "pairwise" approximation of fixed C_6 coefficient fails even when modelling vdW interactions between the same atoms in different nanostructures, let alone completely different atoms. In the case of silagraphene, a similar issue seem to occur as the TS scheme fails to differentiate between AA and AB stacking.

The energy convergence for the self-consistent calculation was set to 10^{-6} eV/atom, and the structure was relaxed using the BFGS algorithm until the force convergence threshold was below 0.03 eV/Å. Phonon calculations were performed using LDA with either the linear response method (for monolayer and bulk, with a grid separation of 0.05 1/Å for interpolation) or finite displacement method (for finite supercells, e.g. bilayer, trilayer, etc, with a 7 Å cutoff radius). For core-level simulations, a relatively large supercell (4x4x4) was utilized to minimize artificial interactions between periodic

images. To ensure charge neutrality, an extra electron was also introduced into the valence band.

For tetrahedral structures, similar parameters were used for geometry optimization. Phonon calculations were performed using LDA and the linear response method with a grid separation of 0.05 \AA^{-1} for Fourier interpolation. Active Raman modes were obtained by computing displacement derivatives of the polarizability tensor using GGA functional based on the Porezag-Pedersen method. (Porezag & Pedersen, 1996) XRD profiles were calculated using a simulated Cu ($K\alpha$) source with $\lambda_1=1.54 \text{ \AA}$ and a pseudo-Voigt function.

Electron diffraction was simulated using SingleCrystal 3.1.2, a commercially available package by CrystalMaker Software Ltd. The crystal thickness was assumed to be 2 nm, camera length was 100 cm and the beam convergence angle was 1° . Intensity saturation (analogous to beam current) was set to 50. The electron wavelength was fixed at 0.037 \AA which corresponds to a beam voltage of 100.1 keV. FWHM of diffraction spots was 0.02 \AA^{-1} .

Electronic band structures in both cases were calculated using the hybrid HSE06 functional (Krukau et al, 2006) with an ultrafine 0.01 \AA^{-1} grid separation which ensured a minimum of $4 \times 4 \times 4$ Monkhorst-Pack grid for the partial density of states (pDOS), regardless of the size of the primitive cell.

CHAPTER 4: RESULTS AND DISCUSSIONS

4.1 Graphitic Silicon Carbide

Whether SiC could overcome its strong sp^3 preference to form stable 2D arrangements is a matter of debate. Theoretically speaking, Si=C bonds, despite being hard to come by, should be able to replace C=C bonds in a graphitic formation. In fact, DFT calculations suggest that silicon-carbon bond length in silagraphene (1.79 Å) is very close to that of bis-silene (1.77 Å) and quite distinct from that of bulk SiC (1.89 Å), suggesting π -type behavior. (Huda et al, 2009) The very first experimental sighting of what was possibly graphitic SiC was reported by Sun et al (2002) in form of nanotubes that displayed a considerably larger interlayer spacing (3.5 Å to 4.5 Å) than typical carbon nanotubes (3.3 Å to 3.4 Å). A pair of pre-edge absorption peaks at 101.2 eV (Si2p core) and 282.5 eV (C1s core) in EELS was also observed that interestingly did not occur in 3C-SiC nanowires, and hence was attributed to π bonding between Si and C atoms. For several years, this strangely large variation of interplanar spacing (~ 1 Å) in what was supposedly graphitic SiC remained a mystery. Finally in 2009, Huda and colleagues tackled this issue by applying LDA methods to the study of various stacking arrangements. When Si(C) atoms were stacked over Si(C) atoms, the interlayer spacing of the relaxed structure was 4.138 Å, whereas if Si(C) atoms were stacked over C(Si) atoms, this value dropped to 2.136 Å and the planar layers started to buckle, hinting at a strong interlayer interaction with sp^3 tendencies. A year later, Yu et al (2010) approached the same problem from a different angle, using GGA and surprisingly arrived at completely different and somewhat contrasting results. Their calculations showed that Si(C)/Si(C) and Si(C)/C(Si) stacking gave rise to an interlayer

distance of 4.47 Å to 4.64 Å (depending on initial distance) and 3.66 Å, respectively; and regardless of their stacking, the layers remained completely flat.

In elemental 2D materials such as graphene, the effect of stacking sequence on interlayer spacing and band gap structure is negligible. For example the hexagonal AA and AB (Bernal) as well as the less stable rhombohedral ABC graphite have nearly identical interlayer spacing and band structure (Charlier et al, 1992 and Rong & Kuiper, 1993), although the latter exhibits band gap opening under a perpendicular electric field. (Aoki & Amawashi, 2007) In 2D binary compounds such as TMDs on other hand, interlayer interactions are more complex. For instance in MoS₂, there is a strong correlation between stacking configuration and interlayer spacing, that varies between 6.1 Å to 6.8 Å, and also indirect band gap, that varies between 1.3 eV to 1.6 eV. (Gao et al, 2015) Graphitic SiC (g-SiC) appears to behave in a similar fashion; however the interactions between Si-Si, C-C and Si-C atomic pairs are far more intricate due to competing tendencies for sp² and sp³ bonding.

This is probably the main reason why recent literature is fragmented and at times even contradicting. It is entirely possible that just like its bulk form, SiC in two dimensions is stable in multiple arrangements. We can construct at least four basic types of g-SiC in two categories. The first category includes a simple hexagonal stacking wherein Si(C) atoms are either positioned on top of Si(C) atoms (hereafter AA) or positioned over C(Si) atoms (hereafter AA'). The second category consists of a Bernal-type hexagonal stacking wherein Si(C) atoms are either positioned on top of Si(C) atoms (hereafter AB) or positioned over C(Si) atoms (hereafter AB').

Given that bulk SiC prefers a tetrahedral arrangement, we start from two proto-structures with intentional buckling, rather than flat layers. AA and AB stacking can be derived by removing every other layer in (001) direction from 2H-SiC and 4H-SiC, respectively; whereas AA' and AB' stacking are created by simply breaking the bonds

between each layer. These arrangements are shown in Figure 4.1 before and after relaxation.

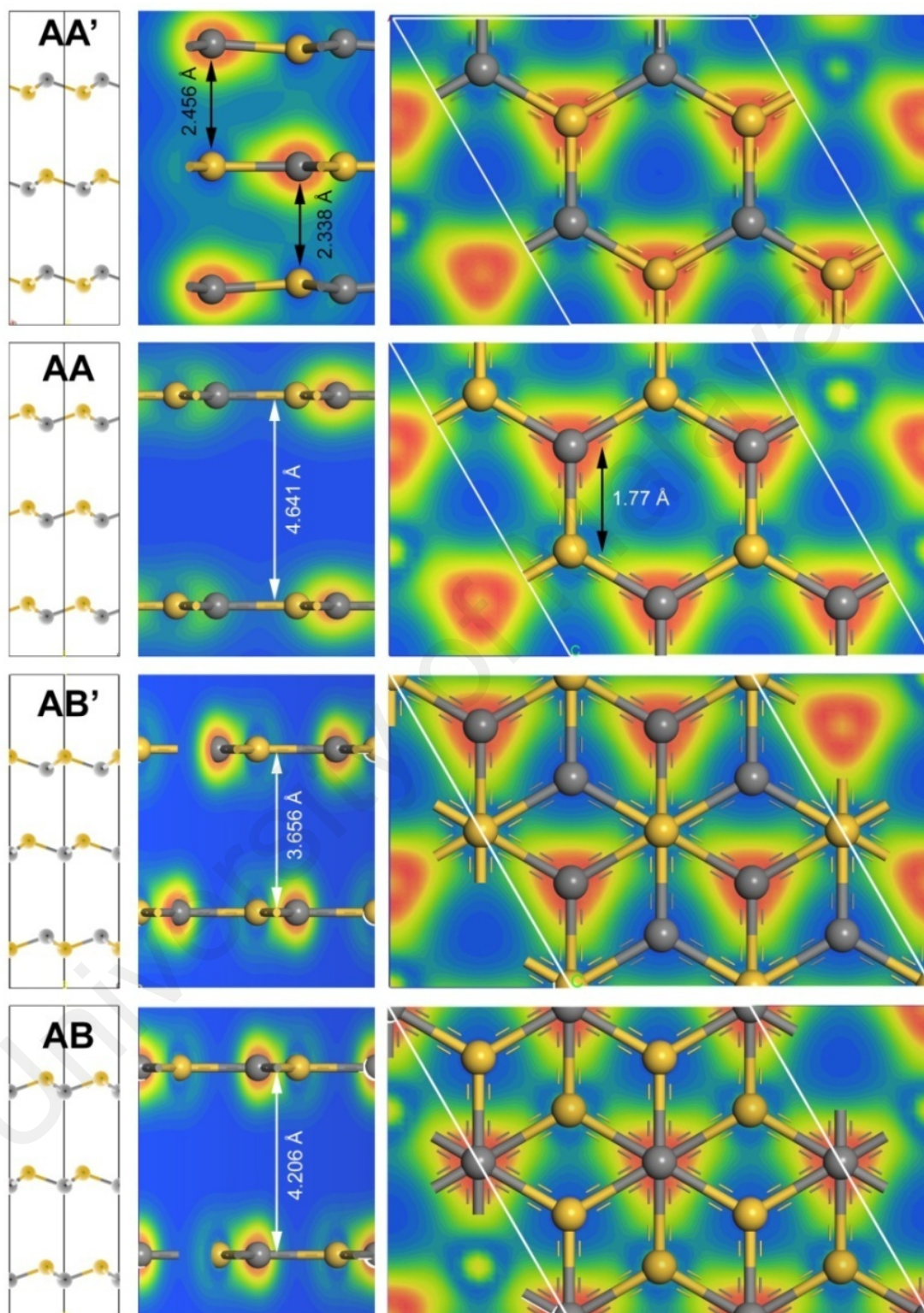


Figure 4.1: Side-view of different silagraphene structures before (left, with intentional buckling along c-axis) and after relaxation (middle) along with their interlayer distances. The right panes show top-view of 2x2x2 supercells so that the long-range order is clearer. The color maps represent the total electron density.

The case of AA' stacking is particularly intriguing. The relaxed AA' structure comprises of a buckled layer sandwiched between two completely flat layers. The average interlayer distance is 2.397 Å which is close to that reported by Huda *et al* (2.136 Å). More recently, Susi *et al* (2017) have also calculated an interlayer spacing of 2.32 Å for AA' stacking which they claimed is the most stable formation of g-SiC. While the individual layers were completely flat, electron charge density isosurface indicated covalent bonding between the layers and the authors concluded that just like silicon, no van der Waals (vdW) bonded layered equivalent of 2D SiC could exist. In contrast, our total electron density calculations (Figure 4.1) suggest that the interlayer interactions are hybrid in nature. At points where the buckled layer is closer to the flat layer (2.338 Å), the behavior is mostly covalent-dominated, whereas in other regions where the interlayer distance is larger (2.456 Å), the interactions are significantly weaker. This peculiar sandwich arrangement is not unique to AA' silagraphene and other 2D materials with high sp^3 tendencies, such as germanene and silicene (that are inherently buckled), were shown to be further stabilized once sandwiched between flat layers of more stable 2D material such as h-BN. (Ni *et al*, 2011)

Interestingly, we calculated an interlayer spacing of 3.656 Å for AB' silagraphene which is nearly identical to that of Yu *et al* (3.66 Å). In both Huda *et al* (2009) and Yu *et al* (2010) a silagraphene wherein Si(C) atoms are positioned over C(Si) atom were considered, but it appears the stacking sequence was different in each study (AA and AB, respectively), hence the seemingly contradicting result. Gao *et al* (2013) have also predicted an interlayer spacing of 3.73 Å for AB' silagraphene which agrees quite well with our conclusion.

The interlayer distances for AA and AB stacking after relaxation are 4.641 Å and 4.206 Å, respectively which are close to the values predicted by Yu *et al* (4.47-4.64 Å)

and Huda et al (4.138 Å), respectively. Beside AA' stacking, the layers in all other types are completely flat.

Next we look at the stability of each arrangement. Evidently, none of these structures are as energetically favorable as any tetrahedral arrangement, which is why graphitic SiC is not common in nature, but the AB' stacking appears to be the most stable, followed by AB (less stable by 579 meV per atom). This is in agreement with Gao et al (2013) who also concluded that AB' stacking is the most stable arrangement (although still 0.99 eV per formula less stable than the common diamond-like SiC). AA' stacking on the other hand has certain qualities that suggest poor stability. For example, Mulliken charge transfer from Si to C atoms is about $0.46|e|$ for the flat layers and approximately $0.003|e|$ lower in buckled layers in large enough (e.g. $3 \times 3 \times 3$) supercells. While miniscule, an unbalanced charge distribution can destabilize the structure. In contrast, Si to C charge transfer value is balanced for all the other arrangements at $0.47|e|$ for AB and AA, and $0.48|e|$ for AB', which are close to the $0.45|e|$ figure derived for SiC nanotubes. (Zhao et al, 2005) This value is significantly smaller, about $0.41|e|$, in tetrahedral SiC, and since it is at its highest in AB', there might be a link between higher ionicity and better stability of graphitic SiC. Similarly, in all stacking arrangements, the Si-C bond length is 1.777 Å whereas in buckled layers of AA', the bonds are stretched by almost 0.5%.

We confirmed this hypothesis, that AA' stacking is not stable, in two ways; firstly, we employed a different electronic minimization technique to make sure that the relaxed structure is not one of the several local minima. By default, all calculations were carried out using E-DFT (Ensemble DFT) scheme which is more time-consuming, but offers superior reliability in terms of convergence. In the case of AA', we also used the density mixing approach (with Pulay mixer and a 0.5 charge mixing amplitude) that calculates the initial electron density from the pseudo-atomic orbitals, rather than randomly

assigned Kohn-Sham wave functions and hence is able to go beyond local minima. (Aarons et al, 2016) As shown in Figure 4.2, we found two major energy minima, with the first one starting around -3,909 eV (for a system of 24 atoms) and slowly decreasing until -3,916 eV (albeit experiencing a sharper reduction beyond -3,913 eV) and then rapidly going down to the global minimum at -3,923 eV. The final structure is surprisingly a tetrahedral formation which is 532.5 meV more stable than the sandwiched flat-buckled hybrid we saw earlier. The resulting system could be easily mistaken for 3C-SiC but in fact is unlike any previously reported polytype and we will further investigate it in a separate study.

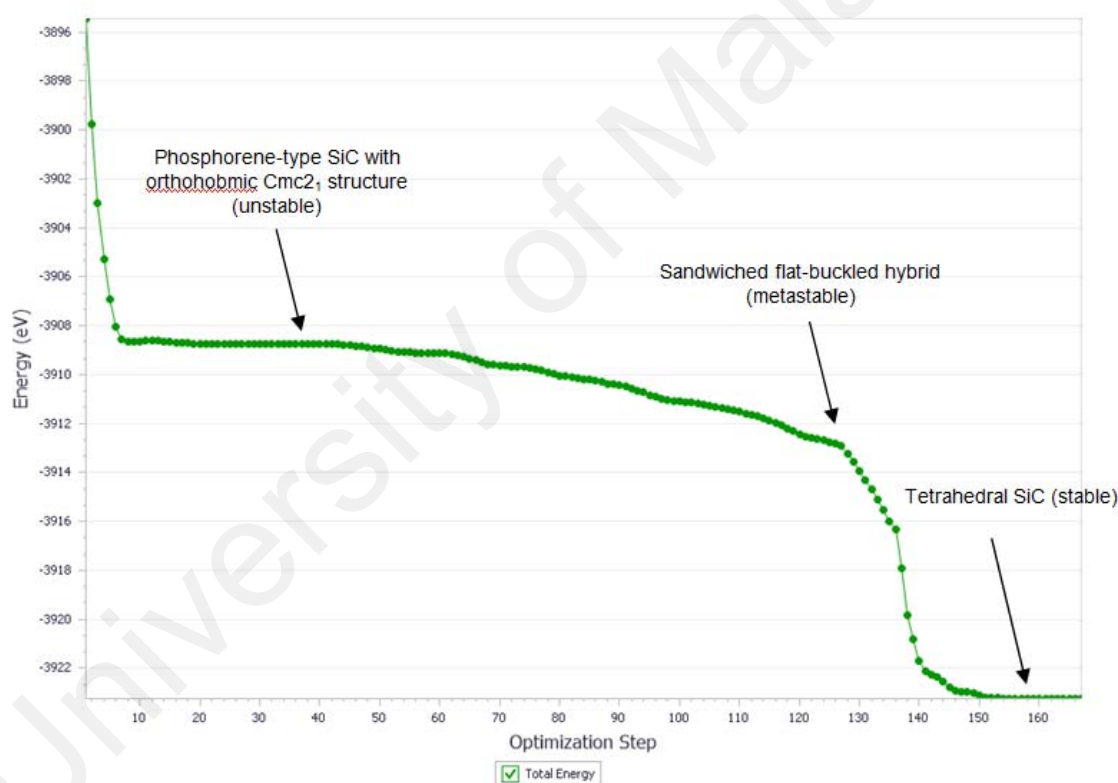


Figure 4.2: Energy minimization curve using the density mixing approach for AA' stacking

There are also less stable 2D arrangements in other local minima, including a phosphorene-type SiC with an orthorhombic $Cmc2_1$ symmetry, stretched Si-C bonds (1.918 Å) and an average interlayer distance of ~ 2.7 Å (see Figure 4.3).

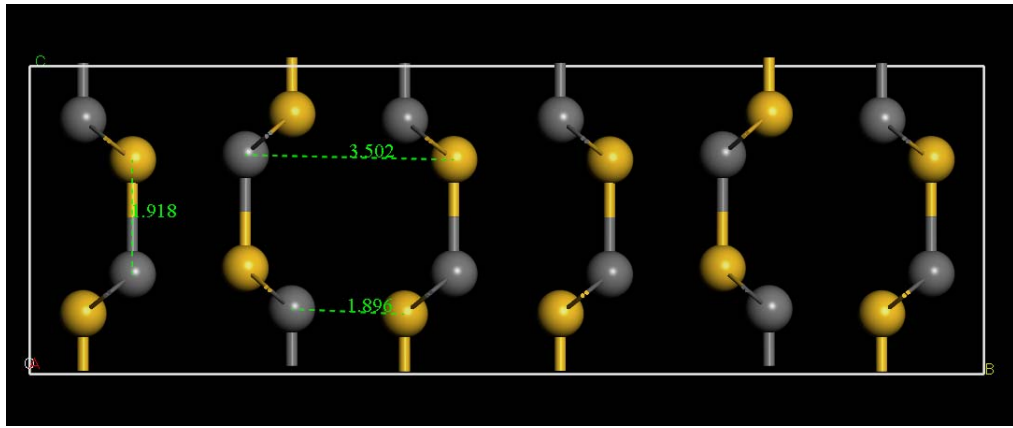


Figure 4.3: The phosphorene-type SiC with orthorhombic Cmc_2 structure (unstable AA')

As a complementary means of assessment, we also performed phonon calculations for the AA' system using LDA. The results included imaginary acoustic frequencies (Figure 4.4) in multiple points in the Brillouin zone, indicating the long-range system is dynamically unstable. However, we have to emphasize that this does not rule out the rare scenario where a buckled layer is coincidentally sandwiched between two stable stacks (such as those of AB') to form a metastable arrangement.

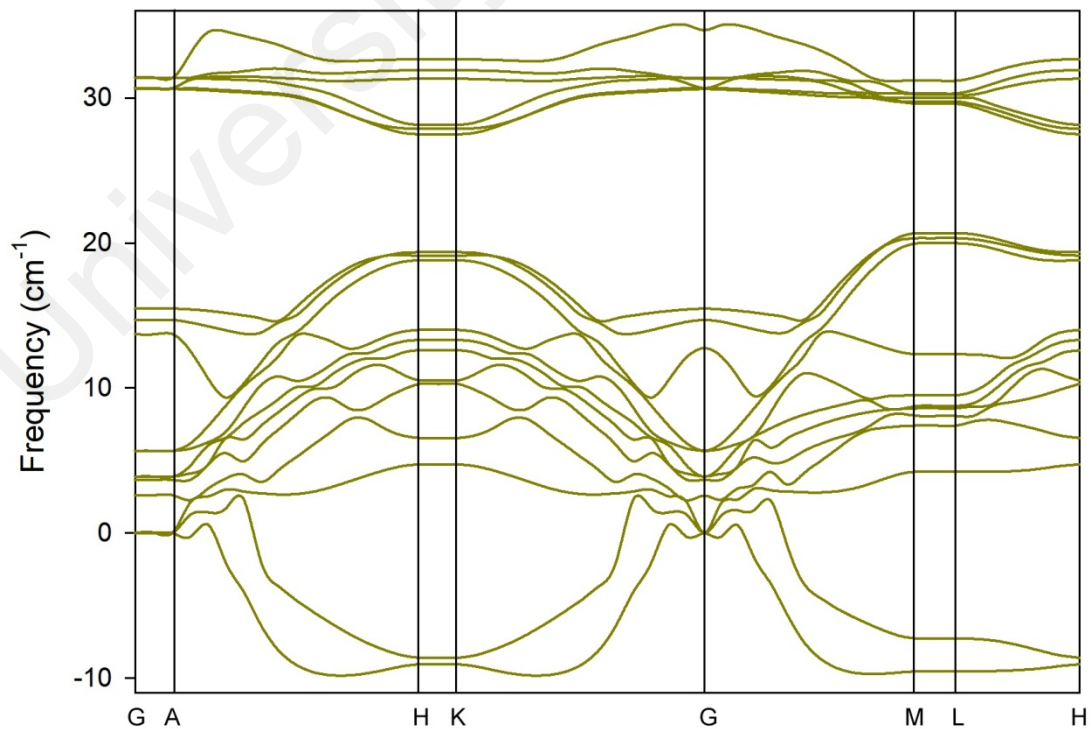


Figure 4.4: Imaginary acoustic modes in the phonon dispersion of the sandwiched flat-buckled hybrid (metastable AA')

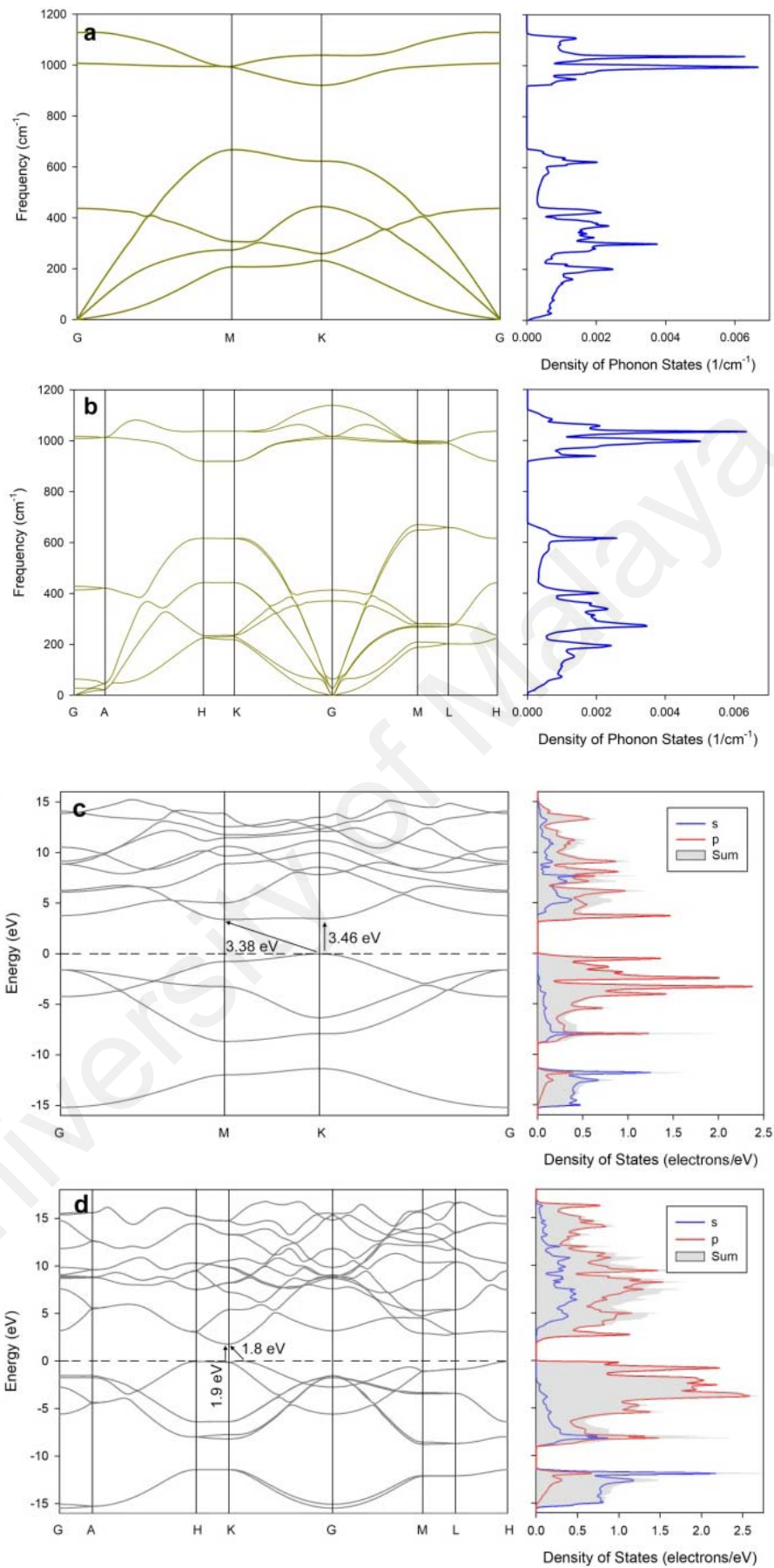


Figure 4.5: Phonon dispersion and density of phonon states of monolayer silagraphene (a) and AB' silagraphite (b) with their corresponding electronic band structure and partial DOS in (c) and (d), respectively.

This exercise posed another question; that whether other arrangements are only stable as g-SiC (rather than bulk) and if yes, how far one could stack them before they become unstable. Starting with monolayer silagraphene (MLSG) and bulk AB' stacking (since it is the most energetically stable formation), we see in Figure 4.5 that both have no imaginary phonon frequencies. In the case of MLSG, phonon dispersion as well as phonon density of states (DOS) are in excellent agreement with previous studies. (Susi et al, 2017) To our astonishment, graphitic SiC also appears to be stable as a bulk material. Given its high energy cost, and the fact that extreme pressure would likely compress it into the tetrahedral arrangement (similar to graphite-diamond transition), we expect to see bulk graphitic SiC, or silagraphite for short, in interstellar media or as a byproduct of thermal discharge.

One can search for the IR absorption of π -type Si-C at 1018.5 cm^{-1} which is quite distinct from that of tetrahedral Si-C at 799 cm^{-1} (see Figure 4.6).

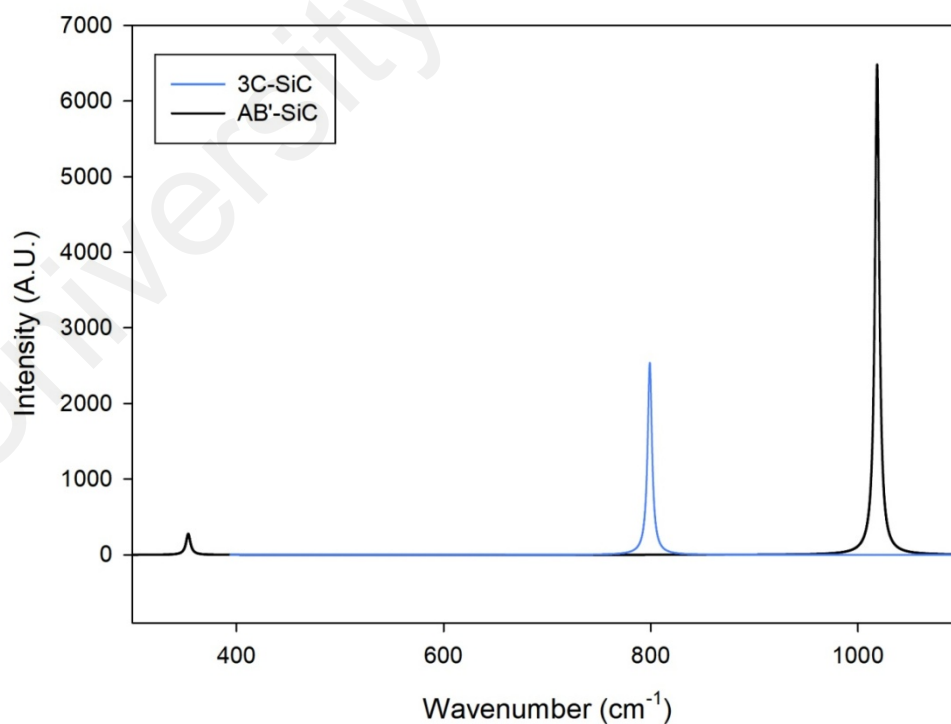


Figure 4.6: IR footprint of AB' silagraphite versus that of 3C-SiC

In the case of AA and AB stacking, the stability threshold is much lower. As we added layers to the stack, ultralow-frequency phonons ($<50 \text{ cm}^{-1}$), especially out-of-plane acoustic modes (ZA) began to shift toward and below zero. This trend is clearly visible in the DOS graphs of Figure 4.7 and hence we expect that anything thicker than a trilayer would make AB and AA slabs increasingly unstable.

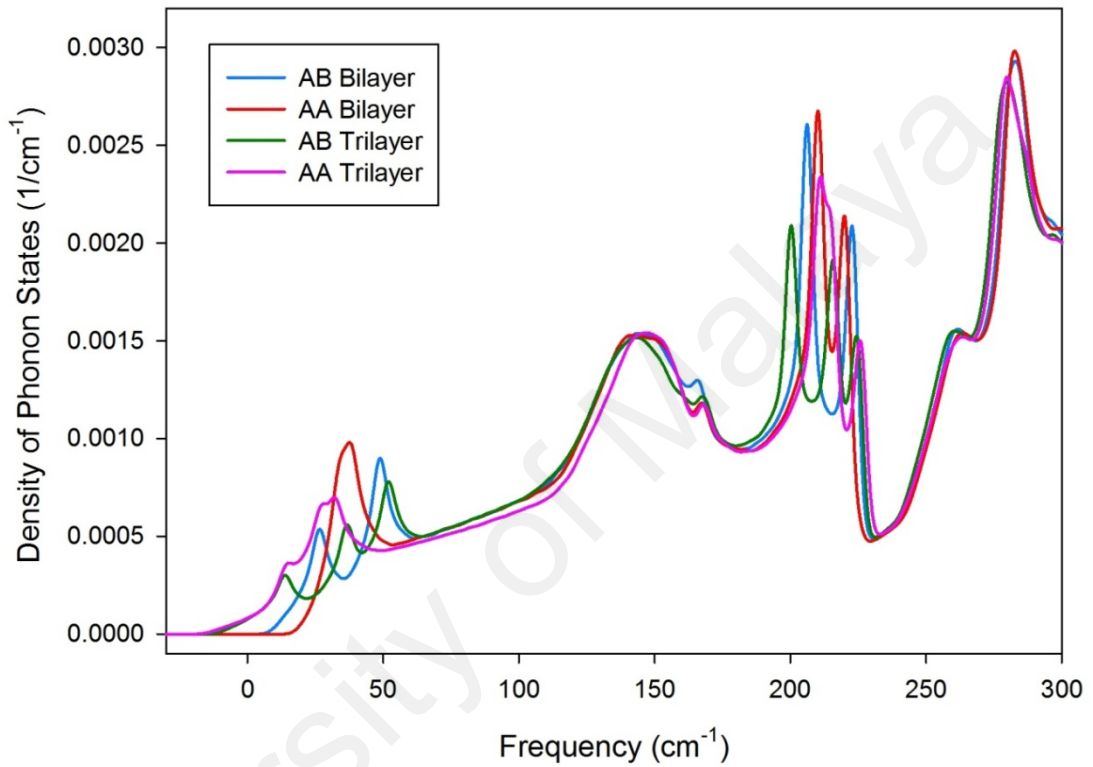


Figure 4.7: Density of Phonon States for bilayer and trilayer AA and AB shows how the addition of layers shifts the ultralow frequency acoustic modes (ZA) toward imaginary values (below zero)

Another interesting revelation is the band structure of monolayer and few-layer silagraphene. Previous studies, either based on GGA (Lin et al, 2013 and Yu et al, 2010 and Susi et al, 2017) or LDA (Huda et al, 2009) have all predicted a direct band gap of approximately 2.5 eV for the monolayer and attributed it to the high ionicity as well as the symmetry-breaking between the Si and C hexagonal sublattices. It is well-known that these cost-efficient approximations grossly underestimate the band gap and hence we conducted our studies using the more accurate but computationally expensive

HSE06 (Heyd-Scuseria-Ernzerhof), which is a screened exchanged (SX) hybrid functional. (Heyd et al, 2005) Sample runs for reference systems such as 3C-SiC and 6H-SiC yielded band gap values of 2.145 eV and 2.905 eV, respectively which are extremely close to experimental measurements (2.2 eV and 3.0 eV, respectively). As shown in Figure 4.5, we found the indirect (K-M) and direct (K-K) band gaps of MLSG to be very close at 3.38 eV and 3.46 eV, respectively. These figures somewhat follow the wide-gap trend based on Gutzwiller (GW) approximations (Hsueh et al, 2011) which have yielded values starting from 3.66 eV but even as high as 4.42 eV (without and with Coulomb truncation, respectively).

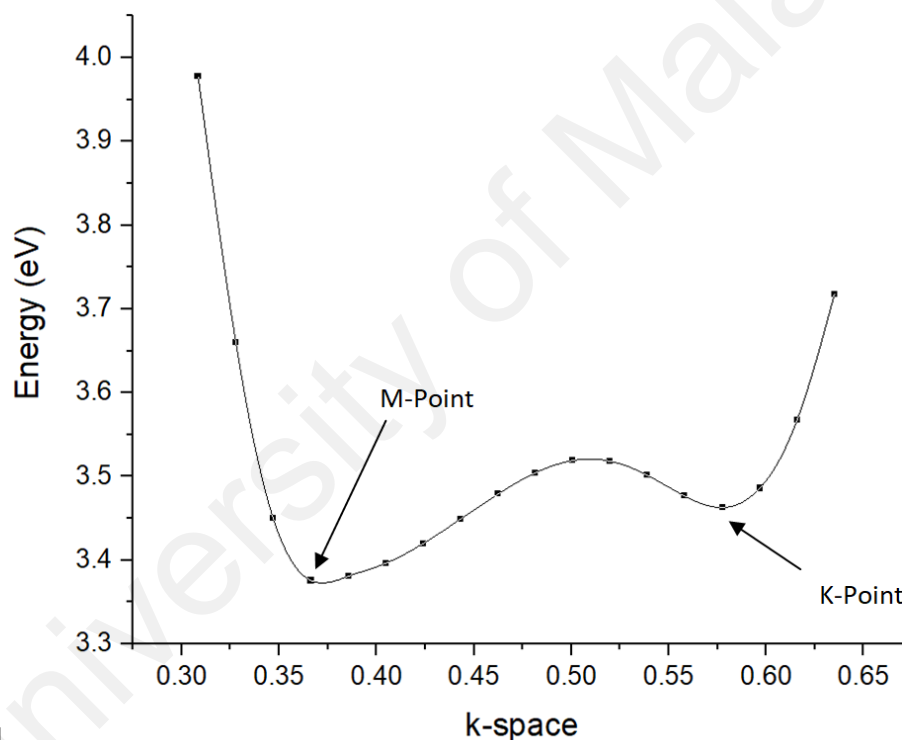


Figure 4.8: A close-up of the CBM in monolayer silagraphene suggesting a highly anisotropic electron mass and mobility

The extremely narrow difference of 0.08 eV between direct and indirect gaps (refer to Figure 4.8 for a close-up view of CBM essentially indicates that the electronic properties could be heavily influenced by changes in residual strain or otherwise ambient interactions such as pressure, temperature or adsorption. This could prove

useful in the development of a diverse array of sensors. More interestingly, CBM are nearly non-dispersive (i.e. flat) along the M-K portion of the Γ -M-K- Γ high-symmetry line, meaning that electrons could behave as heavy fermions in one direction while having relatively higher mobility in another. This level of electron transport anisotropy does not only offer unique technological possibilities such as multi-directional devices, but also works as a highly degenerate system that would support the formation of strongly correlated states with anomalous magnetic properties. (Zheng et al, 2014) In silagraphite, the condition is reversed and the VBM is quite flat near the K-point, suggesting that hole transport would be highly anisotropic. The highest point in VBM is in fact slightly shifted to the right of K-point (hereafter K') and while the direct band gap (K-K) is 1.9 eV, the indirect gap (K-K') is slightly narrower at 1.8 eV. In AB' g-SiC (Figure 4.9) in contrast, the K-K and K-K' gaps are about the same (within 0.01 eV).

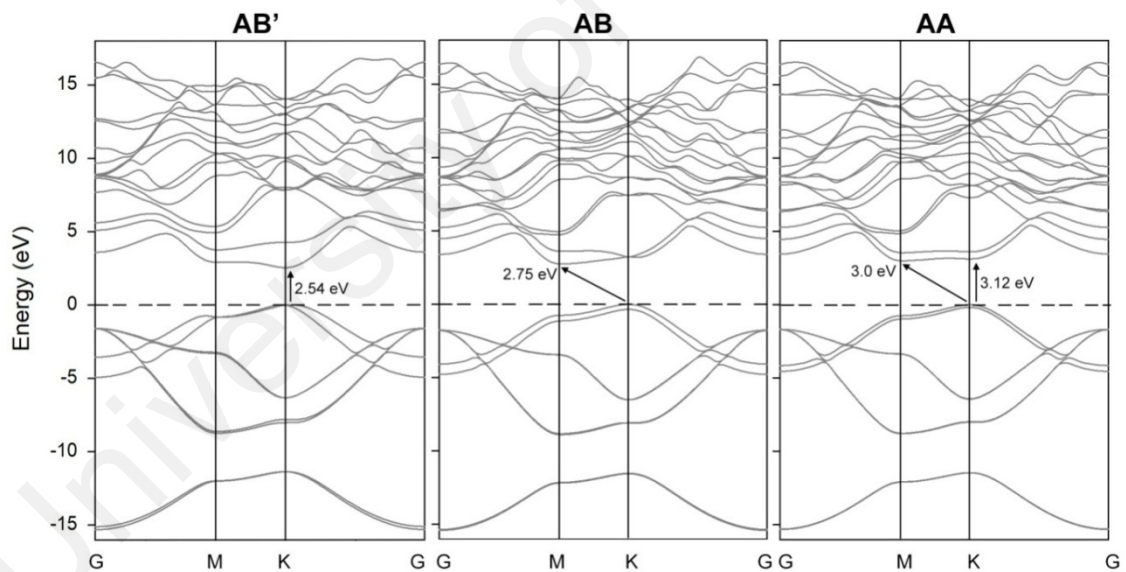


Figure 4.9: Band structure in different stacking arrangements of bilayer silagraphene

Bilayer AB' has a direct band gap of 2.54 eV, but with addition of more layers, the band gap becomes narrower and the K' peak becomes more prominent. This could explain the band gap transition from direct in g-SiC to indirect in silagraphite. The

threshold for this transition is shown in Figure 4.10. At 6 layers and above, the K-K gap becomes equal to that of silagraphite (1.9 eV).

Looking at the partial DOS, in both MLSG and silagraphite, we observe that unlike sp^3 -hybridized SiC where s-orbital contributes significantly to the band edge, sp -hybridization takes place much farther from the CBM.

AA bilayer also exhibits the characteristic CBM similar to MLSG, however as shown in Figure 4.9, the direct gap (3.12 eV) is easily distinguishable from the indirect gap (3.0 eV). AB bilayer on the other hand has an indirect band gap of 2.75 eV.

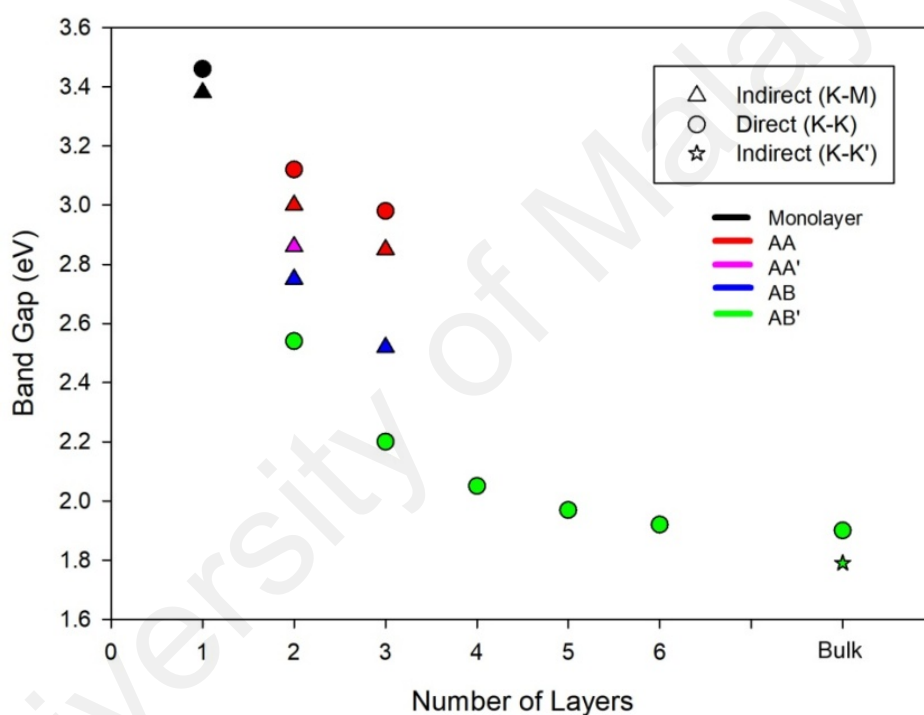


Figure 4.10: Reduction of band gap energy in different arrangements of g-SiC with the increasing number of layers due to quantum confinement

Figure 4.10 summarizes the band gap of various g-SiC arrangements, including the metastable AA' which interestingly shows equal band gap (2.86 eV) in both bilayer and trilayer; this suggests that the buckled layer dominates the electronic properties. The overall trend is the reduction of band gap as the slab becomes thicker. This could be attributed to quantum confinement and has been observed in other 2D binary compounds such as transition metal sulfides. (Kuc et al, 2011) For those arrangements

that have nearly identical (approximately ± 0.1 eV) indirect and direct gap, both values are shown in the graph.

Our lack of success in realizing silagraphene is exacerbated by the fact that since the original report by Sun et al in 2002, there has not been any confirmed sighting of graphitic SiC. As mentioned in Chapter 2, what more recent studies have mistakenly labeled as SiC "nanotubes" or 2D SiC are in fact structures made entirely of tetrahedrally-coordinated SiC.

Until today, graphitic SiC has proven to be an elusive material, lingering at the boundary of mirage and reality. We described a new method in Chapter 3 for synthesis of endothermic compounds using impermeable plasma, a type of thermal plasma that is insulated by a blanket of high-pressure gas ($\Delta P_{\text{plasma-gas}} = -7500$ Torr). The plasma-gas interface acts as a diamagnetic barrier that repels the escaping ions back into the core, where they collide with other ions and induce viscous heating. The core region is an ideal environment for high-enthalpy growth of nanomaterials whose final structure would depend on the solid-state precursor, vicinity to the plasma core and the discharge itself (AC/DC, amperage, duration, carrier gas, etc).

In several experiments, we applied a pulsed DC discharge of argon at 300 A for 30 to 120 s onto a silicon-graphite pellet (1:1 molar ratio). The resulting structure in the core region was consistently a bed of SiC nanocrystals topped with a thin layer of graphitic features including fibrous, sheet-like and spherical morphologies (Fig. 5, a-c). In many cases, it appeared as if the nanowires were nucleated from the crystals and gradually turned into bundles of nanotubes. We initially dismissed these structures; mainly because it was challenging to isolate a sufficiently pure specimen from the pellet. Bulk characterizations such as XRD and Raman spectroscopy were dominated by common peaks from the underlying 3C and hexagonal SiC.

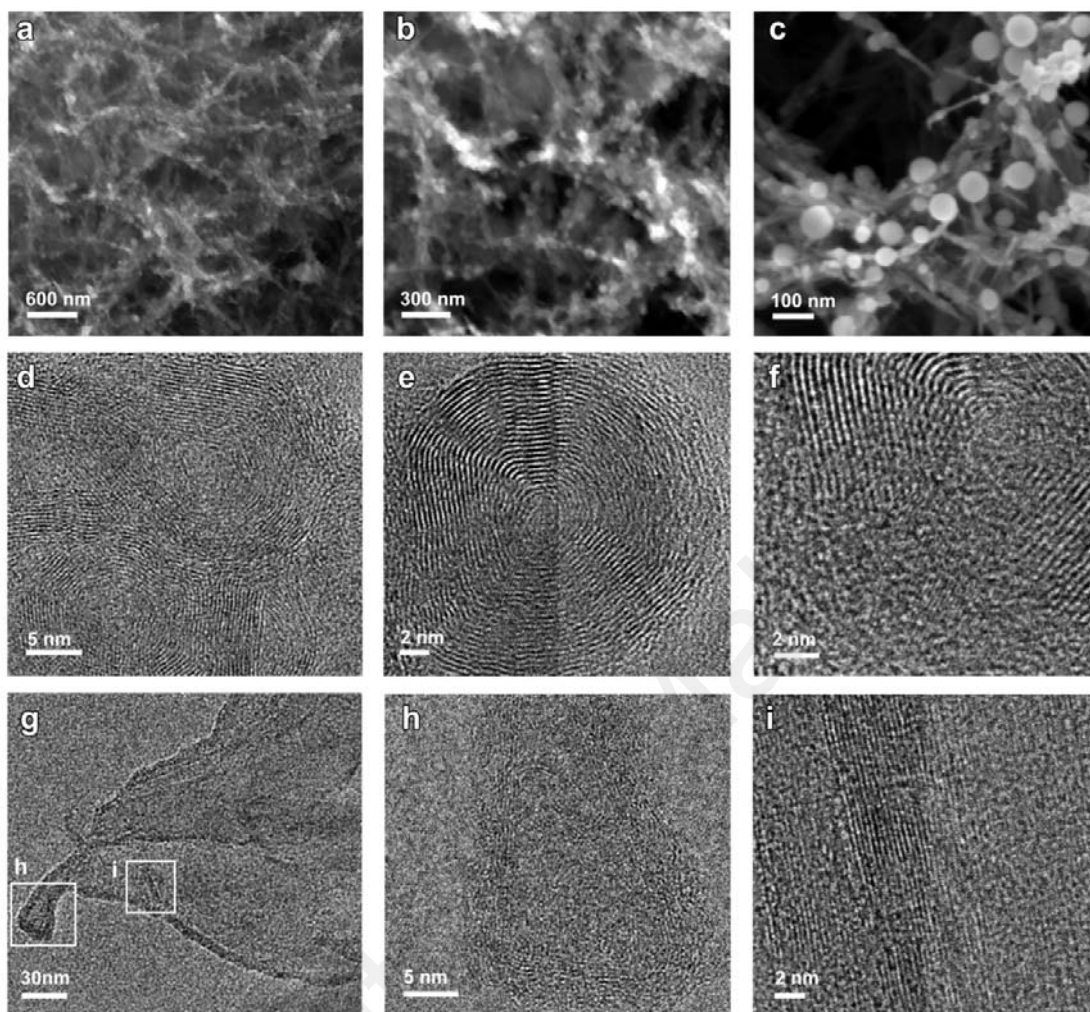


Figure 4.11: Field-emission scanning electron micrographs (FESEM) of graphitic features (sheet, tubes and onions) are depicted (a-c). (d) Several onions are resting on tubular structures. (e) A slightly puckered onion with a barely visible sp^3 -hybridized core (bottom left). (f) The same onion as (e) after several minutes of exposure to electron beams. The diamond-like core has grown larger, tearing open the onion in the bottom left side in the process. (g) Several-layer thick sheet of silagraphene. The magnified region (h) shows how the sheet curls into a tubular/onion-like feature while (i) is a closer view of one of the edges, exhibiting the characteristic interlayer distance of 3.7 Å

However upon closer examination using HRTEM, we found bundles of nanotubes, onion-like features as well as sheets (Fig4.11, d-I, see also Figure 4.12 for more) that showed significantly larger interlayer spacing as compared to graphene. Figure 4.13 demonstrates a detailed profiling of one of these onions. We found a spacing of 3.7 Å to be more common than the usual 3.3 Å spacing of graphene, followed by 4.2 Å and 4.7

Å. These numbers were recorded over 100 data points and were found to deviate less than 0.01 Å, indicating that they truly represent a long-range order, rather than a localized defect.

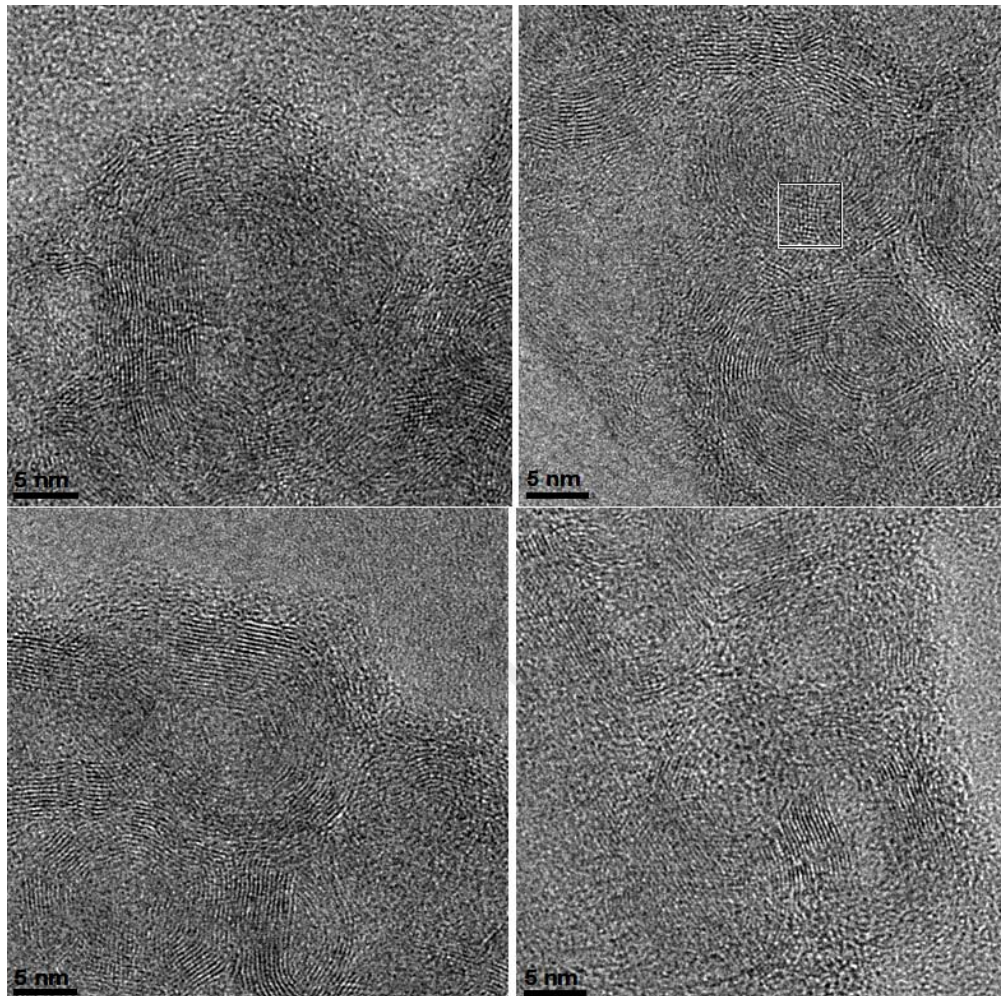


Figure 4.12: A series of HRTEM micrographs showing onion-like features that exhibit admixture of several interlayer spacing, but predominantly 3.7 Å. The outlined region shows superposition of two onions.

Our measurements fall within the same range as that of SiC nanotubes reported by Sun et al (2002). They are also perfectly compatible with our DFT calculations, a summary of which appears in Fig. 4.1.

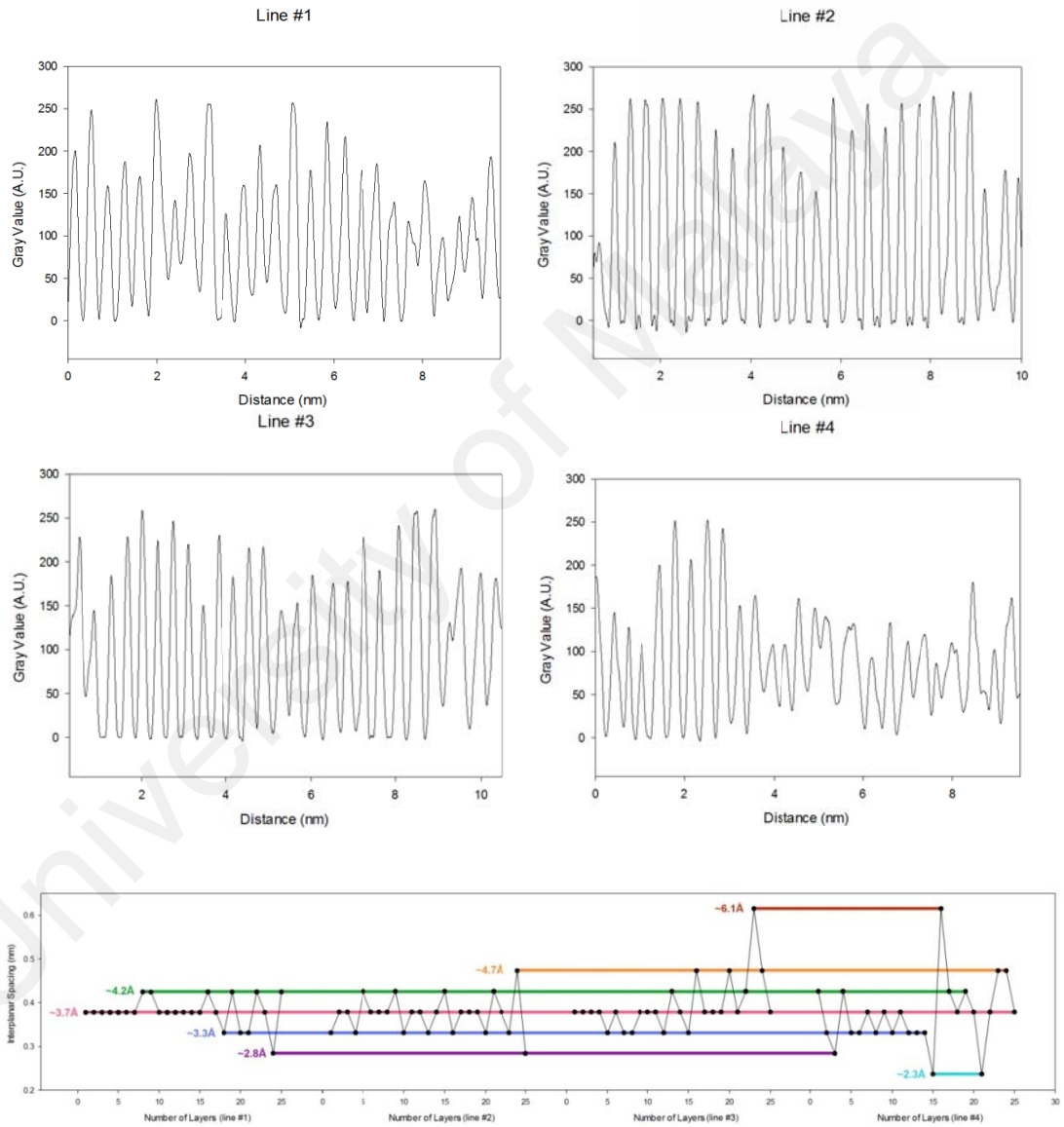
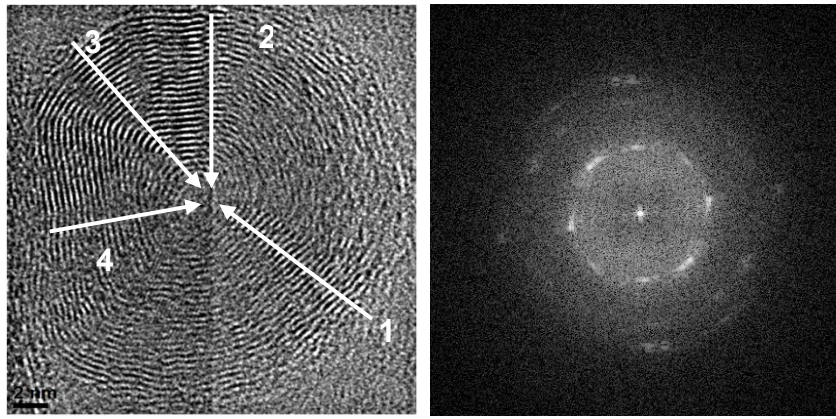


Figure 4.13: Line profiles taken from a slightly puckered onion along with its selected area electron diffraction (SAED) pattern. The scatter plot at the end summarizes the repeating measurements of interlayer spacing.

The fact that 3.7 Å is more common is in agreement with our earlier conclusions with regard to bulk stability of AB' stacking ($d=3.656$ Å). We also did not record more than two subsequent spacing of 4.2 Å and 4.7 Å which represent AB ($d=4.206$ Å) and AA ($d=4.641$ Å) stacking, respectively. This is also consistent with our phonon DOS calculations which suggest that these arrangements are likely to be unstable above three layers. Furthermore, we also observed a spacing of 2.3 Å in heavily puckered parts of the onion which could be attributed to AA' stacking ($d_{\text{avg}}=2.397$ Å). Sheet-like features (such as those shown in Figure 4.11g) were a few-layer thick and exclusively showed a spacing of 3.7 Å. Tubular features were also seen to curl into onion-like features (Figure 4.11, d and h) which could grow to be anywhere between a few tens to a few hundreds of nanometer in diameter. Some of these onions were found to have sp^3 -like core ($d=2.2$ Å) within them that over time would grow and eventually tear open the onion from within (Figure 4.11, e and f, and Figure 4.14).

This behavior is quite similar to what has been previously observed (Banhart & Ajayan, 1996) in carbon onions, concentric layered structures that effectively act as nanoscopic pressure cells and compress their own core to form diamond. This diamond core subsequently grows larger and larger under electron irradiation. Sun et al (2002) have also reported that after exposure to high-energy electron beams (200 kV at 100-150 μA) for several minutes, SiC nanotubes started to curl and self-compress into what was identified as 3C-SiC with $d_{[111]}=2.5$ Å. Interestingly, we found the sp^3 core to nucleate and grow in the heavily puckered region of the onion where AA' stacking were found. Our DFT calculations suggested earlier that this stacking is metastable and relaxes into a previously unknown rhombohedral polytype of SiC with $d_{[009]}=2.5$ Å and $d_{[10\bar{5}]}=2.2$ Å, which explains the difference between our measured d-spacing and that of Sun et al (2002).

HRTEM is an indispensable tool for the study of these structures, but we also applied a secondary technique to verify our findings. In the case of SiC nanotubes, a pair of absorption peaks at 101.2 eV and 282.5 eV was observed (Sun et al, 2002), which are higher and lower than a typical Si-C signal in Si L1 and C K1 edges, respectively.

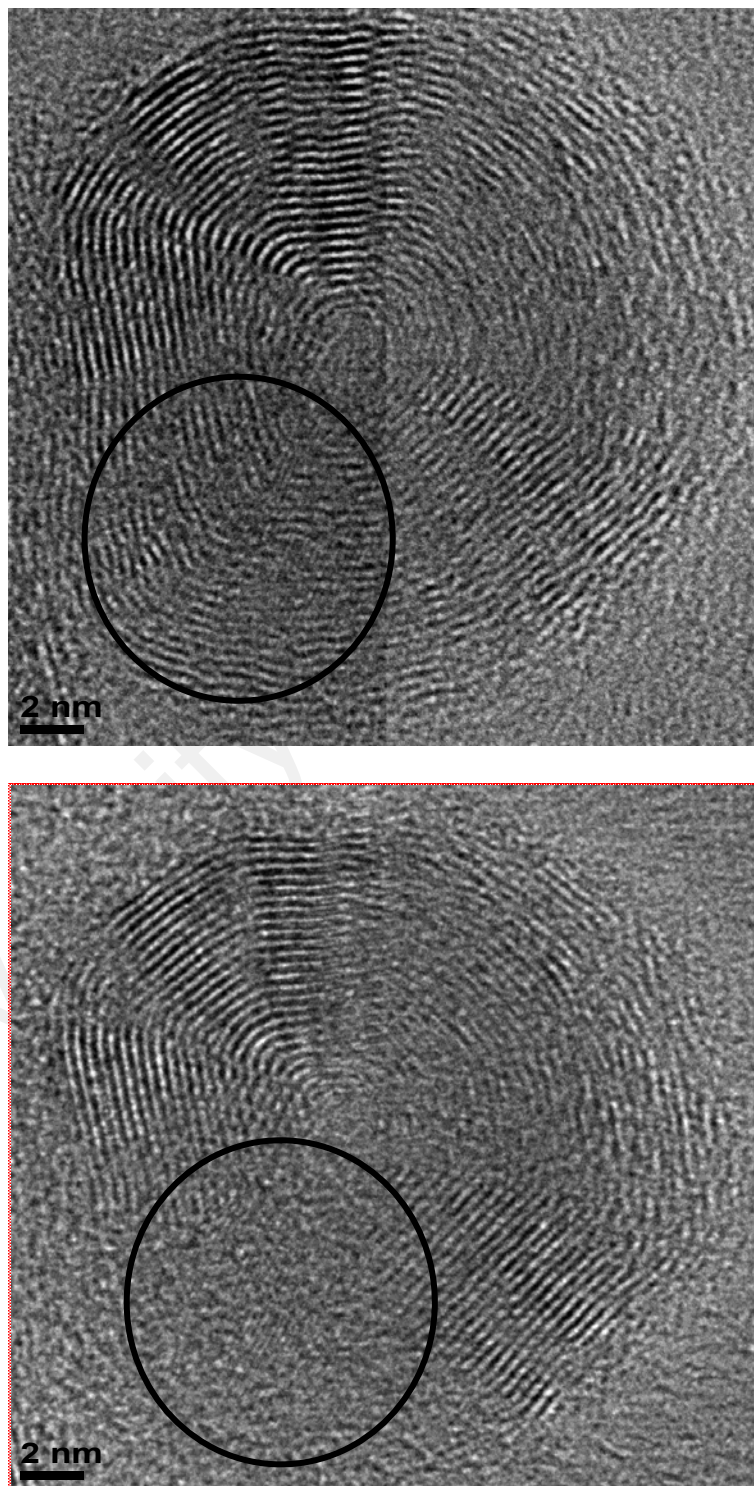


Figure 4.14: A pair of HRTEM micrographs showing an onion before (top) and after (bottom) the growing diamond-like core tears it open from within.

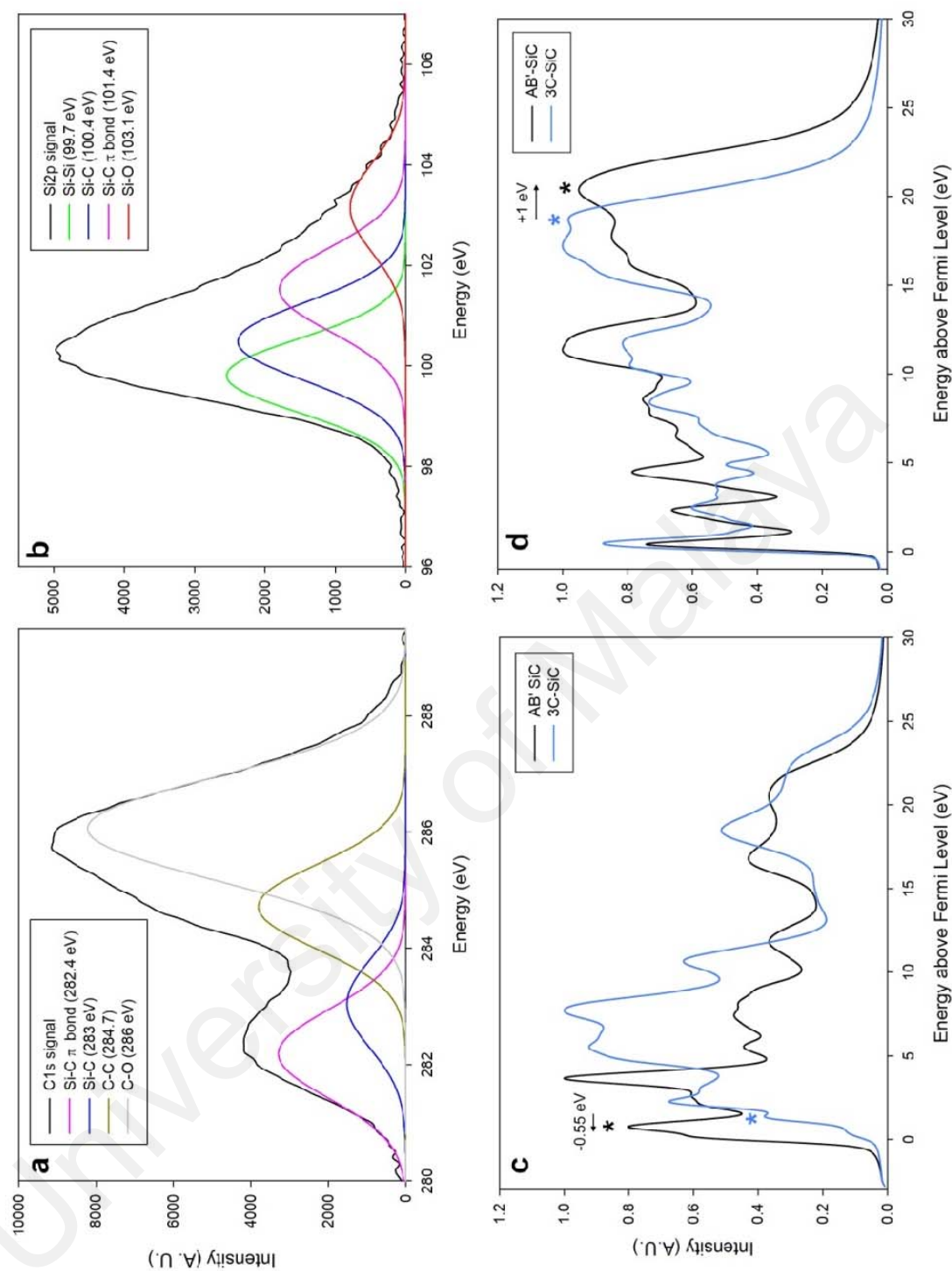


Figure 4.15: Experimental C1s (a) and Si2p (b) XPS signals from the sample along with the simulated core-level C (c) and Si (d) spectra of both AB' silagraphite and 3C-SiC for comparison. Observation of strong surface signals from oxide species is in line with the reactive nature of 2D materials.

In absence of atomically-resolved EELS, we analyzed the samples using the standard XPS instead. While soft X-ray excitation area is about 1 cm^2 , emitted photoelectrons are normally extracted from a much smaller region and a depth of only few nanometers.

Even then, if the results are still intermixed with other species, the high spectral resolution of binding energy and the low level of noise allows for deconvolution of peaks. Figure 4.15, a and b, show that the C1s core undergoes a clear shift, about 0.6 eV, to lower energies with a strong pre-edge peak centered around 282.4 eV. In contrast, in Si2p core, we see a 1 eV shift to higher energies, with a prominent peak at 101.4 eV. These measurements are very distinct from the usual 283 eV and 100.4 eV measured in the case of tetrahedral Si-C. (Shimoda et al, 2007)

To further validate this, we carried out core-level spectroscopy calculations based on the core-hole effect theory (Gao et al, 2008) for both 3C-SiC as well as the AB' silagraphite. The results as depicted in Fig. 4.15c and 6d indicate that in graphitic SiC, the pre-edge absorption peak shifts by 0.55 eV to lower energies and is much stronger, whereas in Si2p, the Si-C moves upward by 1 eV. Both of these values are in excellent agreement with our experimental results.

4.2 Origin of the Tetrahedral SiC Core in Graphitic Onions

In section 4.1, we came across graphitic features (sheets, tubes and onions) that were found to be different variations of silagraphene. In many of the onion-like features, certain portions were heavily puckered and had a significantly smaller interlayer spacing ($\sim 0.23 \text{ nm}$). Within these regions, we also observed a sp^3 -hybridized core with d-spacing of 0.21 to 0.22 nm, which one could attribute to [002] in 3C-SiC. However, our earlier DFT calculations showed that AA' stacking in silagraphene, which is interestingly obtained by breaking the bonds between layers of 2H-SiC in (001)

direction, is metastable and forms a buckled layered with an average interlayer spacing of ~ 0.23 nm.

Further analysis showed that if we allow a very miniscule stacking fault, about 1 degree (see Figure 4.16), these layers would collapse into a far more stable trigonal system (C_{3v}^5 -R3m space group) with a stacking sequence of ABA,BCB,CAC. The lattice constants for this optimal crystal of 9R-SiC were found to be $a=3.037$ Å and $c=22.603$ Å. This stacking happens to be identical to that of the hetero-layers reported by Kaiser et al (2001) within 2H-SiC whiskers.

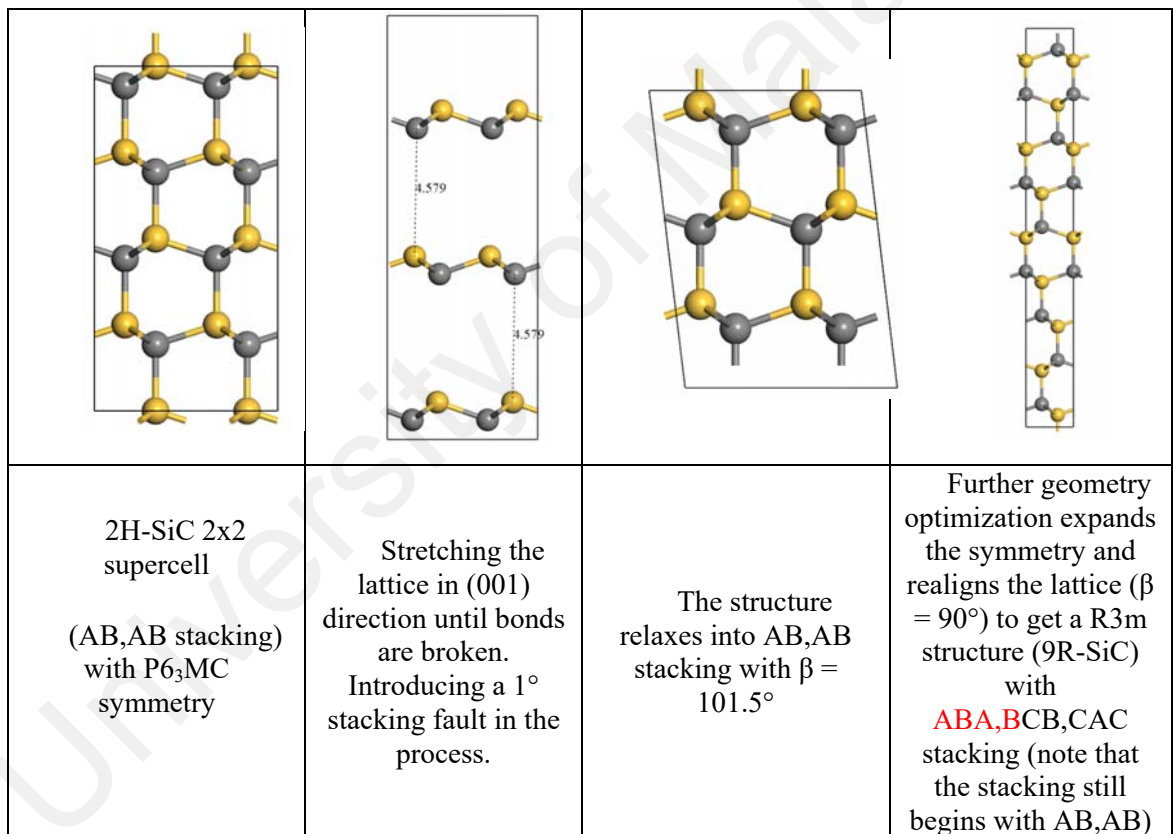


Figure 4.16: 2H \rightarrow 9R transformation in DFT calculations (left to right)

In the rhombohedral category, 15R-SiC is the simplest polytype (ABC,ACB,CAB,ACA,BCB) that has been verified beyond doubt. Theoretically speaking, a more primitive 9R polytype should also exist, (Limpijumnong & Lambrecht

1998) although its occurrence has been a subject of debate and its true atomic arrangement remains unresolved. Addressing these grey areas is important due to a number of factors. Firstly, both diamond (Lifshitz et al, 2001) and silicon (Lopez et al, 2011) as closely-related materials with similar bonding behavior have been shown to have stable 9R polytypes. Secondly, 9R phase plays a critical role in intermediate phase transformation of other complex material systems, such as Cu-Zn-Al shape memory alloys (Ahlers, 1986) and that might be the case with SiC too. Finally, 9R-SiC would have a hexagonality of 66.6% which is higher than that of 4H-SiC (50% hexagonality) and only second to that of 2H-SiC (100% hexagonality). Electronic band gap in SiC systems has been shown to widen with hexagonality, albeit not linearly (Käckell, 1994); therefore from a practical standpoint, electronic properties of 9R-SiC are also of interest, especially considering that it should be more stable than 2H-SiC. (Bernstein, 2005)

The very first sighting of what was presumably 9R-SiC was reported by Jepps and colleagues in 1979. They used tilted-beam imaging with 0.25 nm fringes, corresponding to the spacing of fundamental tetrahedral coordination polyhedra in SiC, to identify a previously unknown stacking. The specimen was prepared from a partially transformed 3C-SiC sample. Several regions around the $(11\bar{2})$ interface revealed a fine structure with repeating (111) threefold layers which suggested ABC,BCA,CAB stacking. This was identified as the elusive 9R-SiC, but the authors also noted that this nine-layer sequence could also originate from Moiré patterns between overlapping initial and twinned 3C-SiC. Subsequent attempts (Jepps & Page, 1980) to further resolve this structure was unsuccessful because the reflections were in extreme proximity of those of 3C-SiC.

In 1999, after almost two decades, Kaiser *et al* reported a similar structure with threefold periodicity and a spacing of 0.75 nm in several regions of an epitaxially grown 3C-SiC. Comparing the dark-field imaging data with simulations revealed two major discrepancies; firstly, the observed stacking sequence was incompatible with the model and secondly, the experimental FFT (fast Fourier transform) pattern showed a fully rectangular grid, rather than a slightly slanted one which is characteristic of rhombohedral systems. As a result, it was concluded that the structure was unambiguously an overlapping twinned 3C-SiC.

Soon after, Kaiser *et al* (2001) published another study in which they demonstrated that a 9R stacking, described in Hägg notations as [++-++-+-], does really occur in catalytically synthesized 2H-SiC whiskers; however only one 9R unit cell appeared in between multiple (6 to 12) repetitions of the 2H polytype. Whether this should be counted as a stable 9R phase remained an open question because an isolated occurrence like this could be simply described in terms of a local disorder.

Earlier in this chapter, we have determined the stable configurations of few-layer silagraphene, a two-dimensional form of SiC, by correlating experimental data with state-of-the-art density functional theory (DFT) models. A certain stacking order was found to be metastable and relax into a tetrahedral formation at lower energies. Here, we report that this tetrahedral structure has a striking resemblance to what DFT calculations identify as the true arrangement of bulk 9R-SiC.

Sun *et al* (2002) have also reported that after exposing SiC nanotubes to high-energy electron beams (200 kV at 100-150 μ A) for several minutes, they began to collapse and form what was determined to be 3C-SiC with $d_{[111]} = 0.25$ nm; although it has to be emphasized that this particular spacing is universal across all SiC polytypes and for example in the case of 9R-SiC could be attributed to [009]. In fact, one can see from

Figure 4.17 that the structure can be easily mistaken at first glance for 3C-SiC or any other common polytype of SiC. So what Sun et al (2002) have observed may have been 9R-SiC as well. Figure 4.17b also shows the atomic arrangement along [009].

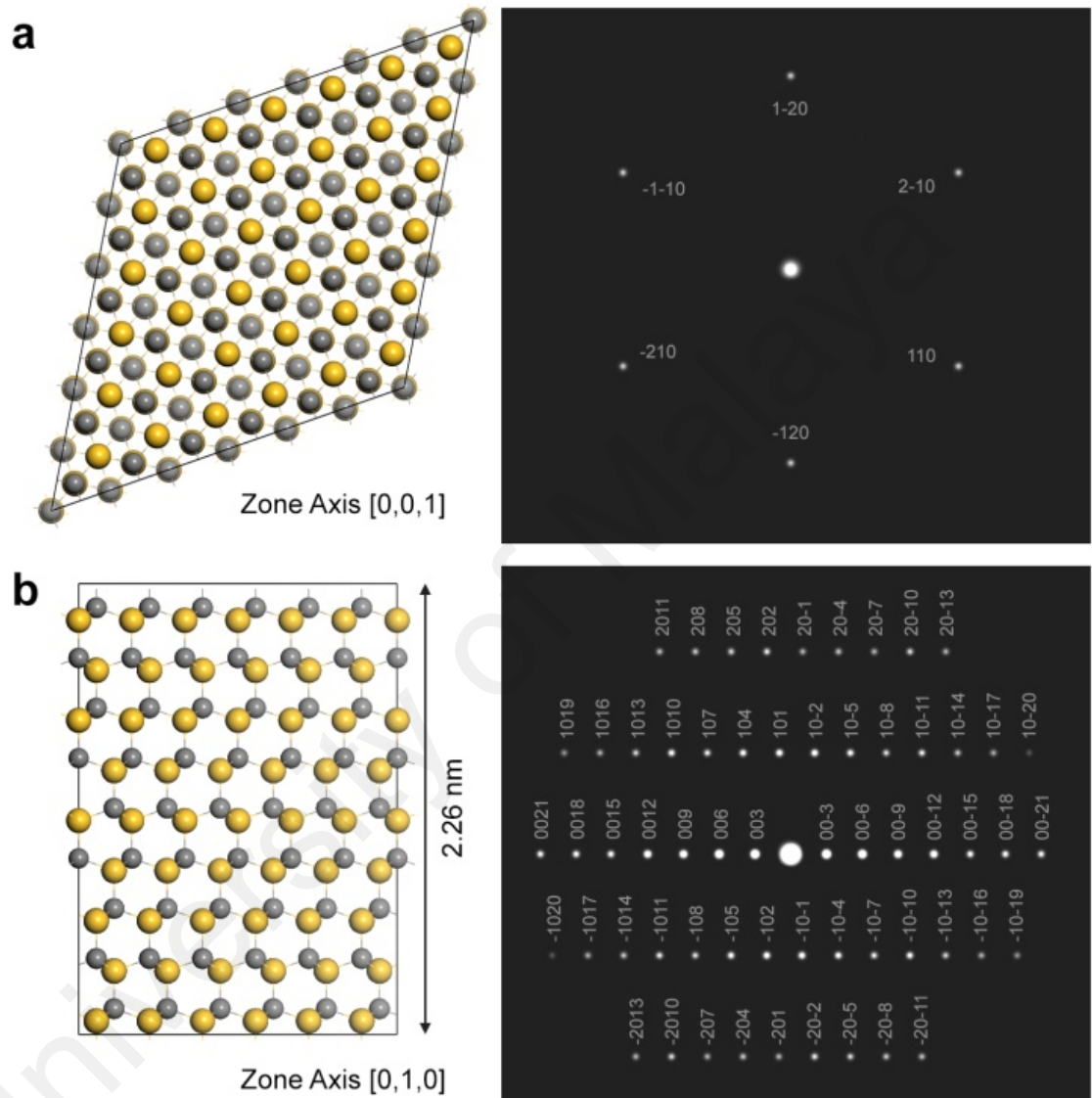


Figure 4.17: The atomic arrangement of 9R-SiC along c- (top) and b- (bottom) axis. Simulated electron diffraction patterns and the corresponding Miller indices are also shown.

A list of peaks along with their calculated intensities and Miller indices appear in Table 4.1. Generally speaking, it would be challenging to differentiate between 9R-SiC and other common rhombohedral polytypes such as 15R-SiC from XRD alone. In

particular, the set of major peaks between 30° and 40° are quite similar in all polytypes (see Figure 4.18 for a comparison with calculated XRD of 15R-SiC). Certain minor peaks between 45° to 70° slightly shift by 1° to 2° in rhombohedral systems but perhaps the easiest way of distinguishing 15R-SiC is to look for a pair of minor peaks at 41.4°, representing [1010] and 42.9°, representing [10-11]. These peaks are absent in 9R-SiC and instead a small peak at 44° emerges that corresponds to [107].

Table 4.1: List of major XRD peaks in 9R-SiC along with their corresponding Miller indices and calculated intensities.

Miller Index			2θ (deg)	Intensity (%)	d-spacing (Å)
h	k	l			
0	0	3	11.7356	0.308	7.53
0	0	6	23.5967	0.601	3.76
1	0	1	33.8881	32.646	2.64
1	0	-2	34.5976	8.39	2.59
0	0	9	35.7211	100	2.51
1	0	4	37.3174	66.073	2.4
1	0	-5	39.2506	34.496	2.29
1	0	7	44.0575	2.811	2.05
1	0	-8	46.8584	9.385	1.93
0	0	12	48.276	0.946	1.88
1	0	10	53.1165	13.149	1.72
1	0	-11	56.5359	3.942	1.62
1	1	0	60.175	25.207	1.53
0	0	15	61.483	0.003	1.50
1	1	3	61.5462	0.001	1.50
1	0	13	63.9	42.739	1.45
1	1	6	65.5601	0.154	1.42
1	0	-14	67.8385	35.128	1.38
2	0	-1	70.884	1.051	1.32
2	0	2	71.306	0.151	1.32
1	1	9	71.9877	31.443	1.31
2	0	-4	72.9838	1.248	1.29
2	0	5	74.2323	0.727	1.27
0	0	18	75.672	0.595	1.25
1	0	16	76.2396	0.422	1.24
2	0	-7	77.5261	0.715	1.23
2	0	8	79.5629	4.001	1.20
1	1	12	80.6249	1.774	1.19
1	0	-17	80.7225	4.958	1.18
2	0	-10	84.4023	1.009	1.14
2	0	11	87.2047	2.99	1.11

More intense peaks on the other hand often coincide with major peaks in common polytypes such as 3C- and 6H-SiC, so it would not be possible to develop any conclusive argument if only these peaks are observed.

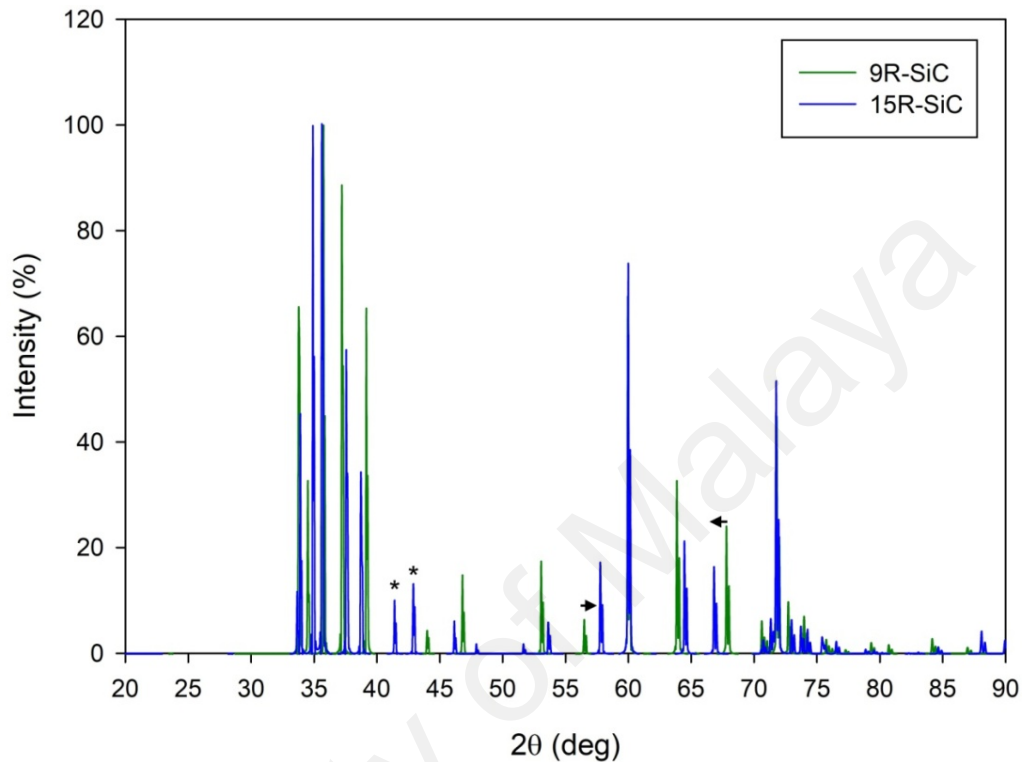


Figure 4.18: Simulated XRD profiles of 9R- and 15R-SiC. The asterisks indicate a pair of peaks that are unique to 15R-SiC and do not appear in 9R-SiC. The arrows show slight shift of certain peaks in 9R-SiC as compared to 15R-SiC.

The inset of Figure 4.19 further shows the simulated morphology of the crystal that was obtained using the Bravais-Friedel Donnay-Harker (BFDH) method. (Docherty et al, 1991) The overall morphology that one is expected to see in scanning electron microscopy is alike in both hexagonal and rhombohedral polytypes. The only exception is that in hexagonal polytypes, all side facets are fully rectangular whereas in rhombohedral SiC, one of the two side facets takes the form of an elongated hexagon (the arrow in inset of Figure 4.19).

The crystallographic system of 9R-SiC is not centro-symmetric and is therefore prone to developing stacking faults. This behavior, especially in non-equilibrium growth environments, could lead to the formation of native defects such as anti-sites. In our DFT calculations, silicon antisites were found to destabilize the 9R-SiC arrangement. In contrast, carbon antisites were stable but a higher carbon content generally made the structure less energetically favorable (e.g. a singular carbon antisite per lattice by 0.42 eV per atom and the carbon-rich 9R-SiC₅ by 2.2 eV per atom). Addition of carbon also heavily compresses the lattice due to the shorter length of C-C bonds (1.54 Å). 9R-SiC₅ for instance compressed the lattice in every direction by almost 10% and interestingly made the planes along the c-axis, such as [003] at 6.8 Å and [006] at 3.4 Å highly diffractive (see Fig. 4.20).

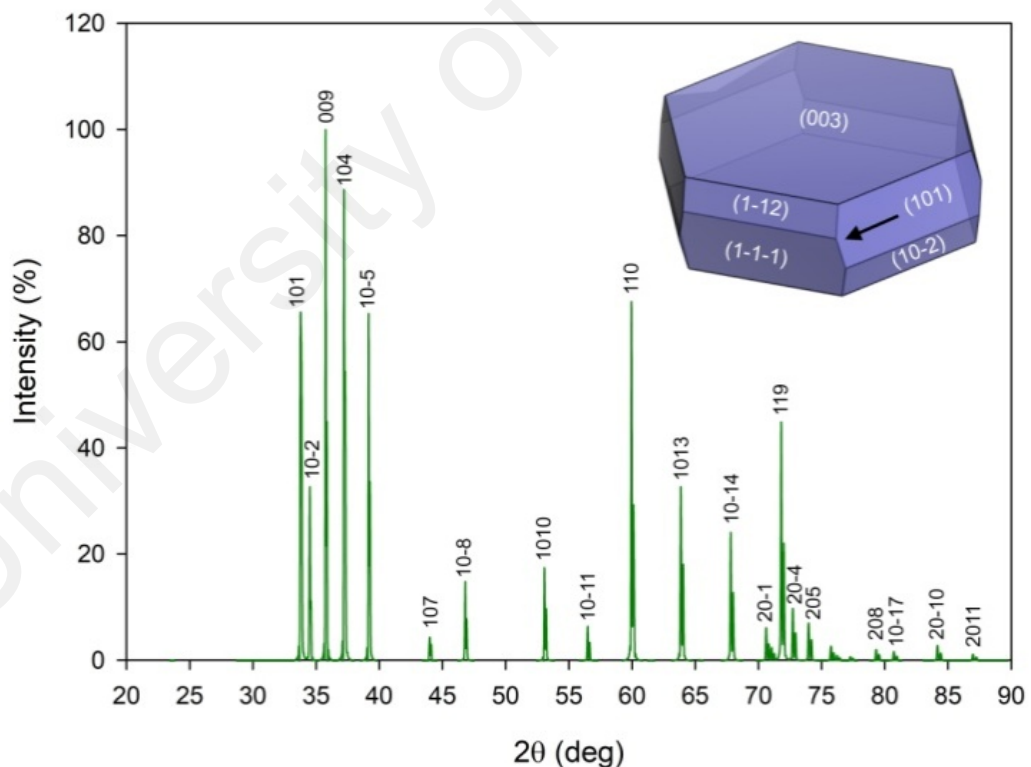


Figure 4.19: Simulated XRD profile of 9R-SiC. The inset shows the crystal morphology as computed using the BFDH method.

Owing to its simpler structure that gives rise to fewer phonon modes, 9R-SiC could be effectively identified against other rhombohedral polytypes using Raman scattering (see Figure 4.21). For instance in the case of 15R-SiC, there is a distinctive folded transverse acoustic (FTA) mode at 166 cm^{-1} which corresponds to phonon modes with $x=2/5$ symmetry. Here, $x=q/q_B$ is the reduced wave vector of the phonon modes in the basic Brillouin zone corresponding to the folded modes at the gamma (G) point. (Nakashima & Harima, 1997)

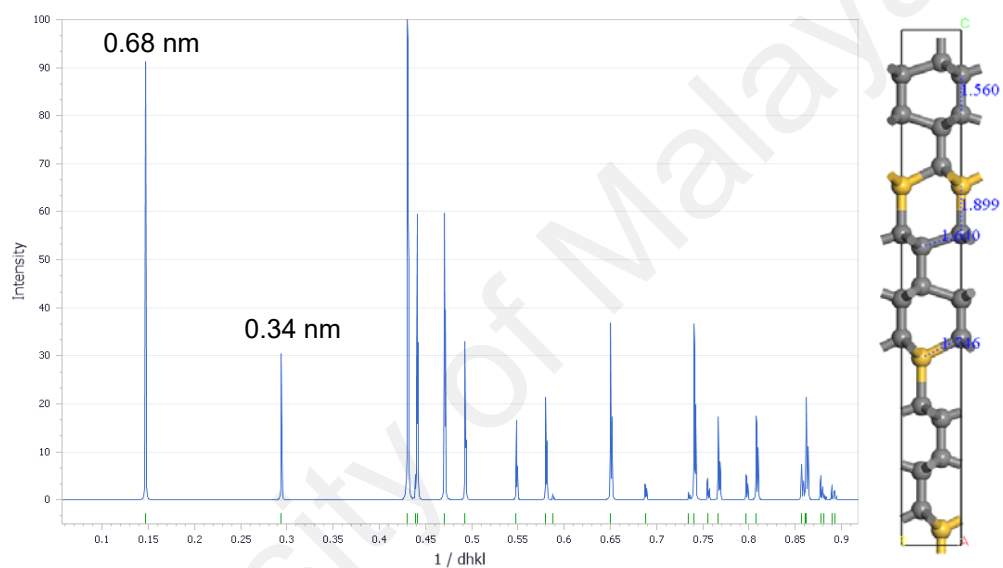


Figure 4.20: A carbon-rich variation of 9R-SiC with (C:Si ratio of 5:1) is shown. The lattice is compressed by 10% due to shorter C-C bonds ($a, b= 2.7\text{ \AA}$, $c= 20.42\text{ \AA}$) and the diffraction spots along the c-axis (003, 006 and so on) become significantly prominent.

On the contrary, $x=2/3$ modes in 9R-SiC have similar vibrational footprint to that of $x=4/5$ in 15R-SiC and as a result they do not make for reliable reference points. For example, the folded longitudinal optical (FLO) mode in 9R-SiC takes place at 857 cm^{-1} whereas that of $x=4/5$ in 15R-SiC occurs at a slightly lower frequency of 852 cm^{-1} . This frequency gap however is generally more pronounced in acoustic modes. For instance, the folded longitudinal acoustic (FLA) modes appear at 495 cm^{-1} and 563 cm^{-1} for 9R-SiC and 15R-SiC ($x=4/5$), respectively. Folded transverse optical (FTO) peaks are often

tens of times stronger in intensity than any other peak, so they are expected to dominate the experimental signals, but at the same time, they are far more complex. The Raman profiles of Figure 4.21 were calculated using extremely low smearing (5 cm^{-1}) to resolve individual peaks.

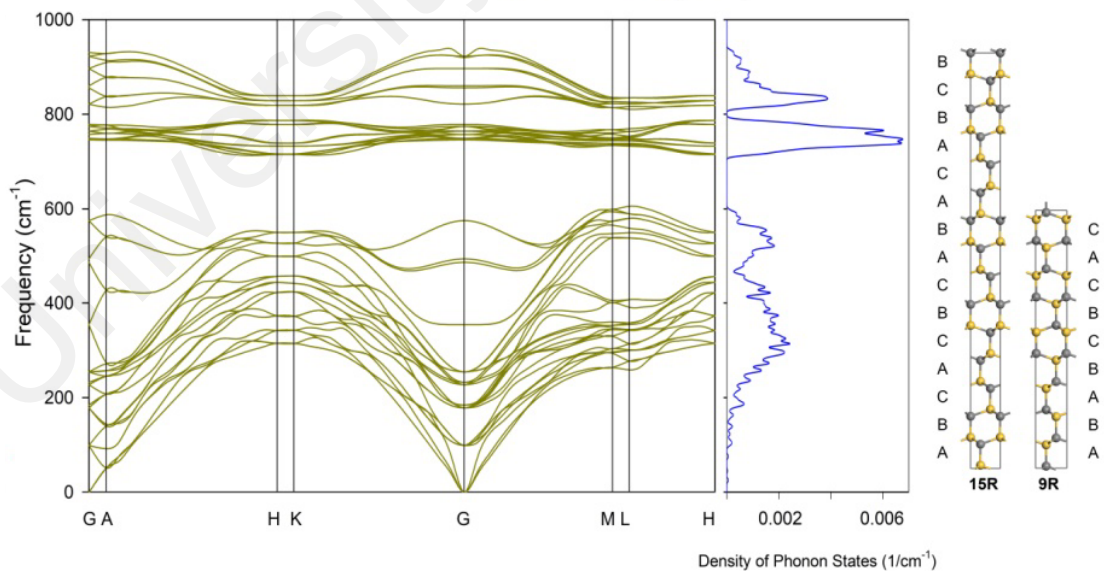
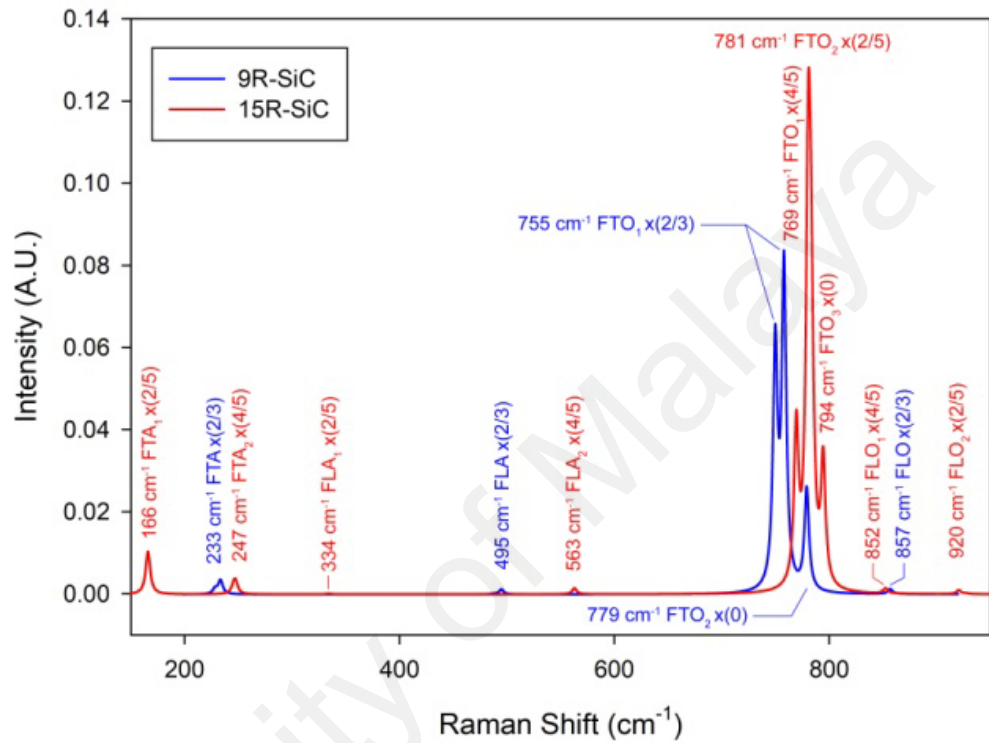


Figure 4.21: Calculated Raman spectra for 9R- and 15R-SiC along with the assigned vibrational modes (top). The stacking sequences of both polytypes are visualized for clarity (bottom, far right). Phonon dispersion curves and phonon DOS of 9R-SiC are also shown.

In the case of 9R-SiC, this has led to the formation of a pair of artificial peaks. Theoretically, we expect to see only one peak corresponding to $x=2/3$ and as a matter of fact, a higher Lorentzian smearing of 15 cm^{-1} reveals a singular peak centered around 755 cm^{-1} . In this particular interval, the second FTO mode of 9R-SiC ($x=0$) at 779 cm^{-1} almost coincides with the second FTO mode of 15R-SiC ($x=2/5$) at 781 cm^{-1} . We must also highlight a few practical challenges here. In a realistic scenario, it would be difficult to obtain highly resolved peaks such as these, unless the signals are recorded at sufficiently low temperatures or come from a large enough single crystal of high quality.

While assessing the Raman scattering, we also studied the phonon dispersion curves of our proposed 9R-SiC structure. It is apparent from Figure 4.21 that there is no imaginary acoustic modes (negative frequencies), indicating that the structure is dynamically stable in its native bulk form. The overall shape of curves is very similar to that of other SiC polytypes, but obviously there are fewer populated bands due to a simpler structure (phonon dispersion curves of 15R-SiC are given in Figure 4.22).

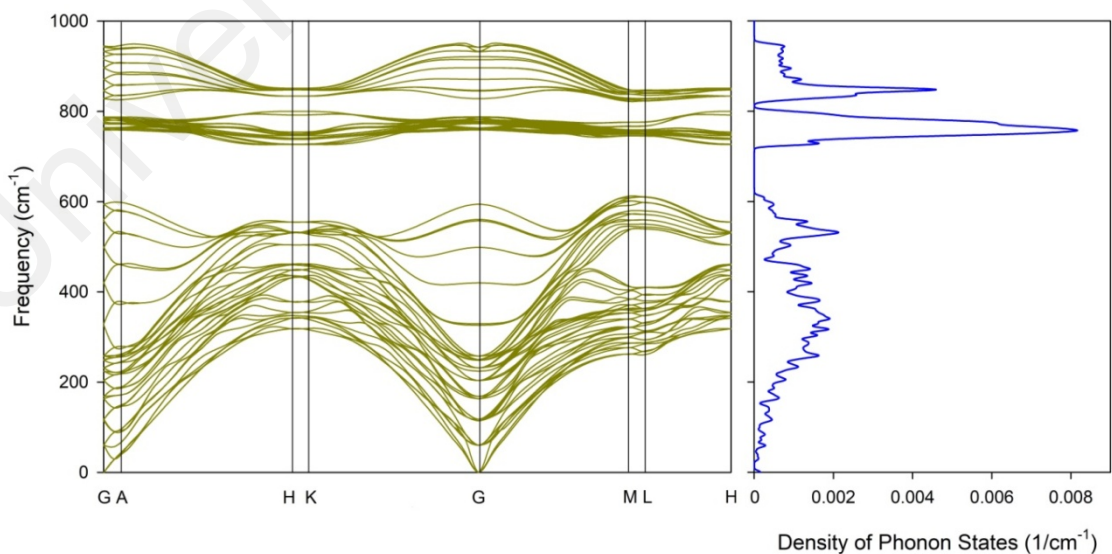


Figure 4.22: Phonon dispersion curves and phonon DOS of 15R-SiC are very similar to those of 9R-SiC.

To a small degree, LDA underestimates the frequency of optical phonons as compared to the Raman modes that are computed using GGA. TO bands (positioned between 750 cm^{-1} and 800 cm^{-1}) are relatively non-dispersive (more flat) and that explains why the Raman intensity for TO is so strong. In contrast, the phonon DOS implies that the LO mode should be significantly more prominent than what we see in our Raman calculations.

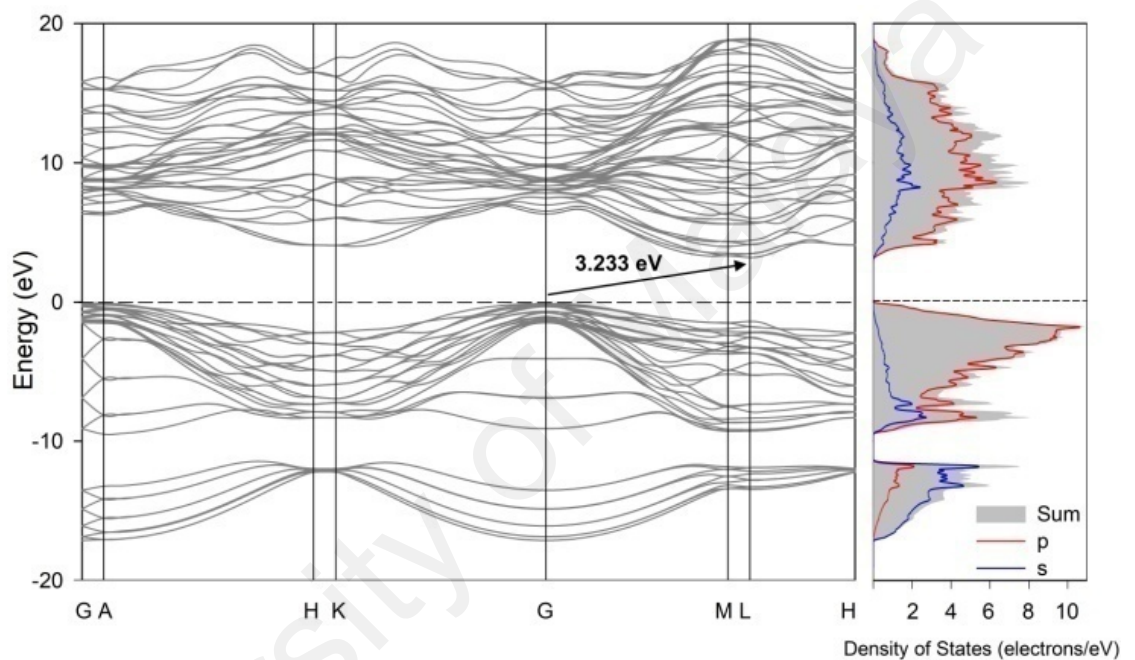


Figure 4.23: Electronic band structure and partial DOS of 9R-SiC.

To identify the root of this issue, we performed Raman calculations using various functionals (LDA, GGA and the hybrid HSE06) for 3C- and 6H-SiC. To rule out the effect of anharmonicity, simulations were repeated at different temperatures (10, 300 and 1000K) as well as excitation wavelengths (325, 514 and 785 nm). Regardless of such variables, CASTEP was found to grossly underestimate or even completely ignore the contribution of LO phonons to Raman activity for all of these structures.

Band structure and pDOS of 9R-SiC as calculated using the hybrid HSE06 functional are shown in Figure 4.23. As is the case with other SiC polytypes, the contribution of s-orbital to the band edge DOS is minimal. The features of the bands are also quite similar to those of 15R-SiC (shown in Figure 4.24), although there is one major difference.

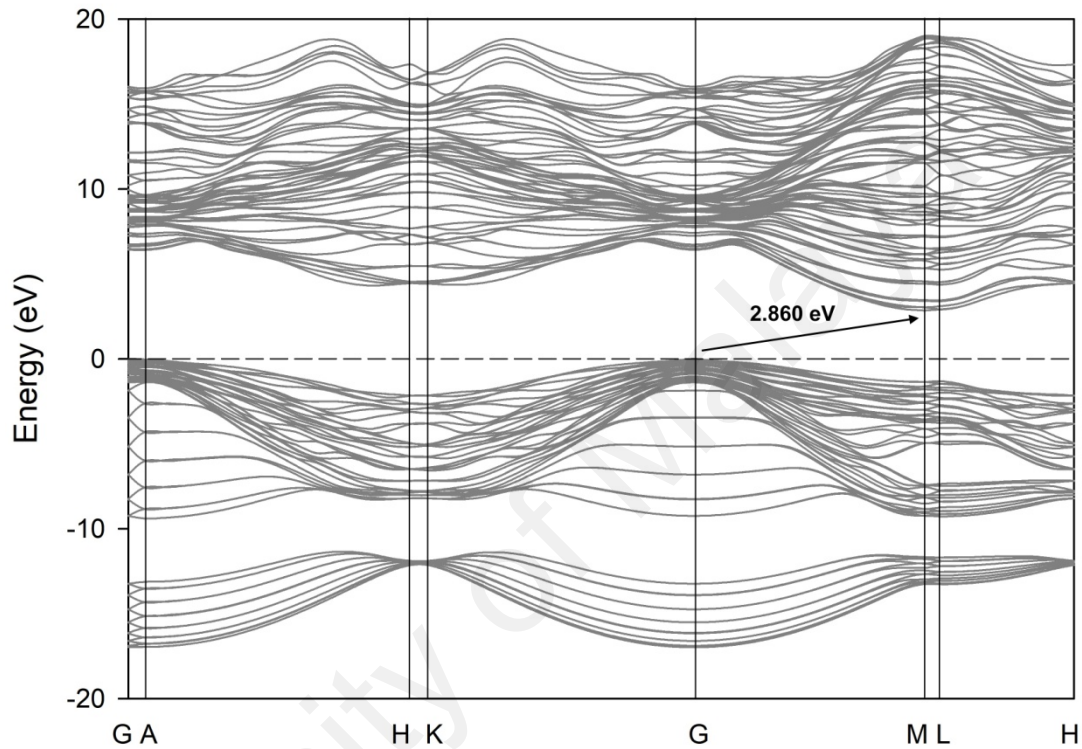


Figure 4.24: Electronic band structure of 15R-SiC is very similar to that of 9R-SiC, but the CBM takes places at the M-point (similar to most hexagonal polytypes of SiC).

In 9R-SiC, the CBM exhibit a sudden bump at the L point in the Brillouin zone. This appears to be unique to 9R-SiC, because 15R-SiC, similar to hexagonal polytypes (beside 2H-SiC) has its CBM at the M point. Similar calculations were carried out for other common SiC polytypes and the results appear in Table 4.2. Complete band structures of 2H- and 4H-SiC are provided in Figure 4.25 for reference. One can see that the calculated band gap for 9R-SiC is even higher than that of 2H-SiC despite its lower

hexagonality. Xue and colleagues (2005) have also reported that unlike other polytypes, the band gap in 9R diamond does not follow the same trend as hexagonality.

Table 4.2: A comparison between experimental (Ching et al, 2006) band gap energy and HSE06 functional calculations. *Note that the reported values for 3C-SiC vary between 2.2 eV and 2.39 eV in different works. Here, we have used an average value.

SiC Polytype	Hexagonality (%)	Indirect gap	HSE06 band gap (eV)	Experimental gap (eV)	Error (%)
3C	0	G → X	2.145	2.30*	- 7.226
2H	100	G → K	3.103	3.33	- 6.817
4H	50	G → M	3.131	3.27	- 4.25
6H	33.3	G → M	2.905	3.02	- 3.807
9R	66.6	G → L	3.233	–	–
15R	40	G → M	2.860	3.0	- 4.895

Given that HSE06 consistently underestimated the band gap in other SiC polytypes, we used quadratic interpolation of error percentages to estimate the experimental band gap of 9R-SiC. The resulting value (~ 3.4 eV) is clearly higher than that of 2H-SiC and is similar to that of GaN, suggesting that 9R-SiC would be a good candidate for high-frequency applications. Another remarkable feature is the relatively sharp tip of the CBM curve in 9R-SiC which indicates a smaller effective electron mass. 15R-SiC is already known to have a higher electron mobility than most SiC polytypes, (Schomer et al, 1999) and therefore 9R-SiC is expected to be even more attractive for device applications.

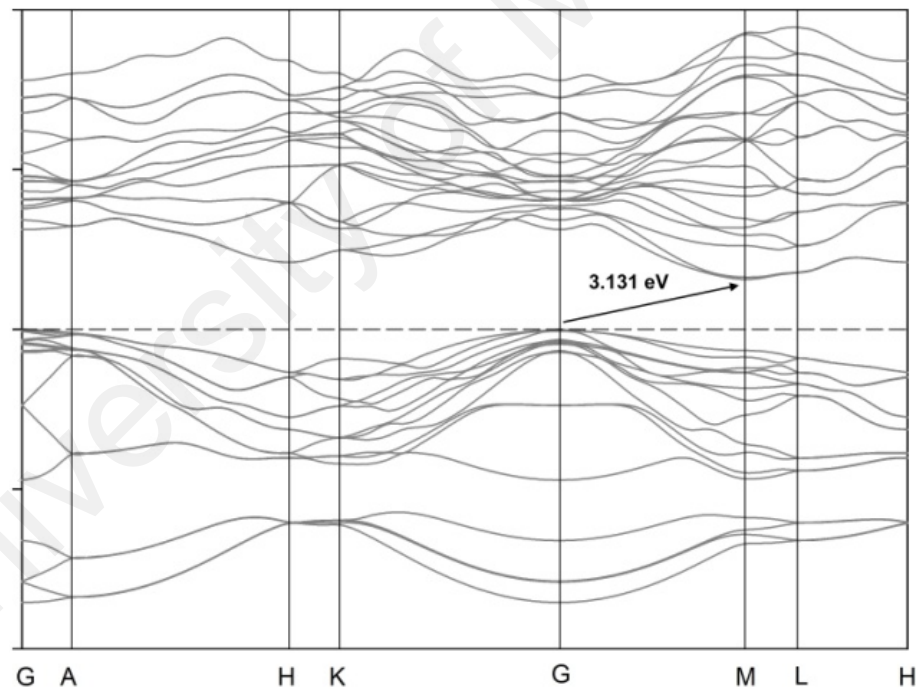
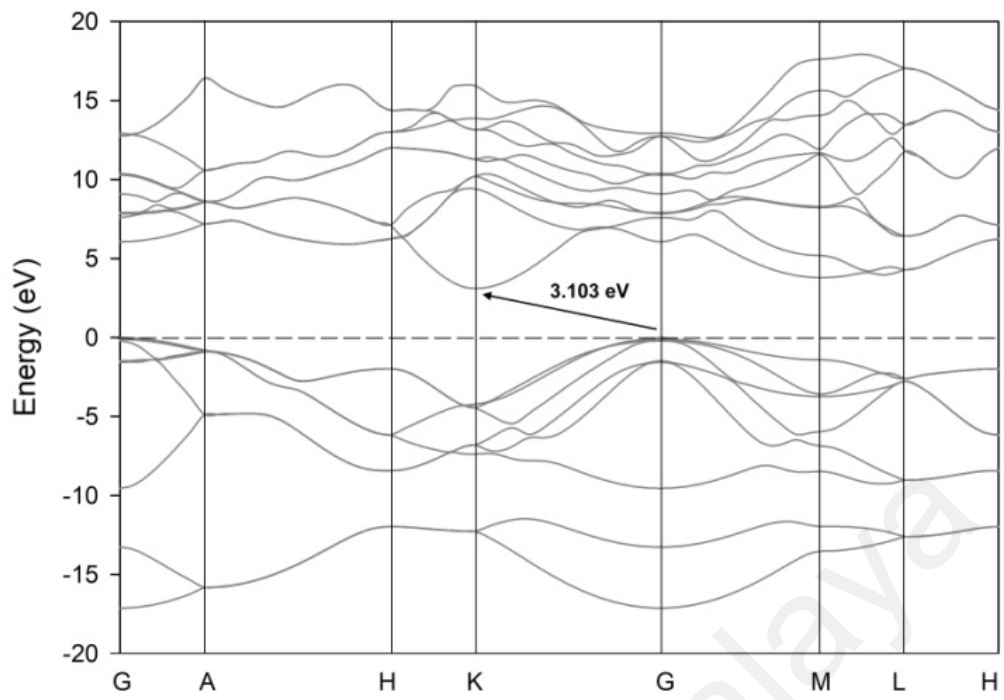


Figure 4.25: Electronic band structure of 2H- (top) and 4H-SiC (bottom) as computed using HSE06 functional are shown for comparison.

CHAPTER 5: CONCLUSIONS

A comprehensive computational was conducted study to explain the variations of interlayer spacing in g-SiC. Three stable polymorphs based on different stacking arrangements were identified, one of which is surprisingly stable as a bulk. Accurate electronic band structures of monolayer and few-layer silagraphene were determined using the HSE06 hybrid functional. In terms of technological applications, polymorphs of silagraphene have very diverse optical properties, covering the whole visible light spectrum and ranging from UV to almost NIR (360-690 nm). In addition to being suitable for photovoltaic devices and light-emitting diodes, silagraphene's unusual band structure makes it a viable candidate for applications involving strain engineering such as highly sensitive sensors. While Silagraphene is unlikely to have as high carrier mobility as some other 2D materials, its anisotropic transport properties are fascinating and are being studied in more details. A number of 2D semiconductors (e.g. TMDs) also show indirect-direct gap transition (Manzeli et al, 2017), but what makes silagraphene unique is its unusual band structure which exhibits nearly non-dispersive features. This attribute is perhaps exclusive only to 2D polymorphs of IV-IV semiconductors, such as the theoretically predicted GeC and SnC monolayers, (Lü et al, 2012) and silagraphene is the first compound in this group to become a reality.

In the second half of Chapter 4, it was shown that 9R-SiC is stable not only as a intermediary disorder, but as a bulk phase with a stacking sequence of ABA,BCB,CAC. This polytype is seemingly rare since it could be easily mistaken for the commonly occurring 3C-SiC in crystallographic and microscopic characterizations. In contrast, vibrational footprints of 9R-SiC are distinctive and could be used to reliably identify the material. Electronic properties of this polytype are quite exceptional. Firstly, 9R-SiC exhibits the widest band gap of all SiC polytypes and secondly, its CBM uniquely takes

place at L point where the shape of the band suggests an unusually low effective mass. As a result, 9R-SiC could be the ideal candidate for high-frequency MOSFETs.

5.1 Future Studies

Energy requirements of silagraphene are relatively high and we did not manage to isolate pure and high-quality samples in large quantities for further investigations. Future studies should focus on alternative routes of preparation, such as heavy doping of ultrathin silicon or graphene.

Similarly, the optimal conditions of growth for large-scale and high-quality 9R-SiC samples are not clear yet and require detailed molecular dynamic simulations. Theoretically, when bonds in the [001] direction of 2H-SiC are broken in tension, even a small degree of stacking fault could lead to the formation of 9R-SiC. Further work in this area could also enable the controlled growth of 2H/9R type II heterojunctions.

REFERENCES

- Aarons, J., Sarwar, M., Thompsett, D., & Skylaris, C. K. (2016). Perspective: Methods for large-scale density functional calculations on metallic systems. *The Journal of chemical physics*, *145*(22), 220901.
- Aoki, M., & Amawashi, H. (2007). Dependence of band structures on stacking and field in layered graphene. *Solid State Communications*, *142*(3), 123-127.
- Ahlers, M. (1986). Martensite and equilibrium phases in Cu-Zn and Cu-Zn-Al alloys. *Progress in materials science*, *30*(3), 135-186.
- Banhart, F., & Ajayan, P. M. (1996). Carbon onions as nanoscopic pressure cells for diamond formation. *Nature*, *382*(6590), 433.
- Bernstein, N., Gotsis, H. J., Papaconstantopoulos, D. A., & Mehl, M. J. (2005). Tight-binding calculations of the band structure and total energies of the various polytypes of silicon carbide. *Physical Review B*, *71*(7), 075203.
- Bertilsson, K., & Nilsson, H. E. (2002). Optimization of 2H, 4H and 6H-SiC high speed vertical MESFETs. *Diamond and related materials*, *11*(3), 1254-1257.
- Bhatnagar, M., & Baliga, B. J. (1993). Comparison of 6H-SiC, 3C-SiC, and Si for power devices. *IEEE Transactions on electron devices*, *40*(3), 645-655.
- Bootsma, G. A., Knippenberg, W. F., & Verspui, G. (1971). Phase transformations, habit changes and crystal growth in SiC. *Journal of Crystal Growth*, *8*(4), 341-353.
- Borowiak-Palen, E., Ruemmel, M. H., Gemming, T., Knupfer, M., Biedermann, K., Leonhardt, A., ... & Kalenczuk, R. J. (2005). Bulk synthesis of carbon-filled silicon carbide nanotubes with a narrow diameter distribution. *Journal of Applied Physics*, *97*, 056102.
- Bučko, T., Lebègue, S., Hafner, J., & Angyan, J. G. (2013). Tkatchenko-Scheffler van der Waals correction method with and without self-consistent screening applied to solids. *Physical Review B*, *87*(6), 064110.
- Chabi, S., Chang, H., Xia, Y., & Zhu, Y. (2016). From graphene to silicon carbide: ultrathin silicon carbide flakes. *Nanotechnology*, *27*(7), 075602.
- Chandrashekhar, M. V. S., Thomas, C. I., Lu, J., & Spencer, M. G. (2007). Observation of a two dimensional electron gas formed in a polarization doped C-face 3-C/4-H SiC heteropolytype junction. *Applied Physics Letters*, *91*(3), 033503.
- Charlier, J. C., Michenaud, J. P., & Gonze, X. (1992). First-principles study of the electronic properties of simple hexagonal graphite. *Physical Review B*, *46*(8), 4531.
- Ching, W. Y., Xu, Y. N., Rulis, P., & Ouyang, L. (2006). The electronic structure and spectroscopic properties of 3C, 2H, 4H, 6H, 15R and 21R polymorphs of SiC. *Materials Science and Engineering: A*, *422*(1-2), 147-156.

Choyke, W. J., Devaty, R. P., & Sridhara, S. G. (1999). A survey of conduction and valence band edges in SiC. *Physica Scripta*, 1999(T79), 9.

Constantinescu, G., Kuc, A., & Heine, T. (2013). Stacking in bulk and bilayer hexagonal boron nitride. *Physical review letters*, 111(3), 036104.

Cordier, Y., Portail, M., Chenot, S., Tottereau, O., Zielinski, M., & Chassagne, T. (2008). AlGa_N/Ga_N high electron mobility transistors grown on 3C-SiC/Si (111). *Journal of Crystal Growth*, 310(20), 4417-4423.

Ding, Y., & Wang, Y. (2014). Geometric and electronic structures of two-dimensional SiC₃ compound. *The Journal of Physical Chemistry C*, 118(8), 4509-4515.

Docherty, R., Clydesdale, G., Roberts, K. J., & Bennema, P. (1991). Application of Bravais-Friedel-Donnay-Harker, attachment energy and Ising models to predicting and understanding the morphology of molecular crystals. *Journal of Physics D: Applied Physics*, 24(2), 89.

Edmond, J. A., Kong, H. S., & Carter, C. H. (1993). Blue LEDs, UV photodiodes and high-temperature rectifiers in 6H-SiC. *Physica B: Condensed Matter*, 185(1), 453-460.

Eibl, O. (1993). New method for absorption correction in high-accuracy, quantitative EDX microanalysis in the TEM including low-energy X-ray lines. *Ultramicroscopy*, 50(2), 179-188.

Fawcett, T. J., Wolan, J. T., Myers, R. L., Walker, J., & Sadow, S. E. (2004). Wide-range (0.33%–100%) 3C-SiC resistive hydrogen gas sensor development. *Applied Physics Letters*, 85(3), 416-418.

Feng, B., Zhang, J., Zhong, Q., Li, W., Li, S., Li, H., ... & Wu, K. (2016). Experimental realization of two-dimensional boron sheets. *Nature chemistry*, 8(6), 563-568.

Fissel, A., Kaiser, U., Schröter, B., Richter, W., & Bechstedt, F. (2001). MBE growth and properties of SiC multi-quantum well structures. *Applied surface science*, 184(1), 37-42.

Fissel, A., Schröter, B., & Richter, W. (1995). Low-temperature growth of SiC thin films on Si and 6H-SiC by solid-source molecular beam epitaxy. *Applied Physics Letters*, 66(23), 3182-3184.

Forbeaux, I., Themlin, J. M., Charrier, A., Thibaudau, F., & Debever, J. M. (2000). Solid-state graphitization mechanisms of silicon carbide 6H-SiC polar faces. *Applied surface science*, 162, 406-412.

Freeman, C. L., Claeysens, F., Allan, N. L., & Harding, J. H. (2006). Graphitic nanofilms as precursors to wurtzite films: theory. *Physical review letters*, 96(6), 066102.

Gao, G. B., Sterner, J., & Morkoc, H. (1994). High frequency performance of SiC heterojunction bipolar transistors. *IEEE Transactions on Electron Devices*, 41(7), 1092-1097.

Gao, G., Ashcroft, N. W., & Hoffmann, R. (2013). The unusual and the expected in the Si/C phase diagram. *Journal of the American Chemical Society*, 135(31), 11651-11656.

Gao, M. R., Chan, M. K., & Sun, Y. (2015). Edge-terminated molybdenum disulfide with a 9.4-Å interlayer spacing for electrochemical hydrogen production. *Nature communications*, 6, 7493.

Gobre, V. V., & Tkatchenko, A. (2013). Scaling laws for van der Waals interactions in nanostructured materials. *Nature communications*, 4, 2341.

Heyd, J., Peralta, J. E., Scuseria, G. E., & Martin, R. L. (2005). Energy band gaps and lattice parameters evaluated with the Heyd-Scuseria-Ernzerhof screened hybrid functional. *The Journal of chemical physics*, 123(17), 174101.

Honjo, G., Miyake, S., & Tomita, T. (1950). Silicon carbide of 594 layers. *Acta Crystallographica*, 3(5), 396-397.

Hsueh, H. C., Guo, G. Y., & Louie, S. G. (2011). Excitonic effects in the optical properties of a SiC sheet and nanotubes. *Physical Review B*, 84(8), 085404.

Hu, J. Q., Bando, Y., Zhan, J. H., & Golberg, D. (2004). Fabrication of ZnS/SiC nanocables, SiC-shelled ZnS nanoribbons (and sheets), and SiC nanotubes (and tubes). *Applied physics letters*, 85(14), 2932-2934.

Huang, H., Chen, W., Chen, S., & Wee, A. T. S. (2008). Bottom-up growth of epitaxial graphene on 6H-SiC (0001). *Acs Nano*, 2(12), 2513-2518.

Huda, M. N., Yan, Y., & Al-Jassim, M. M. (2009). On the existence of Si-C double bonded graphene-like layers. *Chemical Physics Letters*, 479(4), 255-258.

Itoh, A., Akita, H., Kimoto, T., & Matsunami, H. (1994). High-quality 4H-SiC homoepitaxial layers grown by step-controlled epitaxy. *Applied physics letters*, 65(11), 1400-1402.

Jepps, N. W., Smith, D. J., & Page, T. F. (1979). The direct identification of stacking sequences in silicon carbide polytypes by high-resolution electron microscopy. *Acta Crystallographica Section A: Crystal Physics, Diffraction, Theoretical and General Crystallography*, 35(6), 916-923.

Jepps, N. W., & Page, T. F. (1980). 9R-HREM Observations of a New Silicon Carbide Polytype. *Journal of the American Ceramic Society*, 63(1-2), 102-103.

Käckell, P., Wenzien, B., & Bechstedt, F. (1994). Influence of atomic relaxations on the structural properties of SiC polytypes from ab initio calculations. *Physical Review B*, 50(23), 17037.

Kaiser, U., Chuvilin, A., Brown, P. D., & Richter, W. (1999). Origin of Threefold Periodicity in High-Resolution Transmission Electron Microscopy Images of Thin Film Cubic SiC. *Microscopy and Microanalysis*, 5(6), 420-427.

Kaiser, U., Chuvilin, A., Kyznetsov, V., & Butenko, Y. (2001). Evidence for 9R-SiC?. *Microscopy and Microanalysis*, 7(4), 368-369.

Kalna, K., Asenov, A., Ayubi-Moak, JS, Craven, AJ, Droopad, R., Hill, R., . . . Longo, P. (2008). *III-V MOSFETs for Digital Applications with Silicon Co-Integration*. Paper presented at the Advanced Semiconductor Devices and Microsystems, 2008. ASDAM 2008. International Conference on.

Kaneda, S., Sakamoto, Y., Mihara, T., & Tanaka, T. (1987). MBE growth of 3C-SiC/6- SiC and the electric properties of its pn junction. *Journal of Crystal Growth*, 81(1-4), 536-542.

Karmann, S., Helbig, R., & Stein, R. A. (1989). Piezoelectric properties and elastic constants of 4H and 6H SiC at temperatures 4–320 K. *Journal of Applied Physics*, 66(8), 3922-3924.

Komiyama, J., Abe, Y., Suzuki, S., & Nakanishi, H. (2006). Suppression of crack generation in GaN epitaxy on Si using cubic SiC as intermediate layers. *Applied physics letters*, 88(9), 091901.

Kondo, Y., Takahashi, T., Ishii, K., Hayashi, Y., Sakuma, E., Misawa, S., ... & Yoshida, S. (1986). Experimental 3C-SiC MOSFET. *IEEE electron device letters*, 7(7), 404-406.

Krukau, A. V., Vydrov, O. A., Izmaylov, A. F., & Scuseria, G. E. (2006). Influence of the exchange screening parameter on the performance of screened hybrid functionals. *The Journal of chemical physics*, 125(22), 224106.

Kuc, A., Zibouche, N., & Heine, T. (2011). Influence of quantum confinement on the electronic structure of the transition metal sulfide T S 2. *Physical Review B*, 83(24), 245213.

Kumar, A., Csáthy, GA, Manfra, MJ, Pfeiffer, LN, & West, KW. (2010). Nonconventional Odd-Denominator Fractional Quantum Hall States in the Second Landau Level. *Physical review letters*, 105(24), 246808.

Lebedev, A. A., Strel'chuk, A. M., Savkina, N. S., Bogdanova, E. V., Tregubova, A. S., Kuznetsov, A. N., & Davydov, D. V. (2003). Investigation of p-3C-SiC/n+-6H-SiC heterojunctions with low doped p-3C-SiC region. In *Materials Science Forum*(Vol. 433, pp. 427-430). Trans Tech Publications.

Li, J. B., Peng, G., Chen, S. R., Chen, Z. G., & Wu, J. G. (1990). Formation and Morphology of 2H-SiC Whiskers by the Decomposition of Silicon Nitride. *Journal of the American Ceramic Society*, 73(4), 919-922.

Li, Y., Li, F., Zhou, Z., & Chen, Z. (2010). SiC₂ silagraphene and its one-dimensional derivatives: where planar tetracoordinate silicon happens. *Journal of the American Chemical Society*, 133(4), 900-908.

Lifshitz, Y., Duan, X. F., Shang, N. G., Li, Q., Wan, L., Bello, I., & Lee, S. T. (2001). Nanostructure: Epitaxial diamond polytypes on silicon. *Nature*, 412(6845), 404.

Limpijumnong, S., & Lambrecht, W. R. (1998). Total energy differences between SiC polytypes revisited. *Physical Review B*, 57(19), 12017.

Lin, C. M., Chen, Y. Y., Felmetsger, V. V., Senesky, D. G., & Pisano, A. P. (2012). AlN/3C-SiC composite plate enabling high-frequency and high-Q micromechanical resonators. *Advanced Materials*, 24(20), 2722-2727.

Lin, S. S. (2012). Light-emitting two-dimensional ultrathin silicon carbide. *The Journal of Physical Chemistry C*, 116(6), 3951-3955.

Lin, S., Zhang, S., Li, X., Xu, W., Pi, X., Liu, X., ... & Chen, H. (2015). Quasi-two-dimensional SiC and SiC₂: interaction of silicon and carbon at atomic thin lattice plane. *The Journal of Physical Chemistry C*, 119(34), 19772-19779.

Lopez, F. J., Givan, U., Connell, J. G., & Lauhon, L. J. (2011). Silicon nanowire polytypes: identification by Raman spectroscopy, generation mechanism, and misfit strain in homostructures. *Acs Nano*, 5(11), 8958-8966.

Lu, J., Chandrashekar, M. V. S., Parks, J. J., Ralph, D. C., & Spencer, M. G. (2009). Quantum confinement and coherence in a two-dimensional electron gas in a carbon-face 3 C-SiC/6 H-SiC polytype heterostructure. *Applied Physics Letters*, 94(16), 162115.

Lü, T. Y., Liao, X. X., Wang, H. Q., & Zheng, J. C. (2012). Tuning the indirect-direct band gap transition of SiC, GeC and SnC monolayer in a graphene-like honeycomb structure by strain engineering: a quasiparticle GW study. *Journal of Materials Chemistry*, 22(19), 10062-10068.

Mannix, A. J., Zhou, X. F., Kiraly, B., Wood, J. D., Alducin, D., Myers, B. D., ... & Yacaman, M. J. (2015). Synthesis of borophenes: Anisotropic, two-dimensional boron polymorphs. *Science*, 350(6267), 1513-1516.

Manzeli, S., Ovchinnikov, D., Pasquier, D., Yazyev, O. V., & Kis, A. (2017). 2D transition metal dichalcogenides. *Nature Reviews Materials*, 2(8), 17033.

Melinon, P., Masenelli, B., Tournus, F., & Perez, A. (2007). Playing with carbon and silicon at the nanoscale. *Nature materials*, 6(7), 479-490.

Messier, D. R., Riley, F. L., & Brook, R. J. (1978). The α/β silicon nitride phase transformation. *Journal of Materials Science*, 13(6), 1199-1205.

Mitchell, R. S. (1954). Studies on a Group of Silicon Carbide Structures. *The Journal of Chemical Physics*, 22(12), 1977-1983.

Miyamoto, Y., & Yu, B. D. (2002). Computational designing of graphitic silicon carbide and its tubular forms. *Applied physics letters*, 80(4), 586-588.

Nagasawa, H., & Yagi, K. (1997). 3C-SiC Single-Crystal Films Grown on 6-Inch Si Substrates. *physica status solidi (b)*, 202(1), 335-358.

Nagasawa, H., Abe, M., Yagi, K., Kawahara, T., & Hatta, N. (2008). Fabrication of high performance 3C-SiC vertical MOSFETs by reducing planar defects. *physica status solidi (b)*, 245(7), 1272-1280. 523-530.

Nagesh, V., Farmer, J. W., Davis, R. F., & Kong, H. S. (1987). Defects in neutron irradiated SiC. *Applied physics letters*, 50(17), 1138-1140.

Nakashima, S. I., & Harima, H. (1997). Raman investigation of SiC polytypes. *physica status solidi (a)*, 162(1), 39-64.

Ni, Z., Liu, Q., Tang, K., Zheng, J., Zhou, J., Qin, R., ... & Lu, J. (2011). Tunable bandgap in silicene and germanene. *Nano letters*, 12(1), 113-118.

Nicotra, G., Ramasse, Q. M., Deretzis, I., La Magna, A., Spinella, C., & Giannazzo, F. (2013). Delaminated graphene at silicon carbide facets: atomic scale imaging and spectroscopy. *ACS nano*, 7(4), 3045-3052.

Nishino, S., Powell, J. A., & Will, H. A. (1983). Production of large-area single-crystal wafers of cubic SiC for semiconductor devices. *Applied Physics Letters*, 42(5), 460-462.

Oganov, A. R., Chen, J., Gatti, C., Ma, Y., Ma, Y., Glass, C. W., ... & Solozhenko, V. L. (2009). Ionic high-pressure form of elemental boron. *Nature*, 457(7231), 863-867.

Okojie, R. S., Xhang, M., Pirouz, P., Tumakha, S., Jessen, G., & Brillson, L. J. (2001). Observation of 4H-SiC to 3C-SiC polytypic transformation during oxidation. *Applied Physics Letters*, 79(19), 3056-3058.

Pei, L. Z., Tang, Y. H., Chen, Y. W., Guo, C., Li, X. X., Yuan, Y., & Zhang, Y. (2006). Preparation of silicon carbide nanotubes by hydrothermal method. *Journal of applied physics*, 99(11), 114306.

Penev, E. S., Bhowmick, S., Sadrzadeh, A., & Yakobson, B. I. (2012). Polymorphism of two-dimensional boron. *Nano letters*, 12(5), 2441-2445.

Perdew, J. P., Ruzsinszky, A., Csonka, G. I., Vydrov, O. A., Scuseria, G. E., Constantin, L. A., ... & Burke, K. (2008). Restoring the density-gradient expansion for exchange in solids and surfaces. *Physical Review Letters*, 100(13), 136406.

Pirouz, P., Chorey, C. M., & Powell, J. A. (1987). Antiphase boundaries in epitaxially grown β -SiC. *Applied Physics Letters*, 50(4), 221-223.

Polyakov, V. M., & Schwierz, F. (2005). Formation of two-dimensional electron gases in polytypic SiC heterostructures. *Journal of applied physics*, 98(2), 023709.

Porezag, D., & Pederson, M. R. (1996). Infrared intensities and Raman-scattering activities within density-functional theory. *Physical Review B*, 54(11), 7830.

Powell, A. R., & Rowland, L. B. (2002). SiC materials-progress, status, and potential roadblocks. *Proceedings of the IEEE*, 90(6), 942-955.

- Powell, J. A., & Will, H. A. (1972). Low-Temperature Solid-State Phase Transformations in 2 H Silicon Carbide. *Journal of Applied Physics*, 43(4), 1400-1408.
- Powell, J. A., Petit, J. B., Edgar, J. H., Jenkins, I. G., Matus, L. G., Yang, J. W., ... & Yoganathan, M. (1991). Controlled growth of 3C-SiC and 6H-SiC films on low-tilt-angle vicinal (0001) 6H-SiC wafers. *Applied physics letters*, 59(3), 333-335.
- Qin, X., Liu, Y., Li, X., Xu, J., Chi, B., Zhai, D., & Zhao, X. (2015). Origin of Dirac Cones in SiC Silagraphene: A Combined Density Functional and Tight-Binding Study. *The journal of physical chemistry letters*, 6(8), 1333-1339.
- Qteish, A., Heine, V., & Needs, R. J. (1992). Polarization, band lineups, and stability of SiC polytypes. *Physical Review B*, 45(12), 6534.
- Rong, Z. Y., & Kuiper, P. (1993). Electronic effects in scanning tunneling microscopy: Moiré pattern on a graphite surface. *Physical Review B*, 48(23), 17427.
- Sara, R. V. (1965). Phase Equilibria in the system tungsten—carbon. *Journal of the American Ceramic Society*, 48(5), 251-257.
- Sasaki, K., Sakuma, E., Misawa, S., Yoshida, S., & Gonda, S. (1984). High-temperature electrical properties of 3C-SiC epitaxial layers grown by chemical vapor deposition. *Applied physics letters*, 45(1), 72-73.
- Schomer, R., Friedrichs, P., Peters, D., & Stephani, D. (1999). Significantly improved performance of MOSFETs on silicon carbide using the 15R-SiC polytype. *IEEE Electron Device Letters*, 20(5), 241-244.
- Schöner, A., Krieger, M., Pensl, G., Abe, M., & Nagasawa, H. (2006). Fabrication and Characterization of 3C-SiC-Based MOSFETs. *Chemical Vapor Deposition*, 12(8-9), 523-530.
- Shimoda, K., Park, J. S., Hinoki, T., & Kohyama, A. (2007). Influence of surface structure of SiC nano-sized powder analyzed by X-ray photoelectron spectroscopy on basic powder characteristics. *Applied Surface Science*, 253(24), 9450-9456.
- Sorokin, P. B., Kvashnin, A. G., Zhu, Z., & Tománek, D. (2014). Spontaneous graphitization of ultrathin cubic structures: a computational study. *Nano letters*, 14(12), 7126-7130.
- Sridhara, S. G., Carlsson, F. H. C., Bergman, J. P., & Janzén, E. (2001). Luminescence from stacking faults in 4H SiC. *Applied physics letters*, 79(24), 3944-3946.
- Sugii, T., Aoyama, T., & Ito, T. (1990). Low-Temperature Growth of β -SiC on Si by Gas-Source MBE. *Journal of The Electrochemical Society*, 137(3), 989-992.
- Sun, L., Li, Y., Li, Z., Li, Q., Zhou, Z., Chen, Z., ... & Hou, J. G. (2008). Electronic structures of SiC nanoribbons. *The Journal of chemical physics*, 129(17), 174114.
- Sun, X. H., Li, C. P., Wong, W. K., Wong, N. B., Lee, C. S., Lee, S. T., & Teo, B. K. (2002). Formation of silicon carbide nanotubes and nanowires via reaction of silicon

(from disproportionation of silicon monoxide) with carbon nanotubes. *Journal of the American Chemical Society*, 124(48), 14464-14471.

Susi, T., Skákalová, V., Mittelberger, A., Kotrusz, P., Hulman, M., Pennycook, T. J., ... & Meyer, J. C. (2017). Computational insights and the observation of SiC nanograin assembly: towards 2D silicon carbide. *Scientific Reports*, 7(1), 4399.

Szwacki, N. G., & Tymczak, C. J. (2010). The symmetry of the boron buckyball and a related boron nanotube. *Chemical Physics Letters*, 494(1), 80-83.

Taguchi, T., Igawa, N., Yamamoto, H., Shamoto, S. I., & Jitsukawa, S. (2005). Preparation and characterization of single-phase SiC nanotubes and C-SiC coaxial nanotubes. *Physica E: Low-dimensional Systems and Nanostructures*, 28(4), 431-438.

Takeuchi, T., Amano, H., Hiramatsu, K., Sawaki, N., & Akasaki, I. (1991). Growth of single crystalline GaN film on Si substrate using 3C-SiC as an intermediate layer. *Journal of Crystal Growth*, 115(1), 634-638.

Tkatchenko, A., DiStasio Jr, R. A., Car, R., & Scheffler, M. (2012). Accurate and efficient method for many-body van der Waals interactions. *Physical review letters*, 108(23), 236402.

Trew, R. J., Yan, J. B., & Mock, P. M. (1991). The potential of diamond and SiC electronic devices for microwave and millimeter-wave power applications. *Proceedings of the IEEE*, 79(5), 598-620.

Tunega, D., Bučko, T., & Zaoui, A. (2012). Assessment of ten DFT methods in predicting structures of sheet silicates: Importance of dispersion corrections. *The Journal of Chemical Physics*, 137(11), 114105.

Tusche, C., Meyerheim, H. L., & Kirschner, J. (2007). Observation of depolarized ZnO (0001) monolayers: formation of unreconstructed planar sheets. *Physical review letters*, 99(2), 026102.

Vlasse, M., Naslain, R., Kasper, J. S., & Ploog, K. (1979). Crystal structure of tetragonal boron related to α -AlB₁₂. *Journal of Solid State Chemistry*, 28(3), 289-301.

Wang, H., Li, X. D., Kim, T. S., & Kim, D. P. (2005). Inorganic polymer-derived tubular SiC arrays from sacrificial alumina templates. *Applied Physics Letters*, 86(17), 173104.

Wang, L., Wada, H., & Allard, L. F. (1992). Synthesis and characterization of SiC whiskers. *Journal of materials research*, 7(1), 148-163.

Wen, B., & Melnik, R. (2008). Relative stability of nanosized wurtzite and graphitic ZnO from density functional theory. *Chemical Physics Letters*, 466(1), 84-87.

Wu, D., Lagally, M. G., & Liu, F. (2011). Stabilizing graphitic thin films of wurtzite materials by epitaxial strain. *Physical review letters*, 107(23), 236101.

Xu, F. F., & Bando, Y. (2004). Formation of two-dimensional nanomaterials of boron carbides. *The Journal of Physical Chemistry B*, 108(23), 7651-7655.

Xue, X. Y., Zhang, R. Q., & Zhang, X. H. (2005). Structural and electronic properties of 9R diamond polytype. *Solid state communications*, 136(1), 41-44.

Yaghoubi, A. (2013). *Self-assembly of Optically Tunable Quantum Heterostructure Superlattices Using Impermeable Plasma of Carbon* (Doctoral dissertation, Jabatan Kejuruteraan Mekanik, Fakulti Kejuruteraan, Universiti Malaya).

Yaghoubi, A., & Mélinon, P. (2013). Tunable synthesis and in situ growth of silicon-carbon mesostructures using impermeable plasma. *Scientific reports*, 3.

Yano, H., Hirao, T., Kimoto, T., Matsunami, H., Asano, K., & Sugawara, Y. (1999). High channel mobility in inversion layers of 4H-SiC MOSFETs by utilizing (112̄ 0) face. *IEEE Electron Device Letters*, 20(12), 611-613.

Yoshida, S., Daimon, H., Yamanaka, M., Sakuma, E., Misawa, S., & Endo, K. (1986). Schottky-barrier field-effect transistors of 3C-SiC. *Journal of applied physics*, 60(8), 2989-2991.

Yoshida, S., Sasaki, K., Sakuma, E., Misawa, S., & Gonda, S. (1985). Schottky barrier diodes on 3C-SiC. *Applied Physics Letters*, 46(8), 766-768.

Young, D. J., Du, J., Zorman, C. A., & Ko, W. H. (2004). High-temperature single-crystal 3C-SiC capacitive pressure sensor. *IEEE Sensors Journal*, 4(4), 464-470.

Yu, M., Jayanthi, C. S., & Wu, S. Y. (2010). Geometric and electronic structures of graphitic-like and tubular silicon carbides: Ab-initio studies. *Physical Review B*, 82(7), 075407.

Zhang, B., Li, J., Zhai, H., & Zhang, S. (2002). Growth of SiC-AlN whisker with the polytype of 2H. *Journal of materials science letters*, 21(5), 431-434.

Zhao, J. H., Alexandrov, P., & Li, X. (2003). Demonstration of the first 10-kV 4H-SiC Schottky barrier diodes. *IEEE Electron Device Letters*, 24(6), 402-404.

Zhao, M., Xia, Y., Li, F., Zhang, R. Q., & Lee, S. T. (2005). Strain energy and electronic structures of silicon carbide nanotubes: density functional calculations. *Physical Review B*, 71(8), 085312.

Zheng, L., Feng, L., & Yong-Shi, W. (2014). Exotic electronic states in the world of flat bands: From theory to material. *Chinese Physics B*, 23(7), 077308.

Zhou, L. J., Zhang, Y. F., & Wu, L. M. (2013). SiC₂ siligraphene and nanotubes: novel donor materials in excitonic solar cells. *Nano letters*, 13(11), 5431-5436.

Zorman, C. A., Fleischman, A. J., Dewa, A. S., Mehregany, M., Jacob, C., Nishino, S., & Pirouz, P. (1995). Epitaxial growth of 3C-SiC films on 4 in. diam (100) silicon wafers by atmospheric pressure chemical vapor deposition. *Journal of Applied Physics*, 78(8), 5136-5138.

LIST OF PUBLICATIONS

Yaghoubi, A., Masenelli-Varlot, K., Boisron, O., Ramesh, S., & Melinon, P. (2018). Is graphitic silicon carbide (silagraphene) stable?. *Chemistry of Materials*, 30(20), 7234-7244. **IF: 9.890**

Yaghoubi, A., Singh, R., & Melinon, P. (2018). Predicting the primitive form of rhombohedral silicon carbide (9R-SiC): A pathway toward polytypic heterojunctions. *Crystal Growth & Design*, 18(11), 7059-7064. **IF: 3.972**

University of Malaya